Pattern Formation in Engineered Bacteria: from Understanding to Applications

by

Yangxiaolu Cao

Department of Biomedical Engineering
Duke University

Date: _____
Approved:

_____
Lingchong You, Supervisor

_____
John Neu

_____
Fan Yuan

_____
Stefan Zauscher

_____
Katia Koelle

Dissertation submitted in partial fulfillment of
the requirements for the degree of Doctor
of Philosophy in the Department of
Biomedical Engineering in the Graduate School
of Duke University

2017

ABSTRACT

Pattern Formation in Engineered Bacteria: from Understanding to Applications

by

Yangxiaolu Cao

Department of Biomedical Engineering
Duke University

Date: _____
Approved:

_____
Lingchong You, Supervisor

_____
John Neu

_____
Fan Yuan

_____
Stefan Zauscher

_____
Katia Koelle

An abstract of a dissertation submitted in partial
fulfillment of the requirements for the degree
of Doctor of Philosophy in the Department of
Biomedical Engineering in the Graduate School of
Duke University

2017

Abstract

Patterns are ubiquitous in living organisms. However, the mechanisms driving self-organized pattern formations are not well understood. Due to the complexity of natural systems, many confounding factors complicate quantitative experiments and data interpretation, often making it difficult to draw definitive conclusions. Therefore, a limited number of experimental systems could enable precise perturbation and quantification of pattern formation. In comparison, the synthetic system serves as well-defined model systems to elucidate ''design principles'' of biological networks. In the past sixteen years, engineering pattern formation is a major endeavor in synthetic biology. However, there are only two studies about the generation of programmed self-organized pattern formation in growing cells based on coordinated dynamics in a population.

Intrigued by the challenge, my colleagues and I programmed *E. coli* with a synthetic gene circuit to generate self-organized pattern formation. Two implications of this engineered pattern-forming system were illustrated in my Ph.D. thesis.

First, the synthetic system provides a well-defined context to probe principles underlying the scaling property of self-organized pattern formation. Our mechanism underscores the importance of temporal control in generating scale-invariant patterns.

The fundamental premise of this approach is that the principles defined in such engineered systems can be generally applicable to natural examples.

Second, the synthetic system serves as a foundation to generate structured materials with well-defined physical properties. Diverse natural biological systems can form structured materials with well-defined physical and chemical properties spontaneously. However, these natural processes are not readily programmable. By taking the synthetic biology approach, we demonstrate here the programmable, three-dimensional (3D) material fabrication using pattern-forming bacteria growing on top of permeable membranes as the structural scaffold. We equip the bacteria with an engineered protein that enables the assembly of gold nanoparticles into a hybrid organic-inorganic dome structure. The resulting hybrid structure functions as a pressure sensor that responds to touch. We show that the response dynamics are determined by the geometry of the structure, which is programmable by the membrane properties and the extent of circuit activation. Taking advantage of this property, we demonstrate signal sensing and processing using one or multiple bacterially assembled structures.

Dedication

To my family and friends who provided me emotional and physical supports, who still chose to stand by me when I was irrational, who loved and will continue to love me.

Contents

Abstract iv

List of Tables xi

List of Figures xii

Acknowledgements xxix

1. Overview 1

1.1 Objectives 1

1.2 Organization of the objectives 2

2. Generation of Periodic Patterns 4

2.1 Introduction 4

2.2 Elements to generate periodic patterns 5

2.3 Perspectives 10

3.Collective Space-sensing Coordinates Pattern Scaling in Engineered Bacteria 12

3.1 introduction 12

3.2 Results 15

3.2.1 Scale invariance emerges from programmed pattern formation 15

3.2.2 Model reveals the essential requirement for scale invariance 17

3.2.3 Scale invariance is mediated by a collective sensing mechanism 22

3.2.4 The scale invariance is disrupted by perturbing temporal or spatial cues 27

3.3 Discussions 32

3.4 Supplementary experimental procedures 36

3.4.1 Strains, media, and device 36
3.4.1.1 Bacteria strains 36
3.4.1.2 Circuit and Plasmids 36
3.4.1.3 Growth media 36
3.4.1.4 Overnight culture 37
3.4.1.5 Culture well 37
3.4.2 Methods 37
3.4.2.1 Measurement of cell density in liquid culture 37
3.4.2.2 Fluorescent microscopy 38
3.4.2.3 Inkjet printing 38
3.4.2.4 Precise control of seeding configuration by inkjet printing 42
3.4.2.5 Domain size calculation 43
3.4.2.6 Control experiments 43
3.4.2.7 Colony radius measurement 43
3.5 Model development 44
3.5.1 Derivation of passion tracer equations 48
3.5.2 Non-dimensionalization of the model 49
3.5.3 mCherry and CFP equations 51
3.5.4 Domain shape, initial conditions, and boundary conditions 52
3.5.5 Numerical solver for the PDE model 53
3.5.6 Parameters screening and execution of PDE model 54
3.5.7 Comparison with previous patterning dynamics 58

3.5.8 Emergence of scale invariance 60

3.5.9 Effects of adding exogenous AHL 69

3.5.10 Effect of higher metabolic burden 72

3.5.11 Effects of reducing the positive feedback strength 74

3.5.12 Comparison with representative mechanisms for pattern generation and scaling 76

4. Programmed Assembly of Pressure Sensor using Pattern-formation Bacteria 81

4.1 Introduction 81

4.2 Results 84

4.2.1 Pattern-curli formation 84

4.2.2 Inorganic material assembly to bacterial colony 85

4.2.3 Bacterial growth and pattern formation on permeable membrane 85

4.2.4 Fabrication of bacterial pressure sensor 89

4.2.5 Applications of bacterial pressure sensor 95

4.3 Discussions 98

4.4 Supplementary materials and methods 100

4.4.1 Plasmids, cell strains, and growth media 100

4.4.2 Methods 101

4.4.2.1 Measurement of cell density in liquid culture 101

4.4.2.2 Transmission electron microcopy (TEM) 101

4.4.2.3 Scanning electron microscopy (SEM) 101

4.4.2.4 NiNTA-AuNP labelling 102

4.4.2.5 Inkjet printing 104

4.4.2.6 Immunolabeling nanoparticles to the colonies 107

4.4.2.7 Electrochemical measurement 109

4.4.3 Model development 111

4.4.3.1 Colony growth dynamics 111

4.4.3.2 Expression profiles 115

5. Concluding Remarks and Future Directions 119

5.1 Concluding remarks 119

5.2 Future directions 124

5.2.1 Generation of complex patterns 124

References 127

Biography 140

List of Tables

Table 1: Definition and the value of parameters used in the PDE model 46

Table 2: Expression and value of coefficient in nondimensional model 50

Table 3: Definition and the value of parameters used in the ODE model 112

Table 4: Expression and value of coefficient in nondimensional model 118

List of Figures

Figure 1: Generation of periodic patterns. A. Delayed negative feedback emerges from the interplay between two subpopulations in a colony [21]. During cell growth, consumption of glutamate from cells at the periphery of the colony is triggered by ammonium. At the same time, glutamate limits ammonium production from the interior cells. This process leads to oscillations in the colony radius expanding rate over time. B. Positive feedback integrated with negative feedback. During cell division, MinD and MinE oscillate from one pole to the other. Eventually, MinE precisely locates the center of the cell to determine the correct location for forming a ring-like structure [22, 23]. C. Positive feedback integrated with negative feedback with various time delays. By adjusting the initial concentration of AHL, AHL dynamics change over time (left panel). Different size and number of periodic patterns can be formed [24]. D. Positive feedback integrated with negative feedback. The activation module is local, whereas inhibition is long range. This basic reaction-diffusion model is a basic mechanism for generating periodic Turing pattern. Activator and inhibitor form waves in space, leading to periodic patterns. 7

Figure 2: Scale invariance in self-organized pattern formation in engineered bacteria. A. Circuit logic. The circuit consists of a T7 RNA polymerase that activates its own expression as well as the expression of LuxR and LuxI. Upon activation by T7RNAP (T7), LuxI mediates synthesis of AHL (A), which can diffuse across the cell membrane. When the global AHL concentration surpasses a threshold, intracellular AHL binds to LuxR to activate the synthesis of T7 lysozyme (L). Lysozyme then binds to the T7RNAP and forms a T7-lysozyme complex, therefore inhibiting the T7RNAP binding to the T7 promoter. This T7- lysozyme complex also inhibits T7RNAP transcription. In this process, the AHL concentration is affected by its initial concentration and the domain size. The expression rates of T7RNAP, lysozyme, and AHL are all controlled by the spatially dependent gene expression capacity. B. Self-organized pattern formation in engineered bacteria. Left: A composite fluorescent image. Right: mCherry image extracted by MATLAB code from left composite image. Images of a 1.2mm × 1.2mm field of colony at 2500 μm domain radius after 24 h of incubation. The experimental platform used here was described in Figure 7A. C. Scale invariance in self-organized pattern formation. The mCherry ring width (red circle) and the colony radius (green circle) are plotted as a function of the domain radius. Measurements were done in microcolonies after 32 h incubation. The error bars represent the standard error from ≥5 replicates for each domain radius. The solid lines represent the linear regression of the data points (green: colony radius; red: ring width) for intermediate domain radii (between 1500 μm and 7500 μm), where scale invariance emerges (the R-square value

for ring width vs. domain radius linear regression is 0.9828; the R-square value for colony radius vs. domain radius linear regression is 0.9943). The purple block corresponds to domain radii<1500 μm; the yellow block corresponds to domain radii >7500 μm. The insets show mCherry images for domain radii of 1500 μm, 2500 μm, and 3750 μm, respectively. For all of the presented figures, if unnoted, filled circles represent the data where ring width vs. colony radius follows a linear regression with domain radius. D. Ratio of mCherry ring width to colony radius for different domain radii. The ratio was calculated from the data in Figure 1C. The dashed line shows the average ratio for data points within the range of domain radii where the scale invariance emerges. The standard deviation of the ratio values between 1500 and 7500 μm is 0.0448 (~10% of the total constant ratio). 15

Figure 3: Pattern formation dynamics in engineered bacteria. A. Parameter search. Each spike represents the range of a parameter, ranging from 0 to its maximum value (the intersect with the outer circle) [67]. $\boldsymbol{G4}$ was explored between 0 and 10; other parameters' search ranges are listed in Table 1. Each polygon represents a parameter set. I started with 18,231 parameter sets (light blue). Dark blue lines indicate 409 parameter sets that generated core-ring patterns for varying domain radii (from 1 to 3). A local search on each of these 409 sets led to an optimal parameter set that generated scale invariance (red curves). $\boldsymbol{\alpha}$ and $\boldsymbol{\beta}$ are the inhibition factors of T7RNAP and T7 lysozyme on cell growth, respectively. $\boldsymbol{n}$ is the Hill coefficient for distance-dependent gene expression capacity. $\boldsymbol{K\varphi}$ is the half activation distance for gene expression capacity. $\boldsymbol{\alpha T}$ and $\boldsymbol{\alpha L}$ are synthesis rates of T7RNAP and T7 lysozyme, respectively. $\boldsymbol{KT}$ and $\boldsymbol{KP}$ are half-inhibition concentration of T7RNAP and T7-lyszome complex, respectively. $\boldsymbol{G4}$ is the synthesis rate of AHL, after non-dimensionalized. B. Conditions underlying scale invariance. Five parameters shifted systematically during the optimization step: $\boldsymbol{\alpha}$ **and** $\boldsymbol{\beta}$ characterize circuit mediated metabolic burden; $\boldsymbol{n}$ **and** $\boldsymbol{K\varphi}$ determine the shape of gene expression capacity; and $\boldsymbol{\alpha T}$ characterize the strength of T7RNAP feedback. In contrast, the four other parameters, $\boldsymbol{G4}$, $\boldsymbol{\alpha L}$, $\boldsymbol{KT}$, and $\boldsymbol{KP}$ did not change significantly during optimization. The blue histograms represent values from the 409 pattern-forming sets in Figure 2A before optimization. The red histograms represent values of the 409 sets resulting from the optimization. The light red is the overlap between blue and red histogram. C. Simulated spatio-temporal profiles of CFP and mCherry intensity. Left: Average CFP intensity over colony cross-section from 1 to 150 in arbitrary unit. Right: Average mCherry intensity over colony cross-section from 1 to 150 in arbitrary unit. D. Experimentally measured spatio-temporal profiles of CFP and mCherry. Left: average CFP intensity of bacterial colony at different radii from 8 h to 43 h. Right: Average mCherry intensity of bacterial colony at different radii from 8 h to 43 h. The experiments were measured at domain radius of 2500 μm. 19

Figure 4: A collective space sensing mechanism underlies scale invariance. A. A collective space sensing mechanism. The domain size controls the pace and extent of colony expansion by determining nutrient availability. The domain size also controls the timing of ring initiation by determining the accumulation rate of AHL. The interplay of the gene expression capacity (magenta curve), T7RNAP profile (blue curve), and AHL concentration (orange curve) leads to the scale invariance of ring width to colony size. The gene expression capacity and T7RNAP profiles are drawn as functions of the distance to the colony center at the final time point. The red arrow indicates the time window for ring maturation. B. Simulated emergence of a core-ring pattern. Top: AHL (orange curve) and nutrient (black curve) concentrations over time. Bottom: Simulated mCherry distributions at different time points. The time points were labeled on x-axis. The mCherry ring initiates when AHL reaches its maximum concentration ($\boldsymbol{t1}$), which coincides with a pause of colony expansion ($\boldsymbol{t2}$). The ring matures during the time window, $\Delta\boldsymbol{T}$, between ring initiation and system stabilization (red arrow). C. Emergence of scale invariance during core formation. When the colony is at fast expanding phase, the pattering process is mainly governed by an integral feedback topology which is similar to the expansion-repression model [53]. In our model, the T7RNAP can be considered the expander that drives morphogen (AHL) synthesis, whereas the T7 lysozyme serves as the repressor. At time point $\boldsymbol{t1}$, the mCherry profile scales with colony radius. D. Emergence of scale invariance during ring maturation. All the x-axes are normalized to the domain radius. The units of y-axes are all on a per cell basis. Left: At different domain radii, the mCherry profile (pink) at the ring initiation time ($\boldsymbol{t1}$) approximately scales with domain size. $\boldsymbol{RC}$ is the colony radius, and it is a function of domain radius. Middle: mCherry accumulation during maturation time ($\Delta\boldsymbol{T}$) is mainly determined by the gene expression capacity. The x-axis represents the distance from the colony edge. $\boldsymbol{D1}$ and $\boldsymbol{D2}$ are two different domain radii, $\boldsymbol{D1} < \boldsymbol{D2}$. $\boldsymbol{RC\_D1}$ and $\boldsymbol{RC\_D2}$ are the colony radius for domain radii $\boldsymbol{D1}$ and $\boldsymbol{D2}$, respectively. The y-axis is $\Delta\boldsymbol{T}$, the maturation time window. $\Delta\boldsymbol{TD1}$ and $\Delta\boldsymbol{TD2}$ are the maturation time windows when the domain radii are $\boldsymbol{D1}$ (light magenta) and $\boldsymbol{D2}$ (dark magenta). The intersect of x- and y-axes represent that the mCherry accumulation rate is 0 at the colony edge at ring initiation time, $\boldsymbol{t1}$. The z-axis indicates the mCherry accumulation during the given time window. Right: mCherry at $\boldsymbol{t2}$ is a combination of that at $\boldsymbol{t1}$ (pink) and that accumulated during $\Delta\boldsymbol{T}$ (color code is the same with that in middle panel). Its minimum is at the same relative location on the normalized axis (red pointer), indicating proportionality between the inner edge position and the domain radius. The outer edge of the ring pattern is roughly the colony edge, which is also proportional to the domain radius. Combining these two aspects leads to a ring width that scales with the colony size. 23

Figure 5: Modulation of scaling property by environmental factors. A. Simulated scale invariance (base case). Left: Illustration of T7RNAP and gene expression capacity shape in the scale invariance range. Middle: Dependence of the ring width (red circles) and the colony radius (green circles) on the domain radius. The solid lines represent the linear regression of the colony radius and the ring width with respect to the domain radius in the white region. Solid circles represent the linear range of the dependence of the ring width and colony radius on the domain radius. Right: The ratio of mCherry ring width to the colony radius for different domain radii. The dashed line shows the average ratio for the values in the white region. Top left: Illustration of gene expression capacity profile when the domain is too small (purple shaded regions in Top and Middle panels). Top right: Illustration of the AHL profile over time when the domain is too large (yellow shaded regions in Top and Middle panels). The thinner gray curve corresponds to the AHL profile in the left panel; the thicker orange curve corresponds to a larger domain. These results correspond to time point $\boldsymbol{t2}$. B. Modulating the scaling property by adding exogenous AHL. Left: T7RNAP and gene expression capacity profiles were the same with those in base case. Adding exogenous AHL changes the temporal cue. The thinner gray line indicates the AHL concentration over time in the base case; the thicker orange line indicates the AHL concentration over time in the presence of initial exogenous AHL. The ring maturation window is longer (red arrow) compared with the base case. Right top: Simulated scaling property when the parameter of initial exogenous AHL ($\boldsymbol{ahl0}$) were set to 10 and 25 (from left to right). The two figures show relationships of colony radius and of ring width to domain radius with different initial AHL concentrations. The insets represent the ratio of the ring width to the colony radius. The x-axes for the insets are on the same scale as the corresponding figure panels; the y-axes range from 0 to 1. Right bottom: Experimentally measured scaling property in the presence of 20 nM AHL and 50 nM AHL (from left to right). The two figures are plotted as in Figures 1C, D. The error bars represent the standard error or range of 2-5 replicates. Each data point was obtained at 32h after start of experiment. C. Modulating the scaling property by having a higher metabolic burden. Cell growth is slowed down at a high metabolic burden, so AHL reaches its peak value later than in the base case. At that time, T7RNAP distribution over space is not flat yet; instead, it has a higher distribution near the center of the colony, which will increase the mCherry core accumulation during the ring maturation stage. Because the maturation time is shorter, the ring cannot catch up with the core formation and the eventual ring width is smaller. The figure symbols are the same as those in Figure 4B. Simulated scaling properties with $\boldsymbol{\gamma}$, the metabolic burden from an effector gene, at a value of 5 ($\boldsymbol{\gamma}$ = 0 for the base case). D. Modulating the scaling property by using weak T7RNAP positive feedback. Due to the weak feedback, the T7RNAP distribution over space is no longer flat but instead reflects that of the gene expression profile. The weak feedback also slows down accumulation of AHL, thus

delaying the ring initiation in comparison with the base case. Therefore, the ring maturation time (red arrow) is shorter than that in the base case. The figure symbols are the same as those in Figure 4B. The scaling property was simulated with varying positive-feedback strength (the T7 promoter rate is 0.25 or 0.1 fold of promoter rate when circuit is fully induced).....28

Figure 6: Sequential actions of integral feedback and incoherent feedforward underlie the scale invariance. The overall system input is the domain size; the output is the mCherry pattern in a colony scaled with respect to the domain size. The integral feedback underlies a scale-invariant mCherry distribution at ring initiation. In our system, the activation module represents the strong T7RNAP positive feedback; morphogen represents AHL; the repression module represents T7 lysozyme. The incoherent feedforward controls the mCherry increment during maturation time window of ring formation. $\Delta\boldsymbol{T}$ is a proportional function of domain size; $\boldsymbol{rate}$ represents mCherry accumulation rate, which is dominated by gene expression capacity during ring maturation. At the same relative location, a larger domain results in smaller gene expression capacity and thus a reduced accumulation rate in mCherry. This reduction is compensated by the increase in $\Delta\boldsymbol{T}$, leading to the same increment in mCherry at the same relative position for different domain sizes. The sum of the mCherry distribution at ring initiation and the increment during maturation leads to the final mCherry ring (red) that scales with the domain size. The color code is the same as in previous figures.....33

Figure 7: Experiment platform and patterns and growth of inkjet-printed MG1655 cells with or without the gene circuit. A. Protocol for patterning experiments. An LB culture of MG1655 carrying the full gene circuit was grown for 14 h at 37℃. 0.3% molten agar in 2xYT (PH=6.5) medium was prepared. While allowing it to cool, I diluted the overnight culture to an OD of 0.2, and then diluted the resulting culture another 50-fold into 10mL fresh LB culture before loading it into the inkjet printer cartridge. After the agar cooled down to 50˚C, IPTG and appropriate antibiotics were added. 170 μl of the agar was added to each culture-well. After the agar solidified, I then used the inject printer to print the bacteria (1 pixel size) onto the agar surface using a designed template. A glass coverslip was placed on top of the culture-well after printing. Because of the difference of agar volume and culture-well volume, there was an approximately 20 μm air gap between the agar surface and the top glass cover. B. A multi-chamber culture-well. The dimension of the culture-well is illustrated in this graph. For a detailed description, refer to the user manual of the product: Culture Well™ multiwell chambered coverslip (Grace Bio-Labs; Bend, OR, USA; Item #103310). C. A composite fluorescent microscopy image of inkjet-printed microcolonies. Left: Colonies of MC4100 cells carrying ptetmCherry. The printing template was an array with 1000 μm spacing distance. After 24 h

incubation, the distance measured between the center of the colonies were 975.9 μm, and 972.7 μm. Right: Mean and standard deviation of measured distance between centers of the colonies with template spacing distance of 500 μm and 1000 μm, respectively. D. Sample colony arrays corresponding to varying domain radius per colony. Colonies of MG1655 carrying the full circuit. The domain radius was determined by the configuration of initial printing template. The images were taken after 24 h incubation. For the detailed effective domain radius calculation, see "domain size calculation" in Method section. E. mCherry (green dots) and CFP (magenta dots) intensity at varying radial distances from the center, quantified from the images in Figure 2B. The solid red and blue lines represent the running averages of mCherry and CFP intensities, respectively. The black dash lines indicate the inner and outer edges of the mCherry ring. The local minimum of the valley between core and ring determines the inner edge of the ring. The outer edge corresponds to the position on other side of the ring that has the same mCherry intensity as the inner edge. The ring width is the distance between the inner and outer edges. Intensity values were calculated as the average intensity values across all angles at fixed radii about the microcolony core center. In all the images Figure 7E-G, blue represents CFP signal, red represents mCherry signal, green represents phase channel. F. Replicates of colonies with core-ring patterns. 1.7 mm × 1.4 mm composite fluorescent (mCherry and CFP) image of MG1655 cells carrying the full circuit. The colonies were from six different experiments. The images were taken after 24 - 32 h incubation at 30°C. G. Growth and gene expression dynamics of printed MG1655 cells constitutively expressing mCherry. Top: microscopy images of these cells at domain radii of 1500 μm, 2000 μm, and 2500 μm respectively after 24 h of incubation at 30°C. Bottom: mCherry intensities (green dots) at varying radial distance from the center, quantified from the mCherry images. Each solid red line represents the running averages of mCherry intensities across varying radii. H. Top: Heat map of fluorescent emission intensity from confocal image of DAPI stained microcolony after 32 h incubation in both vertical (y-axis) and radial directions (x-axis). The confocal images were taken under the wavelength of 358 nm ultraviolet light. The radial intensity values are the average intensity across angular spanning from 0 to 2π. This process was done by a customized MATLAB code. Bottom: Growth dynamics of the pattern over time. Left: Simulated dynamics of mCherry ring width (red) and colony radius (green) over time. The inner/outer ring edge location was measured as described in Figure 7E. The mCherry ring width is the distance between the outer ring edge and the inner ring edge. The colony radius is defined as the distance from the colony center to the edge, where the cell density is half of the maximum density. The configuration is the same as in the left graph. 40

Figure 8: Simulated and measured growth and pattern formation dynamics and constraining model parameters. A. Effects of IPTG induction on pattern formation. Microscopy images of MG1655 cells carrying the full circuit after different incubation time (14 h, 16 h, and 24 h) with and without 1mM IPTG at 30℃. The green channel represents the phase image, the blue channel represents CFP, and the red channel represents mCherry. The scale bar corresponds to 500 μm. The microscope exposure time to mCherry and CFP channels were consistent between two conditions. B. Measured ring width as a function of the initial AHL concentration. Left: The mCherry ring width decreased with the initial AHL concentration. These values were obtained from replicates after 32 h incubation under corresponding respective domain radii. The error bars represent the standard error (more than 3 replicates per domain radius). Right: Representative images of mCherry patterns with different initial AHL concentrations. mCherry images after 32 h incubation for initial AHL concentration of 5 nM, 20 nM, 30 nM, and 100 nM, respectively. C. Procedure of searching for pattern-forming parameters. Light blue curves represent 18,231 parameter combinations of $G4, \alpha, \beta, n, K\emptyset, \alpha T, \alpha L, KT, KP$. Dark blue curves represent 409 parameter sets that enhance pattern formation for varying domain radii (from 1 to 3). 55 out of 409 parameters sets could generate scale invariance. In these 409 parameter sets, depending on parameter values, there are two types of patterns. I highlighted two typical sets to make comparison. Green dashed curve: $G4 = 2, \beta = 500, K\varphi = 2, \alpha T = 6000, \alpha L = 4500, KT = 1200, KP = 400$, and $\alpha = 4, n = 4$; and red dashed curve: $G4, \alpha,\ K\varphi, \alpha T, \alpha L, KT, KP$ kept the same value compared to green dashed curve, but $\alpha = 0.4, n = 1$. D. Optimization of pattern-forming parameters to generate scale invariance. Step 1. Left: using the method described in Figure 2A, I chose one parameter set out of 409 as a starting set (dark blue curve, one parameter set from Figure 8C). Right: based on the parameter shown on top, mCherry ring width (red circle) and colony radius (blue circle) as a function of the domain radius. The inset is the ratio of the ring width to the colony radius as a function of the domain radius. The inset image is the ratio of ring with to colony radius as a function of domain radius. The standard deviation of these ratio values is 0.21. Step 2. Left: Add a normally distributed perturbation on each value, and repeat 10 times. If the new parameter set does not generate patterns, it is plotted in a gray polygon; otherwise, it is plotted in cyan. The green polygon indicates the parameter set with the highest score. Right: Based on the parameter set plotted in green, mCherry ring width (red circle) and colony radius (blue circle) as a function of the domain radius. The standard deviation of these ratio values is 0.12. Step 3. Iterate step 2 for nine more times. The parameter set with highest score (red) is the optimal set. The standard deviation of these ratio values is 0.07. This optimal parameter set generates scale invariance. E. Procedure of searching for pattern-forming parameters starting from constrained parameter sets. The searching range for α was swept from 0 to 2.5; β from 0 to 1×103; n from 0.5 to 2.5,

$K\varphi$ from 1 to 5; αT from 2.4×103 to 8×103, other parameter's search range are the same with those in Figure 2A. Light blue closed curves represent 6039 parameter combinations of $G4, \alpha, \beta, n, K\varphi, \alpha T, \alpha L, KT, KP$. Dark blue curves represent 1098 parameter sets that enhance pattern formation for varying domain radii (from 1 to 3). Without further optimizing, there are 784 out of these 1098 parameters sets could generate scale invariance. F. Growth of MC4100Z1 and MG1655 cells with or without the pattern-forming circuit and its variants. First panel from left to right: MC4100Z1 cells not carrying a circuit, carrying the positive-feedback module (pET15bLCFPT7) with/without IPTG, carrying the pattern-formation circuit with/without IPTG or AHL, or carrying pattern-formation circuit not containing the luxI gene with/without IPTG. Second panel from left to right: MG1655 cells not carrying a circuit, carrying the positive-feedback module (pET15bLCFPT7) with/without IPTG, carrying the pattern-formation circuit with/without IPTG or AHL, carrying the pattern-formation circuit not containing the luxI gene with/without IPTG, or carrying pattern_desulf circuit (blue) with IPTG induction. The y-axis represents optical density of culture under 600nm wavelength excitation, which was measured by a plate reader under 30℃. G. Two typical patterns. Green box (no scale invariance): simulation results from the parameter set described by green dashed curve in Figure 8C. The mCherry ring width from these patterns is approximately independent of the domain radius. Red box (scale invariance): simulation results from the parameter set described by red dashed curve in Figure 8C. The mCherry ring width is proportional to the domain radius. In both boxes, the left panels are the simulated mCherry patterns; the middle panels are the mCherry profiles as function of distance; the right panels describe the dependence of the colony radius and the ring width on the domain radius. In both graphs, the upper panels correspond to a small domain; the lower panels correspond to a large domain. 55

Figure 9: Simulated spatial and temporal dynamics of circuit components underlying the core-ring pattern formation and scale invariance. A. AHL and nutrient concentrations over time. Four dashed lines indicate four time points 5, 20, 40, 75 (artificial units). B. Profiles of key factors (spatial-dependent gene expression capacity, cell density, T7RNAP and lysozyme distribution) at the cellular level as a function of the radial distance from the center of colony at each phase. (1): CFP and mCherry core formation. Since AHL diffuses across the whole domain, its concentration is low initially and inhibition of T7 RNAP via AHL-activated T7 lysozyme is negligible. The gene expression capacity is uniformly high in the small colony. Therefore, CFP and mCherry distributions are mainly determined by the cell density distribution. (2): CFP ring formation. With the colony expanding, gene expression capacity begins to have significant effect. At the edge of the colony, high global gene expression capacity leads to high T7RNAP expression, giving rise to the formation of CFP ring. Though AHL

accumulates to a high level, high T7RNAP concentration and high gene expression capacity at the edge of the colony leads to an increase in the mCherry synthesis rate, but not yet a mCherry ring. (3): mCherry ring initiation. With nutrient depletion, the colony stops expanding. The combination of high AHL concentration, T7RNAP, and gene expression capacity leads to the initiation of a mCherry ring. (4): mCherry ring maturation. The AHL concentration decreases, but still stays over the threshold. Because cell diffusion begins to have a larger impact than colony driving force, the gene expression capacity leads to the maturation of mCherry ring. C. Profiles of T7RNAP and lysozyme distribution at the population level as a function of radial distance from the center of colony at each phase. By population level, I mean the total T7RNAP (or lysozyme) from all the cells at a specific location. D. T7RNAP profiles at the ring initiation time ($\boldsymbol{t1}$) on a normalized axis for varying domain radii (1.4 and 3). The x-axis is at relative length, scaled by the domain radius. The notation on top of the figure means strong positive feedback is the main reason for generating this flat T7RNAP profile. For all the images in Figures S3-5, if unnoted, lighter color means data generated in smaller domain. E. AHL and nutrient concentrations over time for different domain radii. The light to dark orange curves represent AHL concentrations for an increasing domain radius; the gray to black curves represent nutrient concentrations for an increasing domain radius. The peak of the AHL curve defines the ring initiation time, $t1$. Three straight solid green lines represent the nutrient depletion time, $t2$. The red arrows represent the ring maturation time ΔT for each domain radius. ΔT is proportional to domain radius D. F. Cell density and gene expression capacity profiles along the normalized axis, for a domain radius of 3. The half threshold of gene expression $K\varphi$ equals the half-width of cell distribution's wavefront (FW). G. Maturation of the mCherry ring from $\boldsymbol{t1}$ to $\boldsymbol{t2}$. All three panels are on a normalized x-axis. The units of y-axes are all in per cell base. mCherry @ $\boldsymbol{t1}$: The initial mCherry profiles (red curves) for different domain radii approximately overlap, indicating scale invariance. ΔmCherry during $\Delta\boldsymbol{T}$: the accumulation of mCherry is mainly determined by the gene expression capacity. At a larger domain radius, the profile of gene expression capacity is sharper compared to that at a smaller domain (dashed lines). However, the ring maturation time for a larger domain is longer (red arrow), so the total accumulation of mCherry (solid curves) at the same relative location is equivalent for different domains. That is, ΔmCherry is approximately scale invariant. mCherry @ $\boldsymbol{t2}$: After adding the accumulation profile on the mCherry profile at $t1$, the minimum point of the mCherry profile at steady state (red curve) is at the same relative location. Since the outer edge of the ring pattern is roughly the colony edge, this min point defines the inner ring edge. The inner edge of the mCherry ring is not scale invariant. Domain radius varies from 1.4 to 3. 64

Figure 10: Scaling property of patterns in the presence of exogenous AHL or a higher metabolic burden. A. T7RNAP profiles at the ring initiation time ($\boldsymbol{t1}$) on a normalized axis for varying domain radii (2.2 and 3.8). The x-axis is at relative length, scaled by the domain radius. The notation on top of the panel indicates that strong positive feedback is the cause of flat T7RNAP profile. B. AHL and nutrient concentrations over time for different domain radii. The AHL concentration starts from the same initial value for different domain at time 0. The ring maturation time ΔT for each domain radius is not proportional to domain radius D in this case. C. Cell density and gene expression capacity profiles along the normalized axis, for a domain radius of 3. $K\varphi$ is smaller than FW. D. Maturation of the mCherry ring from $\boldsymbol{t1}$ to $\boldsymbol{t2}$. mCherry @ $\boldsymbol{t1}$: The initial mCherry profiles (red curves) for different domain radii approximately overlap, with the middle part of the curve overlaps into a linear line. ΔmCherry during $\Delta\boldsymbol{T}$: Since ΔT is not proportional to D, and $K\varphi < FW$, ΔmCherry in this case is not scale invariant. mCherry @ $\boldsymbol{t2}$: After adding the accumulation profile on the mCherry profile at $t1$, the minimum point of the mCherry profile at steady state (red curve) is at the same relative location. The inner edge of the mCherry ring is not scale invariant. Domain radius varies from 2.2 to 3.8. E. Modulating the scaling property by adding exogenous AHL. Top: Simulated scaling property when the parameter of initial exogenous AHL ($ahl0$) was set to 5. The figure symbols are the same as those in Figure 4B. Bottom: Measured scaling property in the presence of 10 nM AHL. The error bars represent the standard error or range of 2-4 replicates. Each data point was obtained at 32h after start of experiment. The insets represent the ratio of the ring width to the colony radius. The x-axes for the insets are on the same scale as the corresponding figure panels; the y-axes range from 0 to 1. F. Modulating the scaling property by having a higher metabolic burden. Top: Simulated scaling property with metabolic burden from effector gene γ equal to 1 (γ value base case is 0). The figure symbols are the same as those in Figure 4C. Bottom: Measured scaling property in MG1655 carrying pattern_curli. Pattern curli induced a higher metabolic burden than the pattern-formation circuit. However, it induced a less burden than the pattern_desulf circuit. The insets represent the ratio of the ring width to the colony radius. The x-axes for the insets are on the same scale as the corresponding figure panels; the y-axes range from 0 to 1. 70

Figure 11: Scaling property of patterns for a weak positive feedback. A. T7RNAP profiles at the ring initiation time ($\boldsymbol{t1}$) on a normalized axis for varying domain radii (1 and 1.4). Because of the weak positive feedback, the profile of T7RNAP is not flat along x-axis, and it is not proportional over domain radius. B. AHL and nutrient concentrations over time for different domain radii. In this case, the ring maturation time ΔT is decreasing when domain radius D is decreasing. C. Cell density and gene expression capacity profiles along the normalized axis, for a domain radius of 1. $K\varphi$ equals to FW. D.

Maturation of the mCherry ring from $\boldsymbol{t1}$ to $\boldsymbol{t2}$. mCherry @ $\boldsymbol{t1}$: The initial mCherry profiles (red curves) for different domain radii do not overlap. ΔmCherry during $\Delta\boldsymbol{T}$: Because ΔT is not proportional to D, ΔmCherry in this case is not scale invariant. mCherry @ $\boldsymbol{t2}$: After adding the accumulation profile on the mCherry profile at $t1$, the inner edge of the mCherry ring is not scale invariant. All the three figures, light red to dark red present measurements in domain radius varies from 1 to 1.4. E. Modulating the scaling property by using weak T7RNAP positive feedback. Top: Simulated scaling property with varying positive-feedback strength (the T7 promoter rate is 0.8 and 0.2 fold of promoter rate when circuit is fully induced). The feedback strength decreases from left to right. The figure symbols are the same as those in Figure 4D. Bottom: Experimentally measured scaling property in the presence of 100 μM (left) and 1 μM (right) IPTG. The insets represent the ratio of the ring width to the colony radius. The x-axes for the insets are on the same scale as the corresponding figure panels; the y-axes range from 0 to 1. 75

Figure 12: Programmable material fabrication using engineered pattern-forming bacteria. A. The curli-pattern circuit is built upon a pattern-formation circuit developed by Payne et al.[24]. The original circuit consists of T7RNAP that activates its own expression as well as the expression of LuxR and LuxI. LuxI mediates synthesis of AHL, which in turn, through activation of LuxR, drives expression of T7 Lysozyme and an mCherry reporter. In the revised circuit, CsgA containing a 6×-His tag is co-expressed with the lysozyme and mCherry. When expressed in a host strain producing CsgB, CsgA and CsgB will form curli that can interface with inorganic materials. B. Material assembly by pattern-forming bacteria. Bacteria containing the curli-pattern circuit can form self-organized curli patterns in each colony. The curli pattern can serve as the scaffold to assemble inorganic materials. The colony and the corresponding curli pattern are both programmable by gene circuit parameters and the growth environment. C. The bacterially assembled materials are used as modules for building functional devices. The schematic illustrates a "touch pad", that could sense and transduce local pressure variations. The dome shape represents the micro-structured material made from the colony; the orange lines represent conductive wires; and the two blue planes represent supporting surfaces. 83

Figure 13: Bacterial growth and pattern formation on permeable membranes. A. Growing colonies on a permeable membrane. I loaded 0.3% molten agar in 2×YT with IPTG and appropriate antibiotics in a Culture Well™ multiwell chambered coverslip (Grace Bio-Labs) as the culturing device. After the agar solidified, I placed a permeable membrane on top of the culture well and printed bacteria onto the membrane surface. The diagram is not to scale. B. Tunable dome structures on membranes with different

pore sizes. Each column represents the heat map of mCherry fluorescence patterns measured by a confocal microscope after 32 hrs incubation in both vertical (y-axis) and radial (x-axis) directions. The pore size varied from 0.03 to 0.4 μm, as indicated. The contact angles of these membranes varied slightly (from left to right: 64.0º, 59.0º, 58.5º, 57.7º, 55.3º). C. Simulated dome structures on membranes with varying pore sizes. In our model, I assume that the pore size affects the radius expansion rate v and the nutrient influx rate α1 (Eqs. (2) and (3)), respectively. Each column represents the heat map of simulated mCherry fluorescence patterns for the varying pore sizes. D. Experimentally tunable dome pattern on membranes with different contact angle. Each column represents the heat map of mCherry fluorescence patterns measured by a confocal microscope after 32 hrs incubation in both vertical (y-axis) and radial (x-axis) directions. From left to right, the membrane is PVDF, PC, MCE, NC. The pore size of each membrane is 0.45 μm. Contact angle of each membrane is 134.3º, 63.1º, 38.0º, 1.7º. The most left image is colony directly grow on 0.3% 2×YT (PH=6.5) agar. E. Simulation results of dome pattern on membranes with different contact angle. In our model, I assume varying contact angle affects the radius expansion rate v follows Eq (2). Each column represents the heat map of mCherry fluorescence patterns after simulation with different v. 87

Figure 14: Patterned gold nanoparticles as a resettable pressure sensor A. Controlled compression of two opposing colonies. The distance indicates the displacement of the presser from its starting position. The presser starts to make contact with the device when the displacement is >1 mm. B. Status of two colonies at different time point. Different time points are labeled in Figure 14A. The yellow-blue dome shape represents the colony; yellow dome represents the cells within the colony with gold assembly. The inset image is a higher magnification of the yellow section at nanoscale: gold nanoparticles bind on curli. At time point 3, upon making contact, the two colonies would experience increasing pressure with an increasing displacement distance. C. Colonies with uniform gold nanoparticles exhibited no differential response to pressure. With uniform expression of induced curli in a colony, gold nanoparticles were uniformly assembled throughout the colony, as illustrated as the yellow solid spherical cap on the right-hand side. Magenta and orange lines indicate currents from colonies grown on membranes with a pore sizes of 0.03 μm and 0.1 μm, respectively. The black line indicates response of colonies of pattern-forming bacteria grown on membrane with a pore size of 0.03 μm, without assembling gold nanoparticles (illustrated as the red hemispheroids on the right-hand side). The red arrows indicate the electric current pathway. D. Intensity of electric current as a function of the pressing distance for colonies not containing dome structured gold nanoparticles. The left panel shows responses from a pair of colonies grown on a membrane with a pore size of 0.03 μm. The

light magenta line indicates a varying pressing distance from 0 to 1.5 mm; the magenta line indicates a varying pressing distance from 0 to 1.8 mm. The middle panel shows responses from a pair of colonies grown on a membrane with a pore size of 0.1 μm. The light orange line indicates a varying pressing distance from 0 to 1.5 mm; the orange line indicates a varying pressing distance from 0 to 1.8 mm. The right panel shows responses of a pair colonies of pattern-forming bacteria grown on a membrane with a pore size of 0.1 μm, without assembling the gold nanoparticles. The gray line indicates a varying pressing distance from 0 to 1.5 mm; the black line indicates a varying pressing distance from 0 to 1.8 mm. E. Colonies with the dome structure exhibited differential pressure responses. The red, blue and green solid lines indicate responses from colonies grown on membranes with pore sizes of 0.05 μm, 0.2 μm, and 0.4 μm respectively. The dashed blue line indicates replicate experiment of the solid blue line by using different electrochemical machine of the same model on a different day. The right-hand side illustrates colonies containing dome-structured gold nanoparticles. The red arrows indicate the electrons travel pathway. F. Intensity of electric current as a function of the pressing distance for colonies containing dome structured gold nanoparticles. The left panel shows responses from a pair of colonies grown on a membrane with a pore size of 0.05 μm. The light red line indicates a varying pressing distance from 0 to 1.5 mm; the red line indicates a varying pressing distance from 0 to 1.8 mm. The middle panel shows responses from a pair of colonies grown on a membrane with a pore size of 0.2 μm. The light blue line indicates a varying pressing distance from 0 to 1.5 mm; the blue line indicates a varying pressing distance from 0 to 1.8 mm. The right panel shows responses of a pair colonies of pattern-forming bacteria grown on a membrane with a pore size of 0.4 μm. The light green line indicates a varying pressing distance from 0 to 1.5 mm; the green line indicates a varying pressing distance from 0 to 1.8 mm. 90

Figure 15: Patterned gold nanoparticles respond to pressure derivatives. A. The pressing distance as a function of time, with the same device configuration as in Figure 14. B. Distributions of gold nanoparticles corresponding to different pressure inputs. 1) the pressure is zero; 2) the pressure and its derivative are both positive; 3) the pressure is positive, but its derivative is zero. The three time points are labeled in Figure 15A. C. The pressure sensor responded strongly to changing pressure. The blue and green solid lines indicate current responses from colonies grown on membranes with pore sizes of 0.2 μm and 0.4 μm, respectively. 94

Figure 16: Robust signal processing by the bacterial pressure sensors. A. Control of an LED light using a bacterial pressure sensor in response to manual operation. The images indicate LED light intensities when the sensor was pressed to varying degrees or released. Also see Supplementary Video 1. All electronic components were from

Electroninks Inc. B. Construction of a noise filter and a signal amplifier using bacterially assembled gold domes. As in Fig. 3E, the input is the pressing distance as a function of time. Two sets of colonies were grown on the membranes with pore size of 0.2 μm and 0.05 μm, respectively. Panel i use the sets of small domes; panel ii use the sets of large domes; panels iii and iv are used the combination of the small and large sets of domes, but with different circuit design. Right of panel i and ii: the electric current readouts of these two sets of colonies being pressed separately. However, after combining the same sets of colonies with more complicated designs of the electronic circuits (panels iii and iv), substantial changes in the current signal were observed. Right panel iii: because the applied voltage polarities were opposite, the current signals from two sets of colonies cancelled out. Only the current with higher amplitude was selected, therefore, the electronic circuit combined with the colonies functioned as a noise filter. Right panel iv: because the applied voltage polarities were the same, current signals from two sets of colonies summed up. Hence, the output was amplified in the form of the original input signal, and the electronic circuit functioned as a signal amplifier. The x and y axis are of the same scale among i-iv panels. 96

Figure 17: Construction of pattern-curli circuit. A. TEM image of MG1655 ΔcsgA cells after 24 hrs incubation at 30 ˚C. The scale bar is 200nm. B. TEM image of MG1655 ΔcsgA cells carrying the curli-pattern circuit incubated after 24 hrs incubation at 30 ˚C. The scale bar is 500nm. C. Crystal violet (CV) staining assay of MG1655 ΔcsgA cells carrying the curli-pattern circuit and MG1655 ΔcsgA cells carrying inducible curli circuit. CV staining assay is a standard method to stain amyloid[168]. In this case, the presence of CV stain (blue) indicates the production of curli fibril. Both samples were washed in 1× PBS for three times, then immersed in 500 μL 0.1% CV solution (Sigma) for 15 mins at room temperature. After that, the samples were washed with 1× PBS four times. Left: there was no detectable CV stain in the absence of AHL-mediated CsgA induction. Middle: CV stain was detected when CsgA was induced by 50 nM AHL. Right: CV stain was detected when bacteria carrying the curli-pattern circuit were induced by 1000 μM IPTG. D. OD600 of CV stain dissolved in acetic acid. The samples in Figure 17C were immersed in 500 μL of 30% acetic acid for 15 mins at room temperature. The ODs of dissolved solutions were measured at 600 nm absorbance using a Perkin-Elmer VICTOR3 plate reader. MG1655 ΔcsgA curli-pattern circuit was used in this measurement. Circuit was induced by different amount of IPTG and AHL. E. TEM images of curli secreted from MG1655 ΔcsgA carrying the curli-pattern circuit assembling with 5 nm NiNTA-AuNP. Before assembly, cells were incubated at 30 ˚C after 24 hrs. Then 5 nm NiNTA-AuNP were assembled to curli using the protocol described as NiNTA-AuNP labelling. The scale bar is 100nm. Right: TEM image at larger magnification with scale bar of 50 nm. F. TEM images of curli secreted from MG1655

ΔcsgA carrying the curli-pattern circuit binding with gold nanogold using immunolabeling. The 6×-His tag first binds with 1st antibody (mouse anti-6× His tag antibody conjugated with biotin); then 1st antibody binds to 2nd antibody (goat anti-mouse IgG conjugated with 10 nm gold). By this means, 10 nm gold nanogold particles were assembled to the curli. The scale bar is 500nm. Right: TEM image at larger magnification with scale bar of 200nm. G. TEM images of curli immunolabeling with 2nd antibody without 1st antibody. Antibody agents and constructs were maintained the same with Figure 17F. The scale bar is 500nm. H. TEM images of curli secreted from MG1655 ΔcsgA carrying the curli-pattern circuit binding with quantum dots (Qdots) using immunolabeling. The 6×-His tag first binds with 1st antibody (mouse anti-6× His tag antibody conjugated with biotin); then 1st antibody binds to 2nd antibody (Streptavidin-655Qdots). The scale bar is 200nm. Right: TEM image at larger magnification with scale bar of 100nm. 102

Figure 18: Bacterial growth and pattern formation on permeable membranes. A. Printing bacteria on a membrane. An initial overnight LB culture of MG1655 ΔcsgA carrying the full gene circuit was grown for 16 hrs at 37 ˚C. 0.3% molten agar in 2×YT (PH = 6.5) medium was prepared. While allowing it to cool, I diluted the overnight culture to an OD of 0.2, and then diluted the resulting culture another 50 fold into 10 mL fresh LB culture before loading it into the inkjet printer cartridge. After the agar cooled down to 50 ˚C, IPTG and appropriate antibiotics were added. 170 μL of the agar was added to each culture-well. After the agar solidified, a permeable membrane was placed on top of the agar. I then used the inject printer to print the bacteria solution onto the membrane surface. After incubating the whole device under 30 ºC for 32 hrs, the permeable membrane carrying the colony was carefully removed by using a tweezer. B. Heights and radii of colonies growing on PC membranes with different pore sizes after 32 hrs incubation at 30 ˚C. The heights and radii were extracted by a custom MATLAB image analysis code from the confocal microscopy[28]. The contact angles of these membranes were 64.0º, 59.0º, 58.5º, 57.7º, and 55.3º (corresponding to increasing pore sizes). C. Simulated heights and radii of colonies when the radius expansion rate $\boldsymbol{v}$ and the nutrient influx rate $\boldsymbol{\alpha 1}$ were varied according to Eqs (2) and (3), respectively. D. Heights and radii of colonies growing on membranes with different contact angles after 32 hrs incubation at 30 ºC. The heights and radii were extracted the same way described in Figure 18B. The pore size for all the membranes was 0.45 μm. Contact angles were 1.7º, 38.0º, 63.1º, and 134.3º. E. Simulated heights and radii of colonies when the radius expansion rate $\boldsymbol{v}$ was varied according to Eq (2). 106

Figure 19: Generation of structured materials using bacteria carrying the curli-pattern circuit. A. Assembly of nanoparticles to a colony of bacteria carrying curli-pattern

circuit. I first fixed the colony, and then used the immunolabeling to bind nanoparticles to the colony. B. Gold particles distribute similarly as mCherry in colonies. To examine if curli was co-expressed with T7 Lysozyme sufficiently, I compared the mCherry signal with the emission signal from the patterned nanoparticles. Left column: cells carrying curli-pattern circuit were grown on a PC membrane with a 0.4 μm pore size. Gold nanoparticles conjugated with an Alexa Fluor 488 fluorescent dye (a bright, green-fluorescent dye with excitation ideally suited to the 488 nm laser line, Thermo Fisher Scientific) were assembled onto the colony through immunolabeling. The colony was excited at 435 nm (CFP channel), 555 nm (mCherry channel), or 488 nm (green channel) during confocal microscopy. The mCherry signal matched with the emission signal from Fluor 488 dye very well: both form dome structures, indicating that gold particles distribute similarly as mCherry within the colony. Middle column: cells carrying curli-pattern circuit were grown on PC membrane with 0.03 μm pore size. No gold nanoparticles were assembled onto the colony. When the colony was excited at 488 nm, no emission signal was detected. This proved the signal observed in the left column bottom panel was emitted from the Fluor 488 dye, not from the colony itself. Right column: bacteria carrying the inducible curli circuit were grown on a PC membrane with a 0.03 μm pore size. Gold nanoparticles conjugated with the Alexa Fluor 488 fluorescent dye were assembled on colony through immunolabeling. These bacteria did not express CFP or mCherry reporter. When excited at 488 nm, the emission signal from the Fluor 488 dye formed a solid spherical cap, instead of a dome (Fig. 3D). C. TEM of bacteria scooped from the outer-layer of the colony (shell part) carrying curli-pattern circuit after immunolabeling. The colony was grown on top of a PC membrane with a 0.4 μm pore size. The TEM image shows 10nm gold nanoparticles bound to curli fibrils. This result shows that the bacteria from the curli dome have efficiently assembled the nanoparticles. 108

Figure 20: Assembly of the pressure sensor. A. Design concept. Black lines represent conductive wires. In the absence of pressing, the two colonies are separate and there is no electric current passing through. When pressed together lightly, a small current can go through the two colonies via their contact. The current increases with increasing pressure that enhances the contact. B. Implementation of the sensor. Two PC membranes carrying colonies were mounted to the surfaces of two glass covers with nitrocellulose (Electron Microscopy Science, 72180). Copper wires were used to link the edge of the colony. The two glass covers (each carrying a colony) were placed to face each other with a 0.5 mm spacer (Grace Bio-Labs Press-To-Seal silicone isolator) in between. The other ends of both copper wires were linked to the positive and negative terminals of an electrochemistry workstation. A syringe needle controlled by a programmable syringe pump was used as a “presser” (18ga × 1.5", Blunt Tip) to press the colony sensor. The

diameter of the syringe needle was 1.5 mm. It was placed 1 mm right above the top of the glass cover. The top projection of the cylinder aligned with the location of the colony. C. Configuration of the overall testing device for the pressure sensor. The electrochemical workstation provides a constant voltage, and measures and records the electric currents resulting from the bacterial pressure sensors. 109

Figure 21: Multi-colony location sensors. A. Design of two-colony, three-colony, and four-colony location sensors. Similar to Figure 20, in each device, colonies and conductive wires were mounted onto two membranes. Mounted to the bottom membrane, the yellow wires connected colonies to the negative terminal of the voltage. Mounted to the top membrane, the red wires connected colonies with to positive terminal of the voltage. To differentiate which colony was pressed, I labelled them a, b, c, and d based on the locations. Note: red and yellow wires are the same type of conductive copper wires. B. Current responses to pressing at different locations. The top panel indicates the pressure input – the pressing distance as a function of time at different locations. When applicable, the first pulse was applied to location 'a', the second pulse to 'b', the third pulse to 'c', and the forth pulse to 'd'. The bottom panel indicates the current responses from pressing at different locations. In the same device and at the same strength of pressing, the amplitude of the output current is determined by the location of the pressing. For example, in 2-colony device, the peak current from location 'b' is higher than location 'a'. The pore size of all the membranes used in this set of experiments were 0.1 μm. 110

Figure 22: Pattern formation in multiple colonies. A. Composite fluorescent images of colonies and patterns from multiple initial seeding positions. All images were taken after 32 hrs incubated at 30°C. B. mCherry fluorescent channels of (a). C. Simulated mCherry patterns using our PDE model using comparable seeding configurations. 125

Acknowledgements

I want to give the biggest thank you to my advisor, a mentor, a friend, and an amazing listener: Dr. Lingchong You. The discussions and conversations with him are always insightful and inspirational. From him, I learned not only how to conduct research smartly and efficiently, but also how to be generous and collaborative. Without his help and mentorship, I would have never made it this far.

My collogues and friends from You Lab are important and non-replaceable existences in my life. They are the ones who helped me taking out the plates when I am lazy being somewhere; they are the ones who laugh or cry with me when things are good or bad; they are the ones who sit next to me, look at my data and try to help me interpret them. A special shout out to Hannah, who is not only my colleague, but also my best friend. I will never forget the time she brought her pillow to my house just to be with me to pass those sad moments.

I would also like to thank my committee members: Dr. John Neu, Dr. Fan Yuan, Dr. Stefan Zauscher, Dr. Katia Koelle for their patient guidance. In particular, I want to thank Dr. Neu. I have learned so much by deriving the math equations with him. His passion and interests toward unsolved problems have tremendously positive effects on me. I also want to thank Dr. Zauscher for spending so much of his valuable time to hear and improve my projects.

I cannot express how gratitude toward the people I have met in my life that have helped me. You are the reasons of I am who I am.

1. Overview

Most synthetic biological systems are not only capable of providing better understanding of natural systems, but can also be the basis for various practical applications. Patterns are ubiquitous in living organisms. However, the mechanisms driving self-organized pattern formations are not well understood. Due to the complexity of natural systems, many confounding factors complicate quantitative experiments and data interpretation, often making it difficult to draw definitive conclusions. Therefore, a limited number of experimental systems could enable precise perturbation and quantification of pattern formation. In comparison, the synthetic system serves as well-defined model systems to elucidate ''design principles'' of biological networks.

Intrigued by the challenge, my colleagues and I programmed *E. coli* with a synthetic gene circuit to generate self-organized pattern formation. This pattern-forming system also has the potential for future applications in the generation of patterned biomaterials.

1.1 Objectives

The objectives of my thesis are to use a synthetic-biology approach to (1) investigate the mechanism that underlies scale invariance in self-organized pattern formation without morphogen gradient, (2) utilize the bacterial patterns as templates to generate self-organized inorganic materials with special functionality. In specific:

Objective 1: Model and quantify pattern formation process and scale invariance in depth

This includes: model pattern formations and scaling properties under different experimental conditions and investigate generations of sophisticated patterns experimentally and computationally.

Objective 2: Use engineered bacteria to generate structured materials with well-defined physical properties.

This includes: intergrade pattern-forming circuit and effector genes to generate patterns that interface with inorganic materials; investigate the special physical properties of the organic-inorganic structure and develop it into an application.

1.2 Organization of the objectives

The organization of the dissertation is divided into three Chapters.

Chapter 2 identifies the essential factors to form periodic patterns. Particularly, this chapter discussed the specific roles of these elements in promoting or attenuating oscillatory dynamics, by drawing insights learned from the quantitative analyses of natural or synthetic biological networks in single cells or cell populations.

Chapter 3 describes scale invariant self-organized core-ring patterns programmed by engineered *Escherichia coli*. The analysis in this chapter revealed a collective space-sensing mechanism, which entails sequential actions of an integral feedback loop and an incoherent feedforward loop. The integral feedback is

implemented by the accumulation of a diffusive chemical produced by a colony. This accumulation, combined with nutrient consumption, sets the timing for ring initiation. The incoherent feedforward is implemented by the opposing effects of the domain size on the rate and duration of ring maturation. This mechanism emphasizes a role of timing control in achieving robust pattern scaling and provides a new perspective in examining the phenomenon in natural systems.

Chapter 4 describes the programmable, three-dimensional (3D) material fabrication using pattern-forming bacteria growing on top of permeable membranes as the structural scaffold. We equip the bacteria with an engineered protein that enables the assembly of gold nanoparticles into a hybrid organic-inorganic dome structure. The resulting hybrid structure functions as a pressure sensor that responds to touch. We show that the response dynamics are determined by the geometry of the structure, which is programmable by the membrane properties and the extent of circuit activation. Taking advantage of this property, we demonstrate signal sensing and processing using one or multiple bacterially assembled structures.

2. Generation of Periodic Patterns[1]

Periodic patterns are ubiquitous in nature. Depending on the biological contexts, the molecular mechanisms and the components underlying the generation of these dynamics are extremely diverse. Cutting across this diversity, however, several regulatory elements have been recognized as critical in generating and modulating oscillatory dynamics. These include negative feedback, time delay, positive feedback, nonlinearity in regulation, and random fluctuations ("noise") in cellular processes. Here I discuss the specific roles of these five elements in promoting or attenuating oscillatory dynamics, by drawing insights learned from the quantitative analyses of natural or synthetic biological networks in single cells or cell populations.

2.1 Introduction

Oscillatory dynamics are prevalent in all facets of life. Spatial oscillatory behavior can give rise to periodic patterns, such as skin patterns and vertebrate segmentation [1, 2].

Extensive studies have been conducted to elucidate the molecular mechanisms underlying the generation of oscillatory dynamics (reviewed in [3-5]). Depending on the contexts, the mechanisms and the associated molecular components underlying

---

[1] The content of this chapter has been published. Cao Y*, Lopatkin A*, You L. Elements of biological oscillations in time and space. Nature Structural & Molecular Biology. 2016 Dec 1;23(12):1030-4. (* Equal contributions).

Author contributions: Y.C., A.L., and L.Y. wrote the manuscript.

oscillatory dynamics are extremely diverse in network complexity, temporal and spatial scales, and biological functions. For example, periodic patterns can emerge from oscillatory dynamics in single cells, with a length scale of <1μm [6], or in groups of cells or multi-cellular organisms with scales reaching up to meters in length [7].

Despite all this diversity, however, five elements are recognized as critical in generating or modulating spatial oscillatory dynamics. These are: negative feedback, time delay, positive feedback, nonlinearity in regulation, and noise (Figure 1). These elements contribute to one or multiple aspects of oscillatory dynamics. Moreover, depending on the overall network architecture, each element can either enhance or attenuate generation of oscillations. Here I discuss these contributions by drawing insights learned from quantitative analysis of natural and synthetic biological systems. Natural systems define the biological context and scope of existing oscillatory behavior, while synthetic systems provide an effective platform to test specific network components within a more controllable framework [8, 9]. Together, such examination provides general insights into the role of various design elements within biological oscillations for both basic biological understanding and for practical applications.

2.2 Elements to generate periodic patterns

In space, oscillatory dynamics can result in well-defined periodic patterns [3], and has been extensively studied in animal embryonic development [1, 10]. For example, formation of somites in vertebrate embryos is controlled by a molecular

oscillator, the segmentation clock [11]. The segmentation clock generates a temporal periodicity that can be translated spatially into the periodic boundaries of the somites [12, 13]. Similar to the generation of temporal oscillations, one or more of the five elements are required to generate oscillations in space. Again, negative feedback is the most fundamental requirement.

Incorporating time delay with negative feedback can enhance the robustness of spatial oscillations. In the segmentation clock, negative feedback is realized through Notch signaling [14, 15]. In the segmentation clock of zebrafish, multiple layers of negative feedback are involved in the periodic activation of Notch. Notch will then drives expression of *Her1* and *Her7*, which establish negative-feedback regulation by suppressing their own expression[14]. The delayed negative feedback due to intracellular inhibitory loop is thought to be the fundamental generator of the oscillations of the segmentation clock [16, 17]. In turn, a secreted growth factor (FGF 8) is suggested to convert temporal oscillations into the periodic somite boundaries [18, 19].

Similarly, Liu et al found that metabolic limitation in *Bacillus subtilis* biofilm formation creates a delayed negative feedback loop between peripheral and internal cells, generating oscillations during colony expansion [20]. The authors showed that consumption of glutamate from the cells in the periphery of the colony inhibits ammonium production from the interior cells. Since ammonium production promotes glutamate consumption, this interplay creates a delayed negative feedback in the

glutamate consumption in the peripheral cells, therefore, caused oscillatory dynamic of the colony growth (Figure 1A) [21].

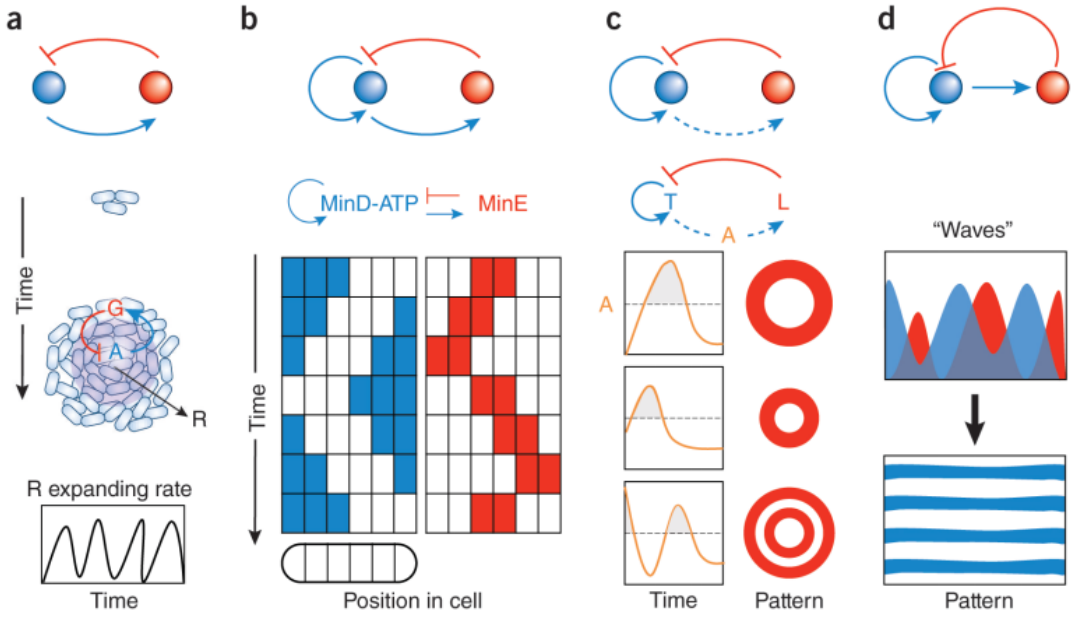

Figure 1: Generation of periodic patterns. A. Delayed negative feedback emerges from the interplay between two subpopulations in a colony [21]. During cell growth, consumption of glutamate from cells at the periphery of the colony is triggered by ammonium. At the same time, glutamate limits ammonium production from the interior cells. This process leads to oscillations in the colony radius expanding rate over time. B. Positive feedback integrated with negative feedback. During cell division, MinD and MinE oscillate from one pole to the other. Eventually, MinE precisely locates the center of the cell to determine the correct location for forming a ring-like structure [22, 23]. C. Positive feedback integrated with negative feedback with various time delays. By adjusting the initial concentration of AHL, AHL dynamics change over time (left panel). Different size and number of periodic patterns can be formed [24]. D. Positive feedback integrated with negative feedback. The activation module is local, whereas inhibition is long range. This basic reaction-diffusion model is a basic mechanism for generating periodic Turing pattern. Activator and inhibitor form waves in space, leading to periodic patterns.

Positive feedback coupled with delayed negative feedback (relaxation oscillator) is another common way to increase robustness in spatial oscillations. During bacterial cell division, three proteins oscillate from pole to pole (MinC, MinD, and MinE). Their oscillations are critical for determining the correct location for forming a ring-like structure around the center of the cell [25-27]. Studies have shown the positive feedback increases the robustness of MinD oscillation [22, 23], contributing to the precision of cell division at an accurate location (Figure 1B).

At the population level, Payne et al. demonstrated genetically programmed *E. coli* could generate robust, self-organized ring patterns of gene expression. A fast-diffusible molecule, AHL, is secreted by a positive feedback loop. When the concentration of AHL is high enough, downstream negative feedback is activated. AHL dynamics are responsible for triggering the formation and maintenance of ring patterns. The delayed time period to regulate the negative feedback loop could be modulated by adding exogenous AHL. Double-ring pattern or multiple ring patters could be generated experimentally and computationally by modulating the negative feedback loop (Figure 1C) [24]. Indeed, using the same system, Cao et al. demonstrated scale invariant ring patterns regulated by sequential actions of an integral feedback and incoherent feed-forward loop [28].

Liu et al. adopted this network architecture in a synthetic gene circuit engineered to generate periodic stripe patterns in a growing bacterial colony [29]. The circuit

contains a density-sensing module through the synthesis and release (by diffusion) of a QS molecule AHL. At a high enough concentration, AHL triggers downstream gene expression that suppresses cell motility. Cells carrying this circuit sequentially form alternating high-low density stripes (periodic patterns). The circuit embeds positive feedback consisting of mutual inhibition: high cell density leads to a reduction in the cell motility, and high cell motility will decrease the local cell density. Additionally, the delayed negative feedback arm is formed between nutrient and cell density. By inducing rate of the inhibition arm from cell density to cell motility, authors indirectly modulate the strength of the positive feedback loop. By this mean, different number of stripes could be formed in space [29].

By far, the most mathematically studied nonlinear system is the reaction-diffusion mechanism, which is the core for Turing pattern formation [30]. Despite the appeal of the Turing mechanism, however, the number of direct experimental demonstration of Turing pattern formation [2, 31] is far less compared to mathematical demonstrations. Among the experimental results, Nakamasu et al. demonstrated that nonlinearities of local activation and long-range inhibition in zebrafish are the necessary conditions for periodic pattern formation, as predicted by mathematical studies [32] (Figure 1D).

As with temporal oscillations, noise is often detrimental by introducing variability and disrupting pattern formation [33, 34]. However, in certain instance,

instability driven by noise could enhance the robustness and sustainability of spatial oscillations. Given a deterministic reaction-diffusion model, the system is able to generate periodic Turing patterns. Maini et al. showed a stochastically excited system could form patterns more rapidly than its deterministic counterpart. Additionally, noise inherent in stochastic systems is able to produce more sustained patterns [35]. To date, however, noise-induced pattern formation has yet to be demonstrated experimentally.

2.3 Perspectives

Periodic pattern formation in biology is critical for defining the body plan during development. Understanding the basic elements driving the generation of spatial oscillations could draw insights on how self-organized system-level integrated oscillations are achieved during embryonic development. However, a periodic pattern by a biological circuit can also be considered as spatial manifestation/encoding of the environmental signals. For example, in bacteria, the efficiency of forming the division ring (determined by oscillatory Min system) is nutrient-dependent [36, 37].

Considering the vast diversity and complexity of oscillating biological systems, it is advantageous that most, if not all, of them can be reduced to a combination of a few basic elements. This simplicity can facilitate the analysis and interpretation of biological oscillations in defining the roles of specific molecular components. In the study of natural biological oscillators, the role of feedback control is well appreciated. In contrast, the consequences of time delay, noise, and nonlinearity are less explored and more

challenging to address. This prospect is made even more difficult, as the role of each element may be context-dependent. Noise can either promote or suppress oscillatory behavior depending on the system. Also, identical motifs might generate oscillations in one system but not in another one due to differences in relevant parameter ranges depending on the environment. However, understanding how these dynamic elements emerge from molecular components may be critical for understanding the biological roles of the latter.

3.Collective Space-sensing Coordinates Pattern Scaling in Engineered Bacteria[1]

3.1 introduction

Scale invariance, or the maintenance of constant relative size of an organ with respect to the whole body during animal development, or between individuals, is a common phenomenon in biology [38, 39]. For example, in the *Drosophila* embryo, the imaginal discs are segmented to scale with the embryo size [40]; in the vertebrate neural tube, the ventral neuroepithelium subdivides into neural progenitor domains with precise positional information [41, 42]. For natural systems, scale invariance of pattern to size is a major, but unsolved, problem in developmental biology. Several reviews have noted the difficulties of studying pattern scaling [43-45]. A major challenge is the limited number of experimentally tractable systems to enable precise perturbation and quantification of pattern scaling. Less than a quarter of the animal models used for studying pattern formation are used to study scale invariance [46]. Moreover, the networks underlying pattern formation or scaling in existing model organisms are often

---

[1] The content of this chapter has been published. Cao Y, Ryser MD, Payne S, Li B, Rao CV, You L. Collective space-sensing coordinates pattern scaling in engineered bacteria. Cell. 2016 Apr 21;165(3):620-30

Author contributions: Y.C. generated and analyzed all the experimental data and discovered the scale invariance in pattern formation. M.D.R. developed the final version of the PDE model and the corresponding numerical solver. Y.C. and L.Y. assisted in formulating the model. S.P. constructed the gene circuit. S.P. proposed the use of inkjet printing and carried out initial experiments with Y.C.. S.P. and Y.C. developed MATLAB codes for image analysis. B.L. developed an initial version of the PDE model. Y.C. developed the parameter search algorithm and generated all simulation results. Y.C., C.V.R., and L.Y. formulated the control interpretation of the collective space sensing mechanism. Y.C., M.D.R., and L.Y. wrote the manuscript, with inputs from B.L., S.P., and C.V.R..

highly complicated, making it difficult to tease out generally applicable design principles. Most proposed mechanisms that explain pattern scaling are theoretically based.

When pattern formation is driven by one or more morphogen gradients, scale invariance can be explained by several mechanisms [47-49]. Analogous mechanisms have been proposed to examine the scale invariance of system responses to varying inputs [50]. In a source-sink mechanism [51], a diffusible morphogen is generated from a source at the center of the system and degraded at the system boundary, which can establish a linear gradient from source to sink regardless of the system size. When two opposing gradients are involved, their ratio as a function of the spatial coordinate can exhibit scale invariance, which in turn can generate scale-invariant patterns [52]. Alternatively, a system may adopt feedback to adjust the scaling of a morphogen gradient. In particular, the expansion-repression mechanism, whereby a system produces fast-diffusing chemicals that suppress the morphogen, can lead to a gradient that scales with the body size [53, 54].

Studies have indicated that pattern formation may not require morphogen gradients [55, 56]. Such patterns are much less studied in comparison to those relying on morphogen gradients. It remains unknown whether and how scale invariance might emerge in such systems. Addressing this question is challenging, in part due to the complexity of natural systems, where many confounding factors complicate quantitative

experiments and data interpretation. To overcome this limitation, we set out to examine the scaling dynamics of pattern formation in *E. coli* programmed by a synthetic gene circuit that Stephen Payne previously developed (Figure 2A) [24]. The circuit consists of a mutant T7 RNA polymerase [57] (T7RNAP) that activates its own expression and that of LuxR and LuxI. LuxI synthesizes an acyl-homoserine lactone (AHL), a membrane-diffusible chemical that upon binding and activating LuxR, can induce expression of T7 lysozyme. Lysozyme inhibits T7RNAP by forming a stable complex with it. The T7-lysozyme complex inhibits the transcription of T7RNAP as well [58]. CFP and mCherry fluorescent proteins are co-expressed with T7RNAP and lysozyme, respectively, to report the circuit dynamics.

As AHL is highly diffusible, its spatial gradient is negligible over the length scale of pattern formation in this system. All else being equal, the time required for AHL to reach a critical concentration is inversely proportional to the size of the growth environment. Therefore, the production and accumulation of AHL enables a growing colony to collectively sense the domain size and to time the pattern formation accordingly [24]. This sensing property suggests an opportunity to quantify pattern scaling in a well-defined experimental platform. Indeed, by using this system, we found a simple mechanism by which scale invariance can emerge without the need to scale the gradient of a diffusible morphogen.

3.2 Results

3.2.1 Scale invariance emerges from programmed pattern formation

I adopted an inkjet-printing technique to precisely control the inoculum size and the location of the initial seeding cells (Figures 7A-C) [59]. Briefly, bacterial culture was used as "ink" and printed onto the surface of soft agar in a multi-well device. This technique ensured precise control over the initial spatial arrangement of colonies and the initial cell number (~20) in each colony. By changing the configuration of initial cell placements, I was able to modulate the effective domain size of the growth environment available for each colony (Figure 7D).

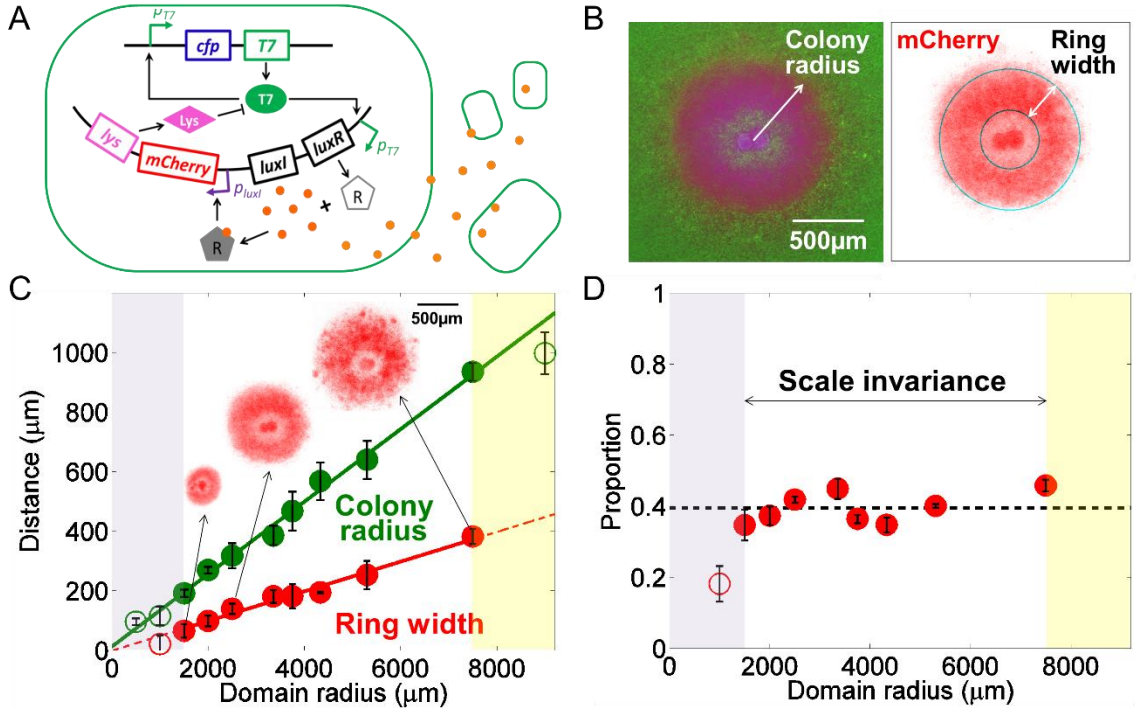

Figure 2: Scale invariance in self-organized pattern formation in engineered bacteria. A. **Circuit logic**. The circuit consists of a T7 RNA polymerase that activates its own expression as well as the expression of LuxR and LuxI. Upon activation by

T7RNAP (T7), LuxI mediates synthesis of AHL (A), which can diffuse across the cell membrane. When the global AHL concentration surpasses a threshold, intracellular AHL binds to LuxR to activate the synthesis of T7 lysozyme (L). Lysozyme then binds to the T7RNAP and forms a T7-lysozyme complex, therefore inhibiting the T7RNAP binding to the T7 promoter. This T7- lysozyme complex also inhibits T7RNAP transcription. In this process, the AHL concentration is affected by its initial concentration and the domain size. The expression rates of T7RNAP, lysozyme, and AHL are all controlled by the spatially dependent gene expression capacity. B. **Self-organized pattern formation in engineered bacteria.** *Left:* A composite fluorescent image. *Right:* mCherry image extracted by MATLAB code from left composite image. Images of a 1.2mm × 1.2mm field of colony at 2500 μm domain radius after 24 h of incubation. The experimental platform used here was described in Figure 7A. C. **Scale invariance in self-organized pattern formation.** The mCherry ring width (red circle) and the colony radius (green circle) are plotted as a function of the domain radius. Measurements were done in microcolonies after 32 h incubation. The error bars represent the standard error from ≥5 replicates for each domain radius. The solid lines represent the linear regression of the data points (green: colony radius; red: ring width) for intermediate domain radii (between 1500 μm and 7500 μm), where scale invariance emerges (the R-square value for ring width vs. domain radius linear regression is 0.9828; the R-square value for colony radius vs. domain radius linear regression is 0.9943). The purple block corresponds to domain radii<1500 μm; the yellow block corresponds to domain radii >7500 μm. The insets show mCherry images for domain radii of 1500 μm, 2500 μm, and 3750 μm, respectively. For all of the presented figures, if unnoted, filled circles represent the data where ring width vs. colony radius follows a linear regression with domain radius. D. **Ratio of mCherry ring width to colony radius for different domain radii.** The ratio was calculated from the data in Figure 1C. The dashed line shows the average ratio for data points within the range of domain radii where the scale invariance emerges. The standard deviation of the ratio values between 1500 and 7500 μm is 0.0448 (~10% of the total constant ratio).

Figure 2B shows a typical self-organized pattern in a microcolony at 24 h after incubation. The pattern consists of a core of high CFP and mCherry expression, as well as a wide peripheral ring of mCherry expression (see Figure 7E). This patterning process was reproducible (Figure 7F). In contrast, *E. coli* MG1655 cells not carrying the circuit did not generate these patterns under the same experimental conditions (Figure 7G).

The domain size plays a critical role in the observed patterning dynamics. No mCherry ring formed when the domain size was too small (<500 μm) or too large (>9000 μm). For intermediate domain sizes (between 1500 and 7500 μm), however, the ring width exhibited scale invariance with respect to the colony radius. Both were proportional to the domain radius (Figure 2C), leading to a constant ratio between them (Figure 2D).

3.2.2 Model reveals the essential requirement for scale invariance

The observed scale invariance is surprising, considering all of the diverse factors contributing to the patterning dynamics. Its simplicity suggests two possibilities. One is that the system parameters are extremely fine-tuned to generate such a simple outcome. Alternatively, beneath the apparent complexity of the circuit dynamics may be a simple regulatory core motif that ensures the observed outcome. If the latter is true, such a motif may define a generally applicable mechanism to generate robust scale invariance.

To address these issues, we formulated a set of partial differential equations (PDEs) to account for the circuit dynamics (see Supplemental Information), including intracellular gene expression and protein-protein interactions, bacterial growth and colony expansion (Figure 7H), and transport of intracellular components by cell movement [60]. Due to their fast diffusion and the geometry of device, AHL and nutrient were assumed to have uniform concentrations across space (Figure 8B). In our model, the term nutrient is used to refer to one or more factors that limit the overall

colony growth. Our model also accounted for the spatial variation in gene expression capacity across the colony: this capacity was highest near the colony edge (defined as the location where cell density is 95% of the carrying capacity) and decreased toward the interior of the colony. This empirical function lumps potential contribution of multiple factors, such as mechanical stress [61], cell-cell contact inhibition [62], and oxygen concentrations [63, 64].

The model has 22 parameters; we chose their initial values based on the literature data or biologically realistic estimates. Given the high dimensional parameter space, however, we did not attempt to determine one parameter set that best fits the experimental data - it would likely represent an overfit. Instead, we sought to determine the likelihood of finding some parameter sets able to generate the observed scale invariance, and then identify the commonalities among these parameter sets. To address these questions, I developed a search algorithm (see Supplemental Information) to explore the parameter space. I examined 18,231 parameter sets, in which I fixed all parameters that had been measured experimentally (Table 1) and varied the remaining nine parameters randomly in a pre-defined range of biologically meaningful values. For each parameter set, I simulated the patterning dynamics for varying domain sizes. I identified 409 parameter sets that produced mCherry core-ring patterns for varying domain sizes (Figure 3A, blue polygons). Of these 409 sets, 55 supported scale invariance (Figure 8C). This result underscores the notion that conditions underlying

scale invariance are much more stringent than those underlying pattern formation [46, 65, 66]. To determine the conditions underlying scale invariance, for each of the 409 parameter sets, I performed a local optimization to generate a parameter set that produced scale invariance (see Supplemental Information, and Figure 8D for further details on the optimization).

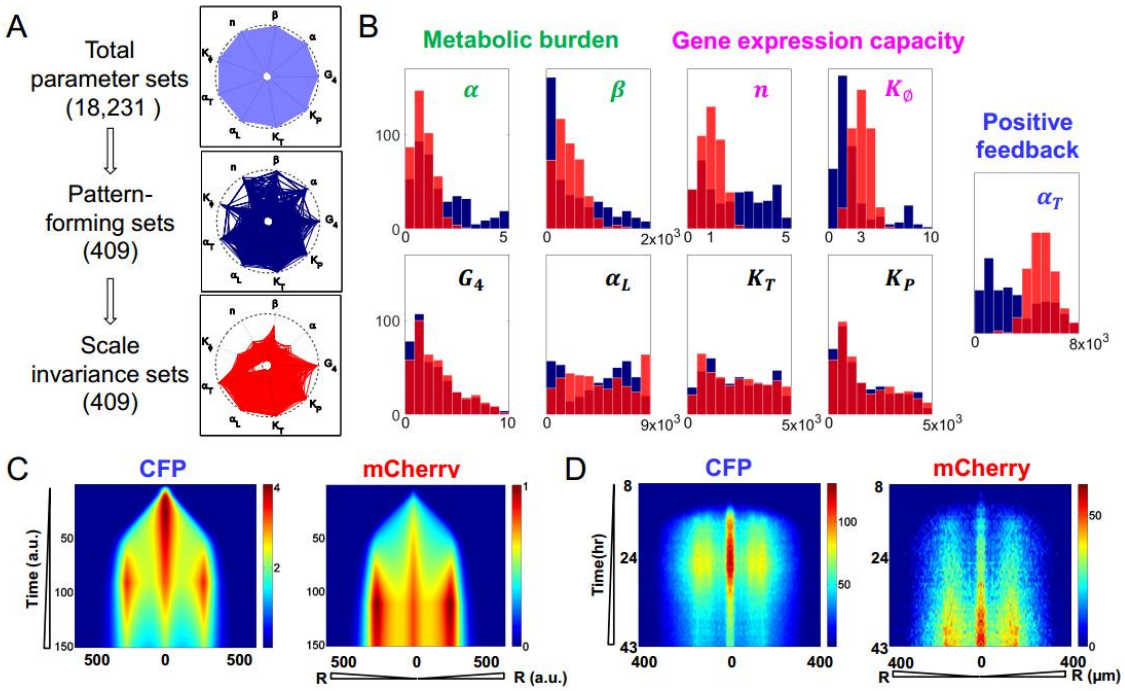

Figure 3: Pattern formation dynamics in engineered bacteria. A. **Parameter search.** Each spike represents the range of a parameter, ranging from 0 to its maximum value (the intersect with the outer circle) [67]. $\boldsymbol{G_4}$ was explored between 0 and 10; other parameters' search ranges are listed in Table 1. Each polygon represents a parameter set. I started with 18,231 parameter sets (light blue). Dark blue lines indicate 409 parameter sets that generated core-ring patterns for varying domain radii (from 1 to 3). A local search on each of these 409 sets led to an optimal parameter set that generated scale invariance (red curves). $\boldsymbol{\alpha}$ and $\boldsymbol{\beta}$ are the inhibition factors of T7RNAP and T7 lysozyme on cell growth, respectively. $\boldsymbol{n}$ is the Hill coefficient for distance-dependent gene expression capacity. $\boldsymbol{K_\varphi}$ is the half activation distance for gene expression capacity. $\boldsymbol{\alpha_T}$ and $\boldsymbol{\alpha_L}$ are synthesis rates of T7RNAP and T7 lysozyme, respectively. $\boldsymbol{K_T}$ and $\boldsymbol{K_P}$ are

half-inhibition concentration of T7RNAP and T7-lyszome complex, respectively. $\boldsymbol{G_4}$ is the synthesis rate of AHL, after non-dimensionalized. B. **Conditions underlying scale invariance.** Five parameters shifted systematically during the optimization step: $\boldsymbol{\alpha}$ **and** $\boldsymbol{\beta}$ characterize circuit mediated metabolic burden; $\boldsymbol{n}$ **and** $\boldsymbol{K_\varphi}$ determine the shape of gene expression capacity; and $\boldsymbol{\alpha_T}$ characterize the strength of T7RNAP feedback. In contrast, the four other parameters, $\boldsymbol{G_4}$, $\boldsymbol{\alpha_L}$, $\boldsymbol{K_T}$, and $\boldsymbol{K_P}$ did not change significantly during optimization. The blue histograms represent values from the 409 pattern-forming sets in Figure 2A before optimization. The red histograms represent values of the 409 sets resulting from the optimization. The light red is the overlap between blue and red histogram. C. **Simulated spatio-temporal profiles of CFP and mCherry intensity**. *Left*: Average CFP intensity over colony cross-section from 1 to 150 in arbitrary unit. *Right*: Average mCherry intensity over colony cross-section from 1 to 150 in arbitrary unit. **D. Experimentally measured spatio-temporal profiles of CFP and mCherry.** *Left*: average CFP intensity of bacterial colony at different radii from 8 h to 43 h. *Right*: Average mCherry intensity of bacterial colony at different radii from 8 h to 43 h. The experiments were measured at domain radius of 2500 μm.

Altogether, the parameter search and further optimization identified 409 parameter sets that generated scale invariance (Figure 3A). These parameter sets differed drastically from each other in terms of the range of the values I have searched for. This diversity suggests that scale invariance is a robust property that can be achieved by many combinations of parameters. I inspected the change of the parameter range during the optimization from pattern-forming sets to scale-invariance sets. Five parameters shifted in a consistent manner (Figure 3B). The final distributions of these parameters reveal three conditions for scale invariance. First, T7RNAP and lysozyme had minimal metabolic burden on cell growth, as indicated by reduced α and β values. Second, the gene expression capacity decreased slowly as a function of distance to the colony edge, as indicated by an optimal Hill coefficient (n) of around 1.0 and moderate width K_φ, which approximately matches the half-width of the colony wavefront. Third, the

T7RNAP positive feedback needed to be sufficiently strong, as indicated by increased α_T values. When these conditions were satisfied, the search algorithm identified a much greater fraction of parameter sets able to generate scale invariance, without further local optimization (Figure 8E).

The first two conditions distinguish the patterns reported here from those described previously [24]. This distinction is indeed consistent with the differences between the two experimental conditions, in terms of cell strains and experimental platforms (see the Supplemental Information for a detailed comparison). In particular, we measured growth of MC4100Z1 (the strain used in the previous study) and MG1655 (current study) cells carrying the pattern-formation circuit and its variants. These variants include the positive-feedback module, the pattern-formation circuit with the *luxI* gene knocked out, and the pattern-formation circuit with an effector gene co-expressed with the T7 lysozyme. Compared with MG1655 cells, MC4100Z1 cells experienced a higher metabolic burden when different circuits were induced. Furthermore, the pattern-formation circuit carrying an effector gene caused a higher metabolic burden than did the pattern-formation circuit by itself (Figure 8F). According to our simulation results, a high metabolic burden and a sharp gene expression profile would generate a narrow mCherry ring whose width does not show scale invariance with the colony size (Figure 8G, green boxed figure on left panel). These predictions are consistent with the experimental observation in the previous study [24].

Figure 3C shows simulated patterning dynamics from an optimal parameter set, which recapitulated the experimentally observed temporal dynamics of the CFP and mCherry pattern formation from 8 to 43 h (Figure 3D). Before the colony stopped expanding at ~12 h, CFP had accumulated to form a core at the center of the microcolony and a weak ring close to the colony edge. Its intensity continued to increase until ~26 h, when it began to decrease. Eventually, CFP decayed into a low and relatively flat profile (43 h). Because mCherry is controlled by T7RNAP via the LuxR/LuxI module, its dynamics lagged behind that of CFP. The mCherry core and ring emerged at ~16 h and kept increasing in intensity until the end of measurement. As a result, the mCherry pattern was much more sustained than that of CFP.

3.2.3 Scale invariance is mediated by a collective sensing mechanism

Inspection of the simulations reveals a collective space-sensing mechanism that underlies the patterning process and the resulting scale invariance. The growth environment acts both as a nutrient reservoir for colony growth and as a sink for AHL produced by the colony (Figure 4A). Everything else being equal, the rate of AHL accumulation decreases with the domain size. Therefore, the production and accumulation of AHL enables a colony to sense the domain size and to coordinate patterning. In other words, the domain size controls the pace and extent of colony expansion by determining nutrient availability. It also controls the timing of ring initiation by determining the accumulation of AHL produced by the colony. Meanwhile,

the spatially dependent gene expression capacity provides the spatial cue to drive pattern formation. Scale invariance requires a proper coordination between the spatial and temporal cues, which are modulated by the domain size and circuit parameters. we now illustrate this notion by examining the key events during the mCherry patterning process, which can be divided into two phases: core formation and ring formation (Figures 3C, 3D, 4B).

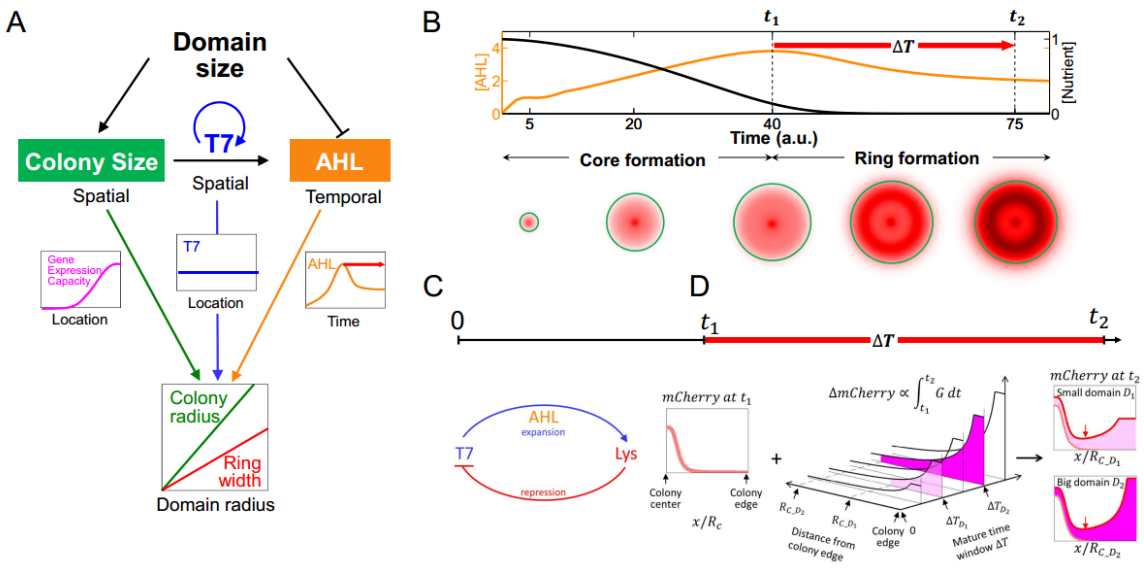

Figure 4: A collective space sensing mechanism underlies scale invariance. A. A collective space sensing mechanism. The domain size controls the pace and extent of colony expansion by determining nutrient availability. The domain size also controls the timing of ring initiation by determining the accumulation rate of AHL. The interplay of the gene expression capacity (magenta curve), T7RNAP profile (blue curve), and AHL concentration (orange curve) leads to the scale invariance of ring width to colony size. The gene expression capacity and T7RNAP profiles are drawn as functions of the distance to the colony center at the final time point. The red arrow indicates the time window for ring maturation. **B. Simulated emergence of a core-ring pattern.** *Top:* AHL (orange curve) and nutrient (black curve) concentrations over time. *Bottom:* Simulated mCherry distributions at different time points. The time points were labeled on x-axis. The mCherry ring initiates when AHL reaches its maximum concentration ($\boldsymbol{t_1}$), which

coincides with a pause of colony expansion ($\boldsymbol{t_2}$). The ring matures during the time window, $\Delta\boldsymbol{T}$, between ring initiation and system stabilization (red arrow). **C. Emergence of scale invariance during core formation.** When the colony is at fast expanding phase, the pattering process is mainly governed by an integral feedback topology which is similar to the expansion-repression model [53]. In our model, the T7RNAP can be considered the expander that drives morphogen (AHL) synthesis, whereas the T7 lysozyme serves as the repressor. At time point $\boldsymbol{t_1}$, the mCherry profile scales with colony radius**. D. Emergence of scale invariance during ring maturation.** All the x-axes are normalized to the domain radius. The units of y-axes are all on a per cell basis. *Left*: At different domain radii, the mCherry profile (pink) at the ring initiation time ($\boldsymbol{t_1}$) approximately scales with domain size. $\boldsymbol{R_C}$ is the colony radius, and it is a function of domain radius. *Middle:* mCherry accumulation during maturation time ($\Delta\boldsymbol{T}$) is mainly determined by the gene expression capacity. The x-axis represents the distance from the colony edge. $\boldsymbol{D_1}$ and $\boldsymbol{D_2}$ are two different domain radii, $\boldsymbol{D_1} < \boldsymbol{D_2}$. $\boldsymbol{R_{C\_D_1}}$ and $\boldsymbol{R_{C\_D_2}}$ are the colony radius for domain radii $\boldsymbol{D_1}$ and $\boldsymbol{D_2}$, respectively. The y-axis is $\Delta\boldsymbol{T}$, the maturation time window. $\Delta\boldsymbol{T_{D_1}}$ and $\Delta\boldsymbol{T_{D_2}}$ are the maturation time windows when the domain radii are $\boldsymbol{D_1}$ (light magenta) and $\boldsymbol{D_2}$ (dark magenta). The intersect of x- and y-axes represent that the mCherry accumulation rate is 0 at the colony edge at ring initiation time, $\boldsymbol{t_1}$. The z-axis indicates the mCherry accumulation during the given time window. *Right:* mCherry at $\boldsymbol{t_2}$ is a combination of that at $\boldsymbol{t_1}$ (pink) and that accumulated during $\Delta\boldsymbol{T}$ (color code is the same with that in middle panel). Its minimum is at the same relative location on the normalized axis (red pointer), indicating proportionality between the inner edge position and the domain radius. The outer edge of the ring pattern is roughly the colony edge, which is also proportional to the domain radius. Combining these two aspects leads to a ring width that scales with the colony size.

At the beginning stage of colony expansion, the T7RNAP positive feedback is active in all cells, leading to global CFP expression. AHL is building up to activate moderate mCherry expression. The gene expression capacity is uniformly high due to the small colony size. Due to the dilution from cell growth at the colony edge, CFP and mCherry are higher in the core at the single cell level. When the colony becomes sufficiently large, such that the colony width is greater than K_φ, it manifests effects of the spatial dependence of the gene expression capacity. This spatial dependence combined

with a strong T7RNAP positive feedback leads to formation of a CFP ring near the colony edge. However, because the expression of mCherry is weaker than that of CFP and insufficient to overcome the dilution due to fast cell growth at the colony edge, there is no mCherry ring formed yet. This phase defines the mCherry core formation. Near the colony edge, the advection of T7RNAP by colony growth and expansion negates effects of the high gene expression capacity, preventing accumulation of T7RNAP or the lysozyme near the edge. The T7 lysozyme profile is thus mainly determined by circuit logic and growth dilution. This phase is reminiscent of the expansion-repression mechanism [49, 53]. In our system, cell growth establishes a gradient by contributing to transport and dilution of a target molecule. The T7RNAP can be considered the expander that drives morphogen (AHL) synthesis, whereas the T7 lysozyme serves as the repressor. As a result of this feedback, the mCherry profile scales with colony radius at the end of first stage (Figure 4C).

As AHL keeps increasing, the metabolic burden and nutrient depletion together slows down colony growth and expansion. Due to the interplay between the T7RNAP positive feedback and the AHL-mediated negative feedback (via lysozyme), T7RNAP has also become approximately uniform across space (Figures 9A-C). Therefore, the spatial dependence of mCherry is primarily determined by the gene expression capacity, which triggers initiation of the mCherry ring near the colony edge. This process is facilitated by the slowdown in overall cell growth. Conversely, the accumulation of

mCherry (and thus the lysozyme) further enhances repression of T7RNAP, which contributes to the down regulation of AHL. Afterwards, the mCherry continues to be expressed across the colony, at rates constrained by the gene expression capacity. The maturation of the mCherry ring is characterized by its widening toward the colony center (Figure 4D).

The collective space-sensing mechanism provides a simple interpretation of the three critical requirements for scale invariance identified by my search algorithm. A *low metabolic burden* by the circuit components ensures that the colony expansion is limited not by the accumulation of a circuit species but rather by nutrient availability, which in turn is limited by the domain size. This coupling allows a perfect coordination between the stop of colony expansion and initiation of the ring at the colony edge.

To generate scale invariance, AHL and T7RNAP both need to be sufficiently uniform across space. The uniform distribution of AHL results from its fast diffusion. The uniform distribution of T7RNAP results from the interplay between the T7RNAP positive feedback and AHL-mediated negative feedback. *Strong T7 positive feedback* is critical for buffering against the varying gene expression capacity, ensuring a flat T7RNAP profile along the domain.

Finally, scale invariance requires a *moderate gene expression capacity gradient*, which has to decrease significantly toward the colony center. If the gene expression did not decrease, mCherry would be uniform across the entire colony. If the gene expression

decreased too sharply, only a narrow mCherry ring would emerge and its width would not scale with the colony width (Figure 8G).

These insights provide an intuitive interpretation for the emergence of scale invariance. When the ring initiates, the mCherry profile scales with the domain size. Thanks to the flat T7RNAP and AHL profiles, maturation of the mCherry ring is driven by gene expression capacity, which has a constant half-width K_φ. When K_φ matches the half-width of the colony wavefront and when the duration of maturation time window scales with the domain size, the change in mCherry during maturation will also scale with the domain size. As a result, the final mCherry profile scales with the domain size (See Chapter 2.4 and Figure 4D, Figures 9D-G for detailed reasoning)

3.2.4 The scale invariance is disrupted by perturbing temporal or spatial cues

Using the base parameter set (Table 2), simulations (Figure 5A) recapitulate the experimentally observed scaling properties (Figures 2C, D), where perfect scale invariance emerged for an intermediate range of domain sizes. According to this mechanism, the pattern formation or scale invariance can be disrupted by perturbing the temporal or spatial cues. When the domain size is too small, the colony size is too small for a distinct ring to emerge. In other words, the ring merges with the core to manifest no distinguishable pattern (Figure 5A, purple region). If the domain size is too large, AHL cannot accumulate to a high enough concentration to trigger ring initiation (Figure

5A, yellow region), again leading to the loss of scale invariance. Both aspects are consistent with experimental data (purple and yellow shaded regions in Figures 2C, D).

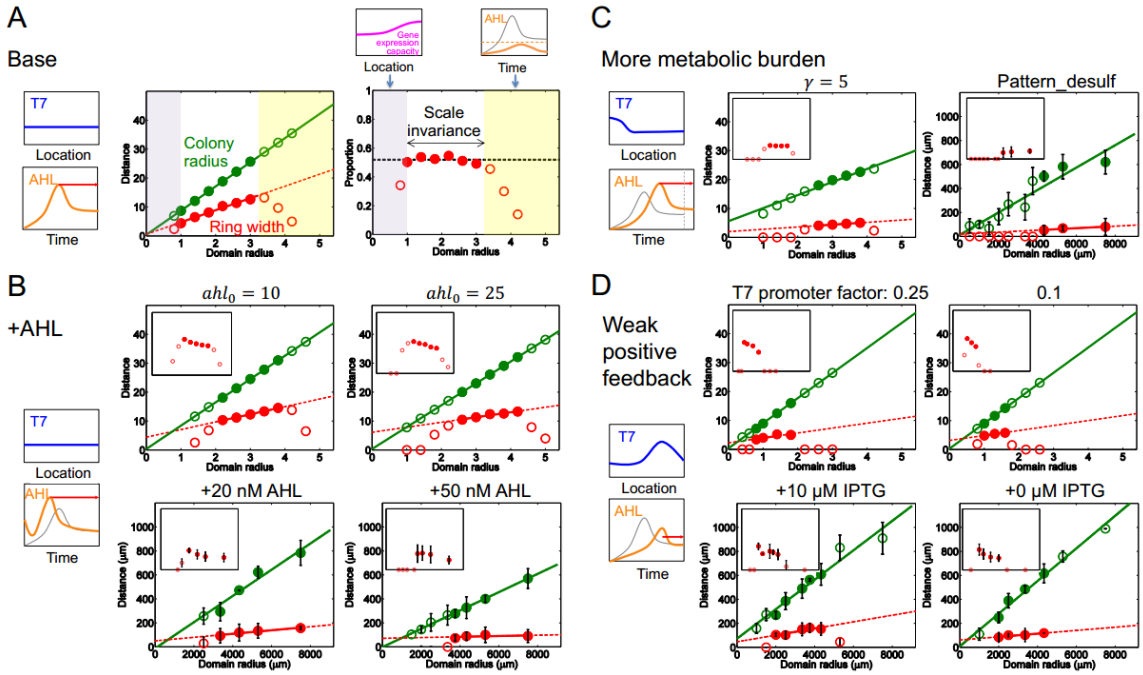

Figure 5: Modulation of scaling property by environmental factors. A. Simulated scale invariance (base case). *Left:* Illustration of T7RNAP and gene expression capacity shape in the scale invariance range. *Middle:* Dependence of the ring width (red circles) and the colony radius (green circles) on the domain radius. The solid lines represent the linear regression of the colony radius and the ring width with respect to the domain radius in the white region. Solid circles represent the linear range of the dependence of the ring width and colony radius on the domain radius. *Right*: The ratio of mCherry ring width to the colony radius for different domain radii. The dashed line shows the average ratio for the values in the white region. *Top left*: Illustration of gene expression capacity profile when the domain is too small (purple shaded regions in Top and Middle panels). *Top right*: Illustration of the AHL profile over time when the domain is too large (yellow shaded regions in Top and Middle panels). The thinner gray curve corresponds to the AHL profile in the left panel; the thicker orange curve corresponds to a larger domain. These results correspond to time point t_2. **B. Modulating the scaling property by adding exogenous AHL.** *Left*: T7RNAP and gene expression capacity profiles were the same with those in base case. Adding exogenous AHL changes the temporal cue. The thinner gray line indicates the AHL concentration over time in the base case; the thicker orange line indicates the AHL concentration over time in the

presence of initial exogenous AHL. The ring maturation window is longer (red arrow) compared with the base case. *Right top:* Simulated scaling property when the parameter of initial exogenous AHL ($\boldsymbol{ahl_0}$) were set to 10 and 25 (from left to right). The two figures show relationships of colony radius and of ring width to domain radius with different initial AHL concentrations. The insets represent the ratio of the ring width to the colony radius. The x-axes for the insets are on the same scale as the corresponding figure panels; the y-axes range from 0 to 1. *Right bottom*: Experimentally measured scaling property in the presence of 20 nM AHL and 50 nM AHL (from left to right). The two figures are plotted as in Figures 1C, D. The error bars represent the standard error or range of 2-5 replicates. Each data point was obtained at 32h after start of experiment. **C. Modulating the scaling property by having a higher metabolic burden.** Cell growth is slowed down at a high metabolic burden, so AHL reaches its peak value later than in the base case. At that time, T7RNAP distribution over space is not flat yet; instead, it has a higher distribution near the center of the colony, which will increase the mCherry core accumulation during the ring maturation stage. Because the maturation time is shorter, the ring cannot catch up with the core formation and the eventual ring width is smaller. The figure symbols are the same as those in Figure 4B. Simulated scaling properties with $\boldsymbol{\gamma}$, the metabolic burden from an effector gene, at a value of 5 ($\boldsymbol{\gamma}$ = 0 for the base case). **D. Modulating the scaling property by using weak T7RNAP positive feedback.** Due to the weak feedback, the T7RNAP distribution over space is no longer flat but instead reflects that of the gene expression profile. The weak feedback also slows down accumulation of AHL, thus delaying the ring initiation in comparison with the base case. Therefore, the ring maturation time (red arrow) is shorter than that in the base case. The figure symbols are the same as those in Figure 4B. The scaling property was simulated with varying positive-feedback strength (the T7 promoter rate is 0.25 or 0.1 fold of promoter rate when circuit is fully induced).

The timing cue can be modulated by adding exogenous AHL, which accelerates ring initiation (Figure 5B, Figure 10E). Our model predicts that the ring width remains a linear function of an intermediate domain size. In comparison with the base case, however, this range of domain sizes conferring the linear dependence is narrower and shifts toward large domain sizes with increasing AHL concentrations. In addition, the linear function has a positive intercept, leading to loss of scale invariance. Both predictions were validated by our observed patterning dynamics in the presence of 10-

50 nM exogenously added AHL. The loss of scale invariance is due to two consequences of exogenous AHL (see Chapter 2.4, Figures 10A-D). First, the maturation time window no longer scales with the domain size, as the ring initiation time is decoupled with the domain size, unlike the base case. Second, the half-width of the colony wavefront becomes wider due to a slight increase in metabolic burden, resulting from accelerated expression of lysozyme and mCherry. This causes a mismatch with the half-width of the gene expression capacity profile. The combination of these effects cause loss of scaling of the mCherry accumulation with respect to the domain size during the maturation phase.

Another key condition for generating scale invariance is the low metabolic burden from gene expression on growth. The metabolic burden controls the pace of cell growth and gene expression. With a higher metabolic burden, the AHL synthesis rate is smaller because of the slower growth rate, so it takes a longer time to reach the peak concentration. This provides a shorter time window for ring maturation (Figure 5C, Figure 10F). Thus, we would expect the ring width to become smaller than the base case. Furthermore, a high metabolic burden cannot maintain a flat T7RNAP profile when the ring initiates. Our model predicts that the combination of these effects would lead to loss of scale invariance. we tested this prediction using an extended circuit containing a cysteine desulfhydrase gene co-expressed with the T7 lysozyme, which caused a greater metabolic burden than did the pattern-formation circuit itself (Figure 8F). When induced, cells carrying the extended circuit indeed exhibited dynamics predicted by

modeling (Figure 5C). Compared with the base case, the ring width became smaller. It remained a linear function of the domain size over a narrower range of domain sizes, and this range shifted toward larger domain sizes. These changes in dynamics led to loss of scale invariance.

The strength of the T7RNAP positive feedback controls both temporal and spatial cues. With a weak positive feedback, the AHL synthesis rate is smaller, and it takes a longer time to reach the peak concentration. This provides a shorter time window for ring maturation (Figure 5D, Figure 11E). Thus, we would expect the ring width to become smaller than the base case. In addition, the model predicts that, in comparison to the base case, the range of the domain sizes that allow pattern formation will shrink and shift toward small domain sizes. Furthermore, a weak positive feedback cannot maintain a flat T7RNAP profile when the ring initiates, as T7RNAP expression itself will be primarily determined by the profile of the gene expression capacity (see Chapter 2.4, Figures 11A-D). Our model predicts that the combination of these effects would lead to loss of scale invariance. Experimentally, the strength of the positive feedback can be controlled by the strength of the promoter driving T7RNAP, which is induced by isopropyl β-D-1-thiogalactopyranoside (IPTG). The T7RNAP feedback weakens when IPTG concentration is low. Under these conditions (100 μM, 10 μM, 1 μM and 0 μM IPTG), the circuit generated a core-ring pattern that was substantially weakened in fluorescent intensity (Figure 8A) compared with that resulting from a

strong positive feedback. The ring width remained a linear function of the domain size over a narrow range of domain sizes. As predicted by modeling, however, this range was narrower and shifted toward smaller domain sizes in comparison with the base case when the IPTG concentration was reduced (Figure 5D).

3.3 Discussions

In comparison with pattern formation, pattern scaling is more challenging to study due to its intrinsically more stringent requirements, in terms of both the underlying regulatory network architecture and the associated reaction mechanisms and parameters. This greater challenge is reflected in the scarcity of well-established, generally applicable mechanisms to explain pattern scaling, in comparison with other aspects of biological patterning [46, 68]. Most mechanisms proposed to explain scale invariance rely on the scaling of morphogen gradients. Our results reveal a collective space sensing mechanism to coordinate colony growth and patterning dynamics to generate scale invariance. Our circuit logic resembles that of the expansion-repression model [53, 69]. However, the dynamic constraints underlying the scale invariance are different from the expansion-repression model. Our mechanism does not require a gradient of the morphogen, but instead relies on the morphogen as a timing cue to trigger pattern initiation.

From a control perspective, our mechanism entails sequential actions of an integral feedback loop and an incoherent feedforward loop (Figure 6). The integral

feedback is implemented through the simultaneous sensing of the domain size using two species, AHL and nutrient. The combined effects of AHL accumulation and nutrient consumption set the timing for the core formation and the ring initiation. As a result, the integral feedback plays a critical role in generating the mCherry distribution at ring initiation time that scales with the colony size.

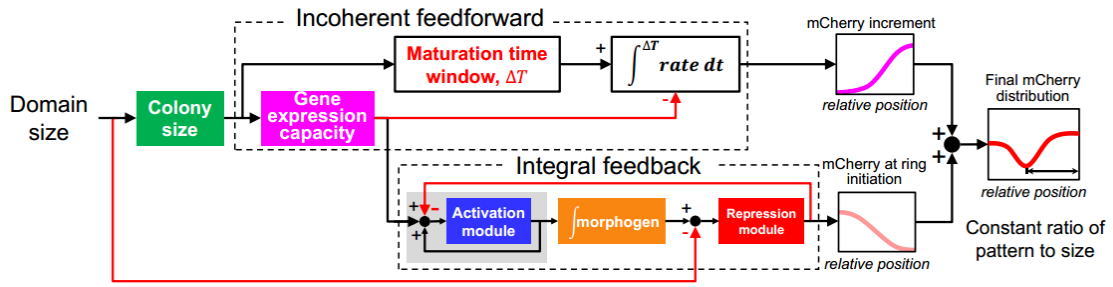

Figure 6: Sequential actions of integral feedback and incoherent feedforward underlie the scale invariance. The overall system input is the domain size; the output is the mCherry pattern in a colony scaled with respect to the domain size. The integral feedback underlies a scale-invariant mCherry distribution at ring initiation. In our system, the activation module represents the strong T7RNAP positive feedback; morphogen represents AHL; the repression module represents T7 lysozyme. The incoherent feedforward controls the mCherry increment during maturation time window of ring formation. $\Delta \boldsymbol{T}$ is a proportional function of domain size; $\boldsymbol{rate}$ represents mCherry accumulation rate, which is dominated by gene expression capacity during ring maturation. At the same *relative* location, a larger domain results in smaller gene expression capacity and thus a reduced accumulation rate in mCherry. This reduction is compensated by the increase in $\Delta \boldsymbol{T}$, leading to the same increment in mCherry at the same relative position for different domain sizes. The sum of the mCherry distribution at ring initiation and the increment during maturation leads to the final mCherry ring (red) that scales with the domain size. The color code is the same as in previous figures.

The incoherent feedforward loop is implemented through the opposing effects of the domain size on two aspects of mCherry accumulation across space. A larger domain size leads to a larger colony, thus reducing the rate of mCherry gene expression at the

same relative position on a scaled axis. However, this reduction is compensated by an extended maturation time, leading to an increment of mCherry that is equivalent at the same relative position within the colony (Figure 4D, 6). The combination of the mCherry profiles at the ring initiation and after ring maturation leads to the final pattern that scales with the colony size. This last step resembles the opposing gradient model [52], which relies on the combination [70] or annihilation [71] of two gradients to generate scaling patterns. However, in our system, the two opposing profiles are not due to molecular diffusion. In addition, the two gradients are sequentially super-imposed.

It is increasingly appreciated that synthetic gene circuits can serve as well-defined model systems to elucidate "design principles" of biological networks [72-74]. The simplicity of the reduced systems enables a high degree of experimental control, which facilitates the deduction of definitive conclusions [75]. Therefore, studies based on synthetic systems can advance the understanding of the underlying mechanisms or processes that are too complicated to study in natural systems [76]. To this end, studies have demonstrated engineering of gene circuits to examine formation of diverse patterns in response to autonomously generated or externally imposed morphogen gradients [29, 77-79]. In contrast, our study focuses on deducing a mechanism underlying the scaling properties of self-organized patterns. Our mechanism underscores the role of temporal control in both generating and scaling patterns.

Geometrically, the patterning process in our system resembles that during the embryonic development in birds and reptiles that occurs in a hard-shell egg. The egg is a self-contained life-supporting system [80], where the shell defines the domain size. Among same species, the vitelline (yolk) weight before embryotic development and hatchling sizes increase isometrically with the egg size [81, 82]. Mechanisms analogous to what we present here could be responsible for generating the scaling property in these systems.

The overall simplicity of our mechanism in terms of the underlying dynamic constraints suggests its applicability to the interpretation of scaling properties of natural biological systems. For example, in the vertebrate neuron tubes, Sonic Hedgehog (Shh) is a morphogen that controls the pattern of neuronal subtype formation [42, 83]. Interestingly, the Shh concentration in the neural tube is found to be much higher than that required to trigger pattern formation [55], and, the duration of Shh plays a critical role in controlling the pattern size [84, 85]. Since cells are known to become insensitive to Shh after prolonged exposure [86], it is conceivable that the duration of elevated Shh concentration may serve as a timing cue to initiate patterning and to time pattern maturation. Also, both the nutrient and AHL are critical in driving pattern formation and scaling in our system. In general, their roles can be fulfilled by other factors controlling tissue growth and gene expression, such as those proposed in the chalone hypothesis [87, 88].

3.4 Supplementary experimental procedures

3.4.1 Strains, media, and device

3.4.1.1 Bacteria strains

Unless noted otherwise, MG1655 cells carrying the circuit or the control plasmids were used for the printing experiments.

3.4.1.2 Circuit and Plasmids

The full circuit consists of two plasmids: pET15bLCFPT7 and pTuLys2CMR2, as described previously[24]

ptetmCherry served as the control for constitutive expression of mCherry. The pattern_LuxIKO circuit is the pattern-formation circuit with *luxI* knocked out [24]. The pattern_curli and pattern_desulf circuits each carries an additional effector gene. The *CsgA* gene [89] was inserted downstream of the T7 lysozyme gene to form the pattern_curli circuit. The cysteine desulfhydrase gene [90] was inserted downstream of T7 lysozyme gene to form the pattern_desulf circuit.

3.4.1.3 Growth media

The LB medium: 25gLB Broth Powder, pH7 (MO BIO Laboratories, Inc) was added into 1L deionized H_2O. After autoclaving for 45mins, the LB medium was stored at room temperature. LB was used to prepare pre-culture for inkjet printing experiments. The medium was supplemented with appropriate antibiotics (75 μg/mL carbenicillin and 50 μg/mL chloramphenicol, or both) when applicable.

The 2×YT medium[91]: 16g tryptone (Difco Laboratories), 5g NaCl (Sigma), 10g yeast extract (Difco Laboratories), and 20.92g MOPS (Sigma) were added into 1L deionized H_2O. The 2xYT medium was adjusted with 1.0M KOH (Sigma) solution to PH = 6.5 by VWR Symphony SB70P PH Meter.

3.4.1.4 Overnight culture

MG1655 cells carrying the full circuit (pET15bLCFPT7 and pTuLys2CMR2) were streaked on an agar plate supplemented with carbenicillin and chloramphenicol, and incubated at 37°C for 16 h. Then, a single colony was picked and inoculated in 3mL LB medium supplemented with 75 μg/mL carbenicillin and 50 μg/mL chloramphenicol for 16 h.

3.4.1.5 Culture well

The culture well used in this system is Culture Well™ multiwell chambered coverslip (Grace Bio-Labs; Bend, OR, USA; Item #103310). Each chip has two 1mm deep wells. The radius of each well is 7500 μm. Before culturing the cells, the rest of the silicon gasket flap was excised using a razor blade.

3.4.2 Methods

3.4.2.1 Measurement of cell density in liquid culture

Cell densities of liquid cultures were quantified using optical density (OD) measured at 600 nm absorbance using a Perkin-Elmer VICTOR3 plate reader.

3.4.2.2 Fluorescent microscopy

A Leica DM16000B fluorescence microscope with a mercury excitation lamp at 5X was used to image samples. Capture resolution was set as 8 bits for depth and 2 for binning. To measure CFP, the excitation filter was set to 436/20, and the emission filter was set to 480/40. The offset of the filter was set to 33/255, gain 100/255. To measure mCherry, the excitation filter was set to 575/25, and the emission filter was set to 632/60. The offset of the filter was set to 0/255; gain 150/255. All these parameters were kept the same between experiments.

3.4.2.3 Inkjet printing

I used the Epson Stylus Photo R280 Ultra Hi-Definition Photo Printer (C11C691201) for printing experiments for three reasons[59]. First, this printer contains a CD tray, which provides the capability of printing on a solid flat surface. After the culture well was loaded on the CD tray, the printing template could be designed to match the corresponding position of the culture well. Second, the inkjet is piezo-activated, which will not affect the cell viability. Third, the printer has a high resolution: 5760 × 1440 pixels at the maximal dots per inch (dpi), which enables precise control of initial seeding positions of bacteria.

To facilitate manipulation and sterilization, the outer shell of the printer was disassembled and removed. I then used PrintPayLess six packs Empty Refillable Ink Cartridges instead of the original ink cartridges.

Print heads were cleaned thoroughly before and after each experiment. First, the printer head box was repositioned to the middle of the printer trail and absorbent paper towels were placed under the printer head to collect the liquid flushing through the printer heads. Second, the printer heads were flushed with 75% ethanol once, followed with washing with deionized water three times gently using a syringe. The absorbent paper towels were removed and the printer head box was then placed back in its original spot.

To prepare 0.3% agar for printing, I mixed 0.15g of agar (214530 Difco™ Agar, Granulated) in 50ml of 2×YT medium, and microwaved the mixture until it was homogenous with no aggregates. I then cooled the agar below 50℃ at room temperature, and supplemented it with 75 μg/mL carbenicillin, 50 μg/mL chloramphenicol, and 1000 μM β-D-1-thiogalactopyranoside (IPTG). I next pipetted 170 μL of the agar into each culture well, and let it solidify at room temperature.

An overnight culture of MG1655 cells carrying the full circuit was diluted to 0.2 absorbance (measured by Victor 3 plate reader) and then diluted another 50 fold into fresh LB broth. The diluted culture was transferred into a tone empty ink cartridge using a sterile syringe. The other five cartridges were filled with deionized water with a 0.2 μm filter (VWR® Syringe Filters, # 28145-477).

Printing templates were designed in software GIMP using 1-pixle diameter spot. Each template was exported to an Epson CD printer program to direct printing of

bacteria onto the agar surface. After printing, a 24 mm×50 mm glass coverslip was placed on the top of the culture well. There are two reasons for using the coverslip: First, the coverslip allows us to control the agar volume. In our typical experiments, the thickness was confined to ~20μm, which allows the cells to grow into a uniform and thin layer. Second, the coverslip seals with the silicon gasket, which minimizes evaporation of water from the soft agar (Figure 7A).

All of the inkjet-printed samples were incubated at 30˚C for 16-43 h.

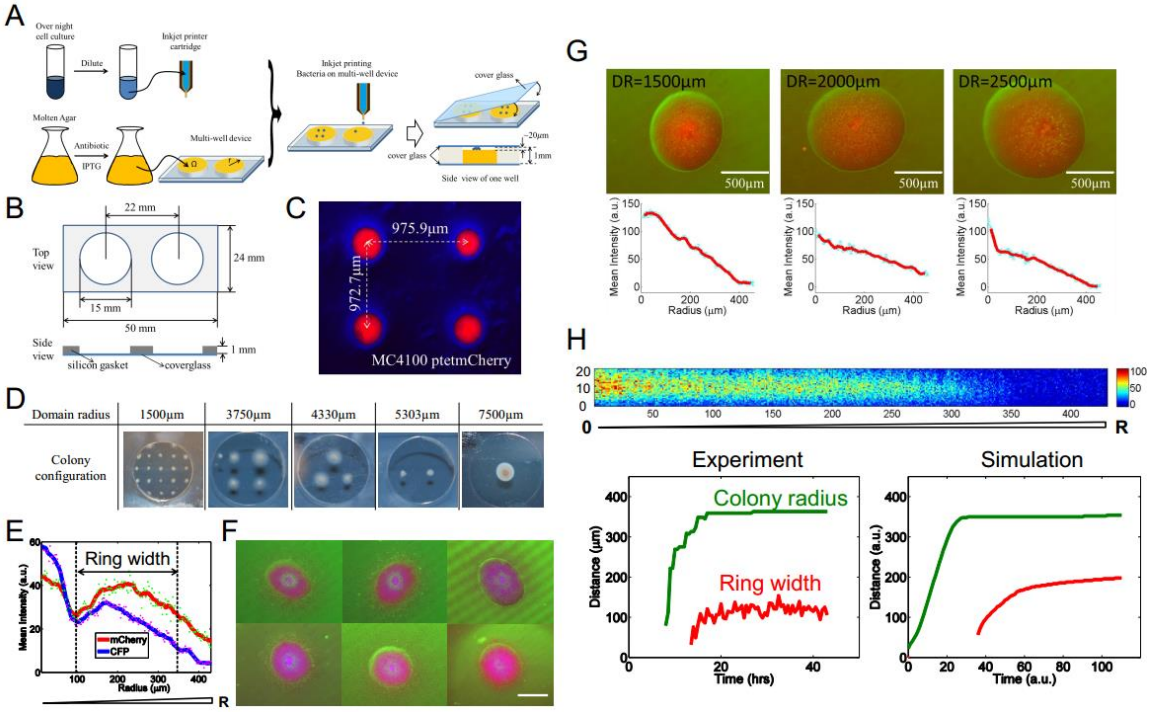

Figure 7: Experiment platform and patterns and growth of inkjet-printed MG1655 cells with or without the gene circuit. A. Protocol for patterning experiments. An LB culture of MG1655 carrying the full gene circuit was grown for 14 h at 37°C. 0.3% molten agar in 2xYT (PH=6.5) medium was prepared. While allowing it to cool, I diluted the overnight culture to an OD of 0.2, and then diluted the resulting culture another 50-fold into 10mL fresh LB culture before loading it into the inkjet printer cartridge. After the agar cooled down to 50˚C, IPTG and appropriate antibiotics were added. 170 μl of

the agar was added to each culture-well. After the agar solidified, I then used the inject printer to print the bacteria (1 pixel size) onto the agar surface using a designed template. A glass coverslip was placed on top of the culture-well after printing. Because of the difference of agar volume and culture-well volume, there was an approximately 20 μm air gap between the agar surface and the top glass cover. B. **A multi-chamber culture-well.** The dimension of the culture-well is illustrated in this graph. For a detailed description, refer to the user manual of the product: Culture Well™ multiwell chambered coverslip (Grace Bio-Labs; Bend, OR, USA; Item #103310). C. **A composite fluorescent microscopy image of inkjet-printed microcolonies.** *Left*: Colonies of MC4100 cells carrying ptetmCherry. The printing template was an array with 1000 μm spacing distance. After 24 h incubation, the distance measured between the center of the colonies were 975.9 μm, and 972.7 μm. *Right*: Mean and standard deviation of measured distance between centers of the colonies with template spacing distance of 500 μm and 1000 μm, respectively. **D. Sample colony arrays corresponding to varying domain radius per colony.** Colonies of MG1655 carrying the full circuit. The domain radius was determined by the configuration of initial printing template. The images were taken after 24 h incubation. For the detailed effective domain radius calculation, see "domain size calculation" in Method section. E. **mCherry (green dots) and CFP (magenta dots) intensity at varying radial distances from the center, quantified from the images in Figure 2B.** The solid red and blue lines represent the running averages of mCherry and CFP intensities, respectively. The black dash lines indicate the inner and outer edges of the mCherry ring. The local minimum of the valley between core and ring determines the inner edge of the ring. The outer edge corresponds to the position on other side of the ring that has the same mCherry intensity as the inner edge. The ring width is the distance between the inner and outer edges. Intensity values were calculated as the average intensity values across all angles at fixed radii about the microcolony core center. In all the images Figure 7E-G, blue represents CFP signal, red represents mCherry signal, green represents phase channel. F. **Replicates of colonies with core-ring patterns.** 1.7 mm × 1.4 mm composite fluorescent (mCherry and CFP) image of MG1655 cells carrying the full circuit. The colonies were from six different experiments. The images were taken after 24 - 32 h incubation at 30°C. G. **Growth and gene expression dynamics of printed MG1655 cells constitutively expressing mCherry.** Top: microscopy images of these cells at domain radii of 1500 μm, 2000 μm, and 2500 μm respectively after 24 h of incubation at 30°C. Bottom: mCherry intensities (green dots) at varying radial distance from the center, quantified from the mCherry images. Each solid red line represents the running averages of mCherry intensities across varying radii. H. **Top: Heat map of fluorescent emission intensity from confocal image of DAPI stained microcolony after 32 h incubation in both vertical (y-axis) and radial directions (x-axis).** The confocal images were taken under the wavelength of 358 nm ultraviolet light. The radial intensity values are the average intensity across angular spanning from 0 to

2π. This process was done by a customized MATLAB code. Bottom: Growth dynamics of the pattern over time. *Left:* Simulated dynamics of mCherry ring width (red) and colony radius (green) over time. The inner/outer ring edge location was measured as described in Figure 7E. The mCherry ring width is the distance between the outer ring edge and the inner ring edge. The colony radius is defined as the distance from the colony center to the edge, where the cell density is half of the maximum density. The configuration is the same as in the left graph.

3.4.2.4 Precise control of seeding configuration by inkjet printing

I tested the inkjet-printing platform by printing MC4100 cells constitutively expressing the mCherry protein. A 3ml LB culture derived from a single colony from MC4100 containing the ptetmCherry plasmid was grown for 16 h at 37℃. The culture was diluted to OD of 0.2 and then diluted another 10-fold before being loaded into an ink cartridge. I placed a 25 mm × 25 mm glass cover in the bottom of the 100 mm petri dish, and then added 7.85 ml molten LB agar supplemented with 50 μg/ml chloramphenicol to generate a 1mm-depth agar layer. After the agar solidified, the embedded glass cover and the above agar were taken out from the petri dish by using a razor blade to cut off the excess agar.

I then printed bacteria onto the agar layer with 1 mm spacing distance between printed spots. The inkjet-printing indeed achieved precise control of the colonies positions. The actual distances between colonies were 969.19 ± 24.28 μm when I intended to print them 1mm apart. The actual distances for the indented 500 μm distances were 506.96 ± 35.57 μm (Figure 7C).

3.4.2.5 Domain size calculation

I made array templates with different spacing distance to control the effective domain area per colony, which is determined as $\frac{agar\ surface\ area}{number\ of\ visible\ colonies}$. The domain radius for each colony is that of a circle with the same area as the effective domain area of the colony. To minimize boundary effects of initial cells printed close to the edge of a culture well, the array was designed to be symmetric and evenly distributed (Figure 7D).

3.4.2.6 Control experiments

I used MG1655 cells carrying ptetmCherry plasmid and the same experimental system described in Figure 7G, by varying the domain radii from 1500 to 2500 μm. In the experiment shown in Figure 8A, after incubation at 30°C for 24 h, no core-ring patterns were observed in the absence of circuit induction by IPTG. Pattern-forming dynamics were evident upon addition of 1mM IPTG (Figures 7G and 8A).

3.4.2.7 Colony radius measurement

In our experiments, the glass coverslip on top of the culture well confines the height of the cell colony. Confocal microscopy images indicate the gap between the agar surface and the top glass cover was ~20μm, consistent with an estimated value of 15μm. Towards the center of the colony, the height is confined by the air gap; the colony height decreases toward to edge because of the motility of the cells.

After locating the center of the colony, distances with greatest gray scale gradient away from the center were recorded. The average value of these distances represents the

colony radius (green line in Figure 7H left panel). The ring width is defined as the distance between the inner and outer edge of the ring (described in Figure 7E).

In simulation, the colony radius (green line in Figure 7H right panel) is defined as the distance from the colony center to the position where the cell density is half of the maximum cell density. The definition of the inner and outer edge of the ring follows the same rules as in Figure 7E.

3.5 Model development

We previously modeled colony growth and gene circuit dynamics using an agent-based approach[24]. The PDE model used in the current study corresponds to the hydrodynamic limit of the stochastic agent-based model from [24]. The PDE formulation has two advantages. First, it is computationally less expensive to solve the PDE model numerically than the stochastic agent-based model. This increased computational efficiency makes intensive parameter estimation studies feasible. Second, the PDE formation better facilitates development of mechanistic insights into the patterning dynamics. Because the air pocket between glass plate and dense agar is only 20μm high (Figure 7H), we model the system in two spatial dimensions and neglect vertical variations in gene expression profiles.

The circuit dynamics can be described by the following PDEs:

$$
\begin{cases}
\dfrac{\partial C}{\partial t} = \kappa_C \Delta C + \alpha_C \dfrac{1}{1+\alpha T+\beta L} \cdot \dfrac{N}{K_N+N} C\left(1-\dfrac{C}{\bar{C}}\right), \\[2ex]
\dfrac{dN}{dt} = -\dfrac{\alpha_N}{|\Omega|}\displaystyle\int_\Omega C\left(1-\dfrac{C}{\bar{C}}\right)\dfrac{N}{K_N+N}\, d\sigma, \\[2ex]
\dfrac{dA}{dt} = \dfrac{\alpha_A}{|\Omega|}\displaystyle\int_\Omega C\, \dfrac{T}{K_T+T}\dfrac{K_P}{K_P+P}\varphi(x,C)d\sigma - d_A A\,, \\[2ex]
\dfrac{\partial T}{\partial t} = \kappa_C \dfrac{\nabla \mathrm{T}\cdot\nabla \mathrm{C}}{C} - \alpha_C T \dfrac{N}{K_N+N}\left(1-\dfrac{C}{\bar{C}}\right) - d_T T \\[2ex]
\qquad\qquad + \alpha_T \theta(C)\dfrac{T}{K_T+T}\dfrac{K_P}{K_P+P}\varphi(x,C) - k_1 TL + k_2 P, \\[2ex]
\dfrac{\partial L}{\partial t} = \kappa_C \dfrac{\nabla \mathrm{L}\cdot\nabla \mathrm{C}}{C} - \alpha_C L \dfrac{N}{K_N+N}\left(1-\dfrac{C}{\bar{C}}\right) \\[2ex]
\qquad\qquad + \alpha_L \theta(C)\dfrac{T}{K_T+T}\dfrac{A^m}{K_A^m+A^m}\varphi(x,C) - d_L L - k_1 TL + k_2 P, \\[2ex]
\dfrac{\partial P}{\partial t} = \kappa_C \dfrac{\nabla \mathrm{P}\cdot\nabla \mathrm{C}}{C} - \alpha_C P \dfrac{N}{K_N+N}\left(1-\dfrac{C}{\bar{C}}\right) + k_1 TL - k_2 P,
\end{cases}
\tag{1}
$$

where

- $C(t,x)$ is the cell density
- $N(t)$ is the nutrient concentration
- $A(t)$ is the AHL concentration
- $T(t,x)$, $L(t,x)$, $P(t,x)$ are cellular T7RNAP, lysozyme and the T7-lysozyme complex density respectively

In deriving these equations, we make the following assumptions:

1. Cells are assumed to perform an unbiased random walk; their movement is modeled as diffusion[92-94]. we considered "diffusion" as an approximation of

the observed colony expansion, so that cell movement can be described by a single lumped parameter. Intracellular components are modeled with passive-tracer equations (see derivation below).

2. Cell growth is modeled with a logistic term, along with a Monod function. The Monod function is to account for contribution of nutrient to overall colony growth. The nutrient here refers to one or more limiting factors that constrain growth. The logistic term accounts for the limit of cell growth in a particular location. This carrying capacity is unlikely limited by nutrient availability. Instead, it is limited by the spatial confinement imposed by our device, which is the colony height is confined to be ~20 μm between the coverslip and the agar surface.
3. Fast diffusion of AHL and nutrient.
4. Gene expression capacity:

$$\varphi(x, C) = \begin{cases} \dfrac{K_\varphi^n}{K_\varphi^n + \left(R_\varphi - x\right)^n}, & x \leq R_\varphi \\ 1, & x > R_\varphi \end{cases} \tag{2}$$

where R_φ is defined as the distance between colony center and the location where cell density is 95% of the carrying capacity (coefficients are all described in Table 1).

Table 1: Definition and the value of parameters used in the PDE model

Parameter	Description	Value	Base Unit	Search range or Reference

κ_C	Cellular diffusion coefficient on 0.3% 2xYT agar	2.5×10^{-3}	$cm^2\cdot h^{-1}$	[95]
α_c	Cell growth rate on 2xYT agar	1	h^{-1}	Fit with experiments
α_n	Nutrient depletion rate	155	$molecule\cdot h^{-1}\cdot cell^{-1}$	Fit with experiments
K_n	Half-saturation for nutrient uptake	20	nM	Fit with experiments
K_A	Concentration threshold of AHL to half-maximum of the pLuxI promoter	20	nM	[96]
α_A	AHL synthesis rate	9600	$molecule\cdot h^{-1}\cdot cell^{-1}$	[97]
d_A	AHL degradation rate	0.3	h^{-1}	[97]
α_L	Synthesis rate of T7 lysozyme	4500	$molecule\cdot h^{-1}\cdot cell^{-1}$	$0 - 9\times10^3$
d_L	Degradation rate of T7 lysozyme	0.0144	h^{-1}	[24]
K_T	Half activation constant of T7RNAP	1200	$molecule\cdot cell^{-1}$	$0 - 5\times10^3$
α_T	Synthesis rate of T7RNAP	6000	$molecule\cdot h^{-1}\cdot cell^{-1}$	$0 - 8\times10^3$
d_T	Degradation rate of T7RNAP	0.3	h^{-1}	[24]
k_1	Combination rate of T-Lys complex	400	$molecule^{-1}h^{-1}\cdot cell$	[98]
k_2	Dissociation rate of T-Lys complex	10800	h^{-1}	[98]
k_D	Equilibrium association constant of T7-lysozyme complex	0.037	$molecule^{-1}\cdot cell$	[98]
K_P	Half inhibition of T-Lys complex	400	$molecule\cdot cell^{-1}$	$0 - 5\times10^3$
α	Inhibition factor of T7RNAP on Growth	1		0 - 5
β	Inhibition factor of T7 lysozyme on Growth	100		$0 - 2\times10^3$

m	Hill coefficient of AHL mediated gene expression	2		[24]
n	Hill coefficient for distance-dependent gene expression capacity	1		0 - 5
K_φ	Half activation distance for gene expression	2	cm	0 - 10
$\bar{C}$	Cell carrying capacity	3×10^5	cells·ml^{-1}	

3.5.1 Derivation of passion tracer equations

T7RNAP, lysozyme and the T7-lysozyme complex cannot diffuse across the membrane of their host cell, and consequently follow the movement of the host cell.

To derive the passive tracer PDE, consider a generic cell-bound substance without sources and sinks, and assume that the cells (C) evolve according to a generic reaction-diffusion equation

$$\frac{\partial C}{\partial t} = \kappa \Delta C + f(C), \tag{3}$$

where κ is the diffusion constant and f is a smooth function. we denote by $Y(t,x)$ (with units $[mol/cell]$) the per cell concentration at location x of the passive tracer, and by $y(t,x)$ (with units $[mol/mm2]$) its surface concentration. Here we invoke again the above assumption on uniform vertical distribution of cell content. In other words, we assume that the per-cell concentration of the substance is uniform in vertical direction and only depends on the location of the cell, but not its height in the stack of cells. Integrating over a control volume V, using the conservation of mass, and applying the divergence theorem, we find the following conservation law in global form

$$\frac{\partial}{\partial t}\int_V Y(x,t)C(x,t)dx = \int_{\partial V} Y(x,t)\,\kappa(x)\nabla C(x,t)\cdot d\sigma$$
$$= \int_V \nabla\cdot\big(\kappa(x)Y(t,x)\nabla C(t,x)\big)dx \tag{4}$$

In the first equality, we used the fact that diffusion is driven along the gradient: the flow is proportional to $\kappa(x)\nabla C$. Together with equation (3), the above conservation equation (4) becomes in local form

$$\frac{\partial Y}{\partial t} = \kappa\frac{\nabla Y\cdot\nabla C}{C} - f(C)Y.$$

3.5.2 Non-dimensionalization of the model

First, we rescale the time and space variables as

$$\hat{t} = \alpha_C t, \quad \hat{x} = \frac{x}{\mathcal{L}}$$

where $\mathcal{L}$ is a length scale to be chosen later.

we next rescale the state variables,

$$\hat{C} = \frac{C}{\bar{C}}, \quad \hat{N} = \frac{N}{N_0}, \quad \hat{A} = \frac{A}{K_A}, \quad \hat{L} = \frac{d_L}{\alpha_L}L, \quad \hat{T} = \frac{d_T}{\alpha_T}T, \quad \hat{P} = \frac{P}{K_P}$$

With these dimensionless variables, and by defining $\hat{\varphi}(\hat{x},\hat{C}) = \varphi(x,C)$, we can rewrite the model equations in a dimensionless form. Introducing the parameter groups G_i, $(i = 1,\dots,12)$ (see Table 2), the nondimensional equations become (omitting the hats for notational simplicity):

$$
\begin{cases}
\dfrac{\partial C}{\partial t} = G_1 \Delta C + \dfrac{1}{1+\alpha T+\beta L} C(1-C)\dfrac{N}{G_2+N}, \\[2ex]
\dfrac{dN}{dt} = -G_3 \displaystyle\int_{\Omega} C(1-C)\dfrac{N}{G_2+N} d\sigma, \\[2ex]
\dfrac{dA}{dt} = G_4 \displaystyle\int_{\Omega} C \dfrac{T}{1+T}\dfrac{1}{1+P} \varphi(x,C) d\sigma - G_5 A, \\[2ex]
\dfrac{\partial L}{\partial t} = G_1 \dfrac{\nabla \mathrm{L} \cdot \nabla \mathrm{C}}{C} - L\dfrac{N}{G_2+N}(1-C) - G_6 L + G_7 \theta(C)\dfrac{T}{1+T}\dfrac{A^m}{1+A^m}\varphi(x,C), \\[2ex]
\dfrac{\partial T}{\partial t} = G_1 \dfrac{\nabla \mathrm{T} \cdot \nabla \mathrm{C}}{C} - T\dfrac{N}{G_2+N}(1-C) - G_8 T + G_9 \theta(C)\dfrac{T}{1+T}\dfrac{1}{1+P}\varphi(x,C), \\[2ex]
\dfrac{\partial P}{\partial t} = G_1 \dfrac{\nabla \mathrm{P} \cdot \nabla \mathrm{C}}{C} - P\dfrac{N}{G_2+N}(1-C),
\end{cases}
\tag{5}
$$

Due to the reversible first order kinetics of T7RNAP bind with T7 lysozyme to form T7-lysozyme complex is fast[98], we add the additional constraint that L, T and P are at equilibrium:

$$P = \frac{G_{10}}{G_{11}G_{12}} TL$$

Table 2: Expression and value of coefficient in nondimensional model

Nondimensional parameter	Expression	Value
G_1	$\dfrac{k_c}{\alpha_c \mathcal{L}^2}$	0.07*
G_2	$\dfrac{K_n}{n_0}$	0.3*
G_3	$\dfrac{\alpha_n \bar{c}}{\alpha_c n_0}\dfrac{\mathcal{L}^3}{\lvert\Omega\rvert}\dfrac{1}{10^{-4}cm}$	0.0046*
G_4	$\dfrac{\alpha_a \bar{c}}{\alpha_c K_a}\dfrac{\mathcal{L}^3}{\lvert\Omega\rvert}\dfrac{1}{10^{-4}cm}$	0.955

G_5	$\frac{d_a}{\alpha_c}$	0.3
G_6	$\frac{d_L}{\alpha_c}$	0.0144
G_7	$\frac{\alpha_L d_L}{\alpha_c \alpha_L}$	0.0144
G_8	$\frac{d_T}{\alpha_c}$	0.3
G_9	$\frac{\alpha_T}{\alpha_c K_T}$	5
G_{10}	$\frac{K_T d_L}{\alpha_L}$	0.0038
G_{11}	$\frac{d_L}{\alpha_L k_D}$	8.64×10^{-5}
G_{12}	$\frac{K_P d_L}{\alpha_L}$	0.0013
$G_{mCherry}$	$\frac{1}{\alpha_c}$	1
G_{CFP}	$\frac{1}{\alpha_c}$	1

* G1, G2, G3 are estimated by comparing the experiment colony expansion with Fisher-KPP's traveling wave solution with wave speed [99]. After fitting G_1 with colony expansion curve, $\mathcal{L} = \sqrt{\frac{k_c}{\alpha_c G_1}}$ =0.18898 cm=1889.8 μm;

3.5.3 mCherry and CFP equations

Experimentally, the circuit dynamics are reported by mCherry and CFP, which are co-expressed with lysozyme and T7RNAP, respectively. To allow for a direct

comparison between model and experiment, we also model the dynamics of mCherry (ψ_R) and CFP (ψ_C):

$$\frac{\partial \psi_R}{\partial t} = G_1 \frac{\nabla \psi_R \cdot \nabla C}{C} - \psi_R \frac{N}{G_2 + N}(1 - C) + G_7 \theta(C) \frac{T}{1 + T} \frac{A^m}{1 + A^m} \varphi(x, C), \tag{6}$$

$$\frac{\partial \psi_C}{\partial t} = G_1 \frac{\nabla \psi_C \cdot \nabla C}{C} - \psi_C \frac{N}{G_2 + N}(1 - C) + G_7 \theta(C) \frac{T}{1 + T} \frac{A^m}{1 + A^m} \varphi(x, C), \tag{7}$$

3.5.4 Domain shape, initial conditions, and boundary conditions

The physical domain (see Figure 7D) is much larger than the emerging patterns, and its total size enters the model equations only through G_3 and G_4, which both scale as $1/|\Omega|$ (see Equation (1) and Table 2). Since the computational domain only provides the computational range for running the simulation, consequently, we choose a computational domain large enough to avoid pattern interference with the boundary and to enforce no-flux boundary conditions.

The initial conditions are chosen to reflect the experimental configuration. Since seeding cells are printed as small droplets on top of the agar, we choose a highly localized, radially symmetric initial field of cells $C(x,t)|_{t=0}$, placed at the center of the domain. The initial nutrient concentration is given by N_0, and the A, L and P concentrations are initially 0. we introduce a small amount of T into the initial cell colony at time 0. Finally, homogenous von Neuman, or no flux conditions are used for all PDEs in system[93].

3.5.5 Numerical solver for the PDE model

To solve the model numerically in MATLAB, we exploit the radial symmetry of the system and reduce it to a PDE in polar coordinates, only depending on one spatial variable, namely the radius $r \in [0, R]$. we then use a fractional multistep method[100, 101]. The goal of the method is to split each equation into the respective advection, diffusion and reaction contributions, and to update each part separately over the basic time step Δt. In addition, we introduce a fourth step, which equilibrates L, T and P after each 3-step update. Next, we briefly describe the numerical methods used in each step.

Step 1: Advection. To update the advection contributions, we combine the MATLAB built-in Runge-Kutta solver ode45 with a second order centered finite difference scheme for discretization of the gradients.

Step 2: Diffusion. Since the diffusion dynamics are stiff, we combine the MATLAB built-in ODE solver ode15s with a second order centered finite difference scheme for discretization of the Laplacian.

Step 3: Reactions. we again use the MATLAB built-in Runge-Kutta solver ode45 to solve the intracellular reaction kinetics.

Step 4: L-T-P equilibration. After completion of steps 1-3, the L-T-P system is updated by projecting it onto the manifold defined by $P = \frac{G_{10}}{G_{11}G_{12}} TL$. With this constraint, the concentrations after steps 1-3 (L_0, T_0, P_0) are updated during step 4 to (L_1, T_1, P_1) as follows:

$$L_1 = \frac{1}{2}\left(L_0 - G_{10}T_0 - G_{11} + \sqrt{(L_0 - G_{10}T_0 - G_{11})^2 + 4G_{11}(L_0 + G_{12}P_0)}\right),$$

$$P_1 = P_0 + \frac{1}{G_{12}}(L_0 - L_1),$$

$$T_1 = T_0 + \frac{1}{G_{10}}(L_0 - L_1).$$

3.5.6 Parameters screening and execution of PDE model

The dimensionless model has 22 parameters (Table 2). Each dimensionless parameter is a combination of several parameters with units. Rather than estimating dimensionless parameters directly, we searched values of dimensional parameters in a realistic range, and then determine the corresponding dimensionless parameters. Ten parameters were estimated or measured in other studies; three parameters were estimated through new experiments (Table 1).

We examined the contributions from the other nine parameters using a simple search algorithm. We first searched 18,231 parameter sets (Figure 8C, light blue lines) to identify those able to generate the core-ring pattern. During this step, we applied three criteria: 1) ability to generate mCherry core-ring pattern similar to the experimental observations; 2) transient CFP dynamics; 3) maintenance of mCherry ring within at least three-fold change in the domain size. Our search yielded 409 parameter sets (Figure 8C, dark blue lines). However, many of these sets did not generate scale invariance (e.g., see Figure 8D, step 1, blue curve).

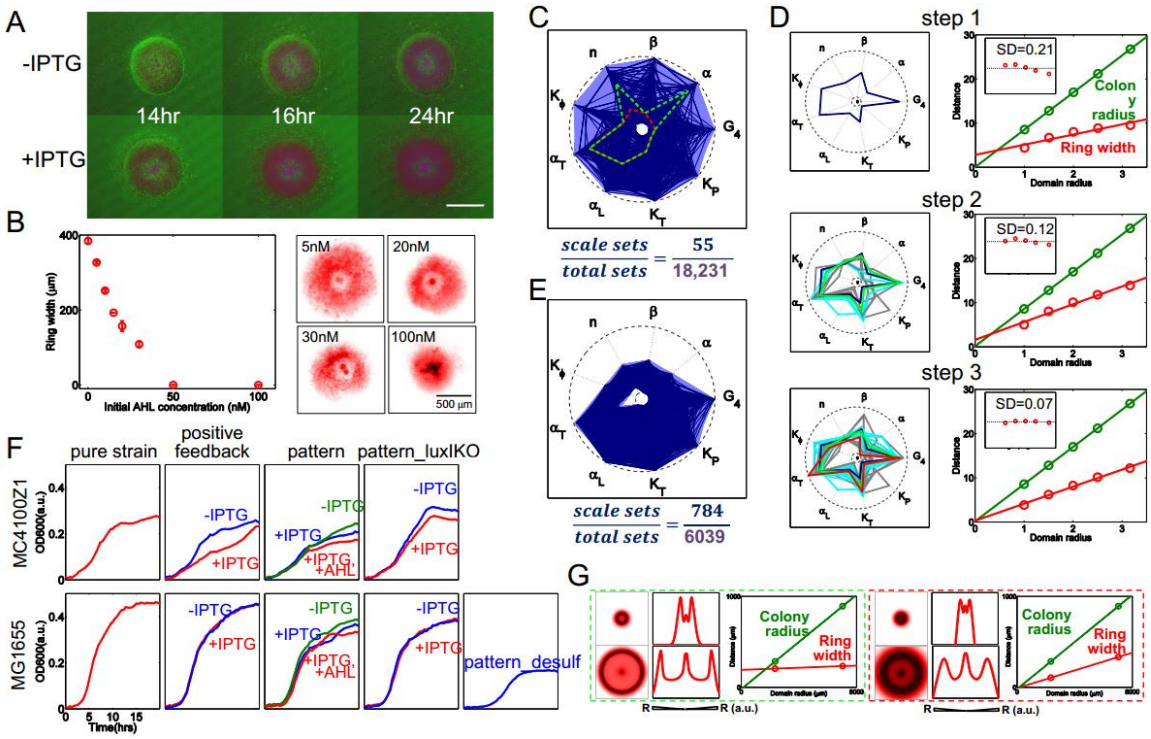

Figure 8: Simulated and measured growth and pattern formation dynamics and constraining model parameters. A. Effects of IPTG induction on pattern formation. Microscopy images of MG1655 cells carrying the full circuit after different incubation time (14 h, 16 h, and 24 h) with and without 1mM IPTG at 30°C. The green channel represents the phase image, the blue channel represents CFP, and the red channel represents mCherry. The scale bar corresponds to 500 μm. The microscope exposure time to mCherry and CFP channels were consistent between two conditions. B. **Measured ring width as a function of the initial AHL concentration**. *Left:* The mCherry ring width decreased with the initial AHL concentration. These values were obtained from replicates after 32 h incubation under corresponding respective domain radii. The error bars represent the standard error (more than 3 replicates per domain radius). *Right:* Representative images of mCherry patterns with different initial AHL concentrations. mCherry images after 32 h incubation for initial AHL concentration of 5 nM, 20 nM, 30 nM, and 100 nM, respectively. C. **Procedure of searching for pattern-forming parameters.** Light blue curves represent 18,231 parameter combinations of $\boldsymbol{G_4, \alpha, \beta, n, K_\emptyset, \alpha_T, \alpha_L, K_T, K_P}$. Dark blue curves represent 409 parameter sets that enhance pattern formation for varying domain radii (from 1 to 3). 55 out of 409 parameters sets could generate scale invariance. In these 409 parameter sets, depending on parameter values, there are two types of patterns. We highlighted two typical sets to make comparison. Green dashed curve: $\boldsymbol{G_4 = 2, \beta = 500, K_\varphi = 2, \alpha_T = 6000, \alpha_L = 4500, K_T =}$

$\mathbf{1200}, \boldsymbol{K_P} = \mathbf{400}$, and $\boldsymbol{\alpha} = \mathbf{4}, \boldsymbol{n} = \mathbf{4}$; and red dashed curve: $\boldsymbol{G_4}, \boldsymbol{\alpha}$, $\boldsymbol{K_\varphi}, \boldsymbol{\alpha_T}, \boldsymbol{\alpha_L}, \boldsymbol{K_T}, \boldsymbol{K_P}$ kept the same value compared to green dashed curve, but $\boldsymbol{\alpha} = \mathbf{0.4}, \boldsymbol{n} = \mathbf{1}$. **D. Optimization of pattern-forming parameters to generate scale invariance.** Step 1. *Left*: using the method described in Figure 2A, we chose one parameter set out of 409 as a starting set (dark blue curve, one parameter set from Figure 8C). *Right*: based on the parameter shown on top, mCherry ring width (red circle) and colony radius (blue circle) as a function of the domain radius. The inset is the ratio of the ring width to the colony radius as a function of the domain radius. The inset image is the ratio of ring with to colony radius as a function of domain radius. The standard deviation of these ratio values is 0.21. Step 2. *Left:* Add a normally distributed perturbation on each value, and repeat 10 times. If the new parameter set does not generate patterns, it is plotted in a gray polygon; otherwise, it is plotted in cyan. The green polygon indicates the parameter set with the highest score. *Right*: Based on the parameter set plotted in green, mCherry ring width (red circle) and colony radius (blue circle) as a function of the domain radius. The standard deviation of these ratio values is 0.12. Step 3. Iterate step 2 for nine more times. The parameter set with highest score (red) is the optimal set. The standard deviation of these ratio values is 0.07. This optimal parameter set generates scale invariance. E. **Procedure of searching for pattern-forming parameters starting from constrained parameter sets.** The searching range for $\boldsymbol{\alpha}$ was swept from 0 to 2.5; $\boldsymbol{\beta}$ from 0 to $\mathbf{1}\times\mathbf{10^3}$; $\boldsymbol{n}$ from 0.5 to 2.5, $\boldsymbol{K_\varphi}$ from 1 to 5; $\boldsymbol{\alpha_T}$ from $\mathbf{2.4}\times\mathbf{10^3}$ to $\mathbf{8}\times\mathbf{10^3}$, other parameter's search range are the same with those in Figure 2A. Light blue closed curves represent 6039 parameter combinations of $\boldsymbol{G_4}, \boldsymbol{\alpha}, \boldsymbol{\beta}, \boldsymbol{n}, \boldsymbol{K_\varphi}, \boldsymbol{\alpha_T}, \boldsymbol{\alpha_L}, \boldsymbol{K_T}, \boldsymbol{K_P}$. Dark blue curves represent 1098 parameter sets that enhance pattern formation for varying domain radii (from 1 to 3). Without further optimizing, there are 784 out of these 1098 parameters sets could generate scale invariance. F. **Growth of MC4100Z1 and MG1655 cells with or without the pattern-forming circuit and its variants.** First panel from left to right: MC4100Z1 cells not carrying a circuit, carrying the positive-feedback module (pET15bLCFPT7) with/without IPTG, carrying the pattern-formation circuit with/without IPTG or AHL, or carrying pattern-formation circuit not containing the luxI gene with/without IPTG. Second panel from left to right: MG1655 cells not carrying a circuit, carrying the positive-feedback module (pET15bLCFPT7) with/without IPTG, carrying the pattern-formation circuit with/without IPTG or AHL, carrying the pattern-formation circuit not containing the *luxI* gene with/without IPTG, or carrying pattern_desulf circuit (blue) with IPTG induction. The y-axis represents optical density of culture under 600nm wavelength excitation, which was measured by a plate reader under 30℃. G. **Two typical patterns.** Green box (no scale invariance): simulation results from the parameter set described by green dashed curve in Figure 8C. The mCherry ring width from these patterns is approximately independent of the domain radius. Red box (scale invariance): simulation results from the parameter set described by red dashed curve in Figure 8C. The mCherry ring width is proportional to the domain radius. In both boxes, the left panels are the

simulated mCherry patterns; the middle panels are the mCherry profiles as function of distance; the right panels describe the dependence of the colony radius and the ring width on the domain radius. In both graphs, the upper panels correspond to a small domain; the lower panels correspond to a large domain.

We next searched the vicinity of each of these sets to determine an optimal set able to generate scale invariance. In each round of search, we introduced a small normally distributed perturbation to each parameter value (Figure 8D, step 2). With the perturbed parameter set, we simulated the patterning dynamics for different domain radii and calculated a score for the parameter set according to its performance in generating scale invariance. This score accounts for two aspects:

(1) The linear correlation between the ring width and the domain radius, as well as that between the colony radius and the domain radius. Each correlation is quantified on the basis of the coefficient of determination (R-squared) to value the linear fit. Higher R-squared value results in a higher score;

(2) The standard deviation (SD) of the ratio of the ring width to the colony radius. Smaller SD value results in a higher score.

We repeated this perturbation 10 times and identified the parameter set with the highest score. We then used this new set as a starting point for the next round of perturbation analysis. The red curve in Figure 8D step 3 is the parameter set that has the highest score after a total of 100 perturbations (10 rounds, each with 10 perturbations to the same parameter set). This parameter set generates a high degree of scale invariance (bottom panel in step 3).

3.5.7 Comparison with previous patterning dynamics

Experimentally, the key differences in the circuit parameters include:

(1) Greater cell motility of MG1655 cells (than MC4100Z1 cells), such that it can still form a sufficiently large colony even when growing on agar with higher density (0.3% in the current study vs. 0.07% in the previous study). This difference is only critical for making our inkjet-printing protocol feasible – it is more challenging to print on very soft agar. In other words, the greater motility of MG1655 compensates for the higher agar density in the current study.

(2) A shallower gradient of the gene expression capacity. This notion is consistent with our observation of the gene expression pattern of constitutive mCherry from MG1655 cells (Figure 7G).

(3) Less metabolic burden of circuit activation on the host cell. To illustrate this point, we measured growth in MC4100Z1 (the cell strain used in the previous study) and MG1655 (current study) cells carrying the pattern-formation circuit and its different variants. These variants include the positive-feedback module, the pattern-formation circuit with the *luxI* gene knocked out, and the pattern-formation circuit with an effector gene co-expressed with the T7 lysozyme. As Figure 8F shows, compared with MG1655 cells, MC4100Z1 cells experienced a higher metabolic burden when different circuits were induced. Furthermore, the

pattern-formation circuits carrying an effector gene (pattern_desulf) caused a higher metabolic burden than did the pattern-formation circuit by itself.

Computationally, the model is able to generate two types of patterns, depending on parameter values. In the presence of a strong metabolic burden by circuit activation (α=4) and fast decaying gene expression capacity (n=4 and $K_\varphi = 2$), the patterns do not exhibit scale invariance (indicated as a green dashed line in Figure 8C). These correspond to our previous experimental data [24]. In this case, mCherry formed a ring during the development, and the ring width did not change with domain radius (Figure 8G, green box). The steep gene expression capacity profile in this configuration results in very high expression of mCherry and T7 lysozyme on the edge relative to the interior. Also, a very narrow ring will occur towards the edge of the colony and since this results in a very high metabolic burden, a pause in colony growth occurs, causing less dilution of circuit components and therefore reinforcement of a very bright, narrow ring.

The other set of parameters have a moderate metabolic burden (α=0.4) and a slowly decaying gene expression capacity profile (n=1) (indicated as a red dashed line in Figure 8C). mCherry here formed a long lasting pattern consisting of a core and a ring, and CFP formed a transient ring before the mCherry ring initiated. Also, both the width of the mCherry ring and the colony radius scaled linearly with respect to the domain radius (Figure 8G, red box). This is consistent with the experimental results generated in the current study. In the current experimental setup, the cells grew on top of the agar,

which provided better access to nutrients for all cells in the colony. Compared with the previous experiment, the gene expression profile in this case exhibited a flatter profile and the metabolic burden caused by circuit activation is weaker.

3.5.8 Emergence of scale invariance

The scale invariance requires a balance between colony growth and timing of pattern formation. In particular, the simulations indicate three conditions that are critical for the generation of scale invariance. First, the metabolic burden by the circuit is small. Second, the T7RNAP feedback is strong. Third, the gene expression capacity declines slowly toward the colony center. Here we illustrate the mathematical basis on how these conditions can lead to scale invariance.

Variables:

- D: domain radius; δ_n: initial nutrient concentration; h: the height of the culture well
- t_1: ring initiation time; t_2: when the nutrient concentration reaches $0.001N_0$(complete exhaustion); $\Delta T = t_2 - t_1$
- R_C: colony radius when the system reaches steady state; σ is the proportion coefficient; $R_C = \sigma \cdot D$
- R_φ(t): the distance from colony center to the position where cell density is 95% of the carrying capacity
- F_W: distance between R_φ and R_C, also defined as half-width of the wavefront

- x_{inner}: distance between the colony center and the inner edge of the ring
- x_{outer}: distance between the colony center and the outer edge of the ring
- W_R: width of the mCherry ring; $W_R = x_{outer} - x_{inner}$.

Proportionality between R_c and D

With a small metabolic burden, the growth dynamics can be decoupled from the circuit dynamics. As a result, the equation governing cell dynamics (1) admits traveling wave solutions:

$$\dot{r} \approx v \frac{N}{G_2 + N} \tag{8}$$

where v is the maximum traveling wave speed.

Next, we notice that nutrient consumption is restricted to the moving colony edge of width $2F_W$. Thus the nutrient consumption is approximated by:

$$\dot{N} = -G_3 2\pi \cdot 2F_W r(t) \frac{N}{G_2 + N} \tag{9}$$

Combining equations (8) and (9) yields:

$$\dot{r} = v \frac{\dot{N}}{-G_3^1 \cdot r(t)}$$

$$\dot{r^2} = -\frac{2v}{G_3^1} \dot{N}, \tag{10}$$

where $G_3^1 = 4\pi F_W G_3$.

Integrating both sides of equation (10) yields:

$$r(t) = \sqrt{\frac{2v}{G_3^1}(N(0) - N(t))}$$

Eventually, all nutrient will be consumed, and hence:

$$R_c = \lim_{t\to\infty} r(t) = \sqrt{\frac{2v}{G_3^1}N(0)} = \sqrt{\frac{2v}{G_3^1}\pi D^2 h\delta_n} = \sqrt{\frac{2v}{G_3^1}\pi h\delta_n}\cdot D.$$

Or:

$$R_c = \sigma D,$$

where $\sigma = \sqrt{\frac{2v}{G_3^1}\pi h\delta_n}$, a constant.

Proportionality between t_1 and D

To simplify the estimation, we rewrite equation (5) as follows:

$$\begin{cases} \frac{da}{dt} = \alpha_A \frac{T}{K_T + T}\frac{K_P}{K_P + P}, \\ \frac{\partial T}{\partial t} = \alpha_T \frac{T}{K_T + T}\frac{K_P}{K_P + P} - \frac{\partial P}{\partial t}, \\ \frac{\partial L}{\partial t} = \alpha_L \frac{T}{K_T + T}\frac{A^m}{K_A^m + A^m} - \frac{\partial P}{\partial t}, \\ \frac{\partial P}{\partial t} = k_1 TL - k_2 P, \\ A = \frac{1}{|\Omega|}\sum a \end{cases}$$

Here we make several assumptions:

(1) a is AHL production per cell. This is a function of time and location.

(2) Gene expression only takes place over a certain width along the edge of the colony. This assumption is made with reference the gene expression capacity formula, in which half width is applied as a constant.

(3) Because the metabolic burden is low, we separate colony growth from the gene expression equations.

It can be shown that, when $A \gg 1, P(x,t) \approx a(x,t)$. The relation between t_1 and D is determined by how quickly AHL accumulates and the amount of this accumulation.

AHL accumulation rate

The rate of AHL accumulation over time is given by:

$$\frac{dA}{dt} = G_4 \int_{\Omega} C \frac{T}{1+T} \frac{1}{1+P} \varphi(x,C) d\sigma - G_5 A ,$$

At the beginning of cell growth, $C \frac{T}{1+T} \frac{1}{1+P}$ is the same for different domain sizes. Near time 0, A is negligible; thus, the degradation term can be eliminated. Therefore,

$$\frac{dA}{dt} \propto G_4 \propto \frac{1}{|\Omega|} \propto \frac{1}{D^2}$$

AHL accumulation amount

The total amount of AHL accumulation is also determined by the same rate equation but can be approximated by considering the time window when AHL approaches its maximum (or when time approaches t_1)

$$\frac{dA}{dt} = G_4 \int_{\Omega} C \frac{T}{1+T} \frac{1}{1+P} \varphi(x,C) d\sigma - G_5 A = G_4 \frac{T}{1+T} \frac{1}{1+P} * 2\pi R_C * K_\varphi - G_5 A$$

As AHL approaches its maximum, we have $A \gg 1,\ T(x,t) \ll 1$. Also, $T(x,t)$ does not change significantly over time due to the lysozyme-mediated negative feedback; thus, $\frac{T}{1+T} \approx small\ constant$. Under this condition, we also have $P \approx a$. Hence:

$$\frac{dA}{dt} \propto \frac{R}{D^2} \frac{1}{1+P} - G_5 A = \frac{R}{D^2} \frac{1}{1+a} - G_5 A = \frac{R}{D^2} \frac{1}{1 + \frac{A * D^2}{R_C}} - G_5 A$$

When AHL reaches its maximum (A_{max}), we have $\frac{dA}{dt}|_{A=A_{max}} = 0$, or:

$$\frac{R_C}{D^2}\frac{1}{1+\frac{A_{max}*D^2}{R}} - G_5 A_{max} = 0 \rightarrow {A_{max}}^2 D^2 + R_C A_{max} = \frac{{R_C}^2}{D^2 \cdot G_5}$$

Because $R_C \propto D, {A_{max}}^2 D^2 + R_C A_{max} \propto 1 \rightarrow A_{max}|_{t=t_1} \propto \frac{1}{D}$. Therefore,

$$t_1 = \frac{A_{max}|_{t=t_1}}{AHL\ acucmulation\ rate} \propto \frac{\frac{1}{D}}{\frac{1}{D^2}} \propto D$$

Proportionality of the mCherry ring width to D

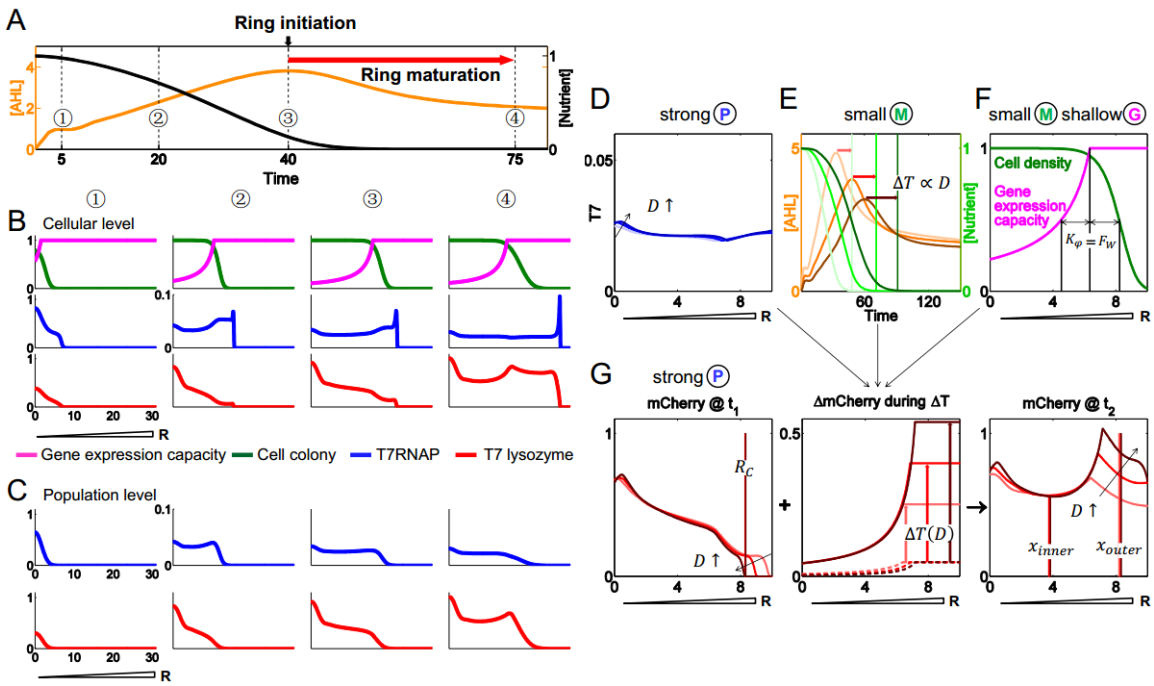

Figure 9: Simulated spatial and temporal dynamics of circuit components underlying the core-ring pattern formation and scale invariance. A. AHL and nutrient concentrations over time. Four dashed lines indicate four time points 5, 20, 40, 75 (artificial units). B. **Profiles of key factors (spatial-dependent gene expression capacity, cell density, T7RNAP and lysozyme distribution) at the cellular level as a function of the radial distance from the center of colony at each phase.** (1): CFP and mCherry core formation. Since AHL diffuses across the whole domain, its concentration is low initially and inhibition of T7 RNAP via AHL-activated T7 lysozyme is negligible. The gene expression capacity is uniformly high in the small colony. Therefore, CFP and mCherry distributions are mainly determined by the cell density distribution. (2): CFP ring

formation. With the colony expanding, gene expression capacity begins to have significant effect. At the edge of the colony, high global gene expression capacity leads to high T7RNAP expression, giving rise to the formation of CFP ring. Though AHL accumulates to a high level, high T7RNAP concentration and high gene expression capacity at the edge of the colony leads to an increase in the mCherry synthesis rate, but not yet a mCherry ring. (3): mCherry ring initiation. With nutrient depletion, the colony stops expanding. The combination of high AHL concentration, T7RNAP, and gene expression capacity leads to the initiation of a mCherry ring. (4): mCherry ring maturation. The AHL concentration decreases, but still stays over the threshold. Because cell diffusion begins to have a larger impact than colony driving force, the gene expression capacity leads to the maturation of mCherry ring. C. **Profiles of T7RNAP and lysozyme distribution at the population level** as a function of radial distance from the center of colony at each phase. By population level, we mean the total T7RNAP (or lysozyme) from all the cells at a specific location. D. **T7RNAP profiles at the ring initiation time (t_1) on a normalized axis for varying domain radii** (1.4 and 3). The x-axis is at relative length, scaled by the domain radius. The notation on top of the figure means strong positive feedback is the main reason for generating this flat T7RNAP profile. For all the images in Figures S3-5, if unnoted, lighter color means data generated in smaller domain. E. A**HL and nutrient concentrations over time for different domain radii.** The light to dark orange curves represent AHL concentrations for an increasing domain radius; the gray to black curves represent nutrient concentrations for an increasing domain radius. The peak of the AHL curve defines the ring initiation time, $\boldsymbol{t_1}$. Three straight solid green lines represent the nutrient depletion time, $\boldsymbol{t_2}$. The red arrows represent the ring maturation time $\Delta\boldsymbol{T}$ for each domain radius. $\Delta\boldsymbol{T}$ is proportional to domain radius *D*. F. **Cell density and gene expression capacity profiles along the normalized axis, for a domain radius of 3.** The half threshold of gene expression $\boldsymbol{K_\varphi}$ equals the half-width of cell distribution's wavefront ($\boldsymbol{F_W}$). **G. Maturation of the mCherry ring from $\boldsymbol{t_1}$ to $\boldsymbol{t_2}$.** All three panels are on a normalized x-axis. The units of y-axes are all in per cell base. **mCherry @ $\boldsymbol{t_1}$**: The initial mCherry profiles (red curves) for different domain radii approximately overlap, indicating scale invariance. **ΔmCherry during $\Delta\boldsymbol{T}$**: the accumulation of mCherry is mainly determined by the gene expression capacity. At a larger domain radius, the profile of gene expression capacity is sharper compared to that at a smaller domain (dashed lines). However, the ring maturation time for a larger domain is longer (red arrow), so the total accumulation of mCherry (solid curves) at the same relative location is equivalent for different domains. That is, ΔmCherry is approximately scale invariant. **mCherry @ $\boldsymbol{t_2}$**: After adding the accumulation profile on the mCherry profile at $\boldsymbol{t_1}$, the minimum point of the mCherry profile at steady state (red curve) is at the same relative location. Since the outer edge of the ring pattern is roughly the colony edge, this min point defines the inner ring edge.

The inner edge of the mCherry ring is not scale invariant. Domain radius varies from 1.4 to 3.

After t_1, colony radius expansion is negligible. According to (6), advection of mCherry and T7RNAP within R_c is negligible as $\nabla C \approx 0$. The profile of mCherry $\psi_R(x,t)$ at radius x and time t can be expressed as

$$\psi_R(x,t) = \psi_R(x,t_1) + G_7 \int_{t_1}^{t} \varphi(x,t) \cdot \frac{T(x,t)}{1+T(x,t)} \cdot \frac{A(t)^m}{A(t)^m+1} dt$$

Therefore, when $t = t_2$, mCherry profile is

$$\psi_R(x,t_2) = \psi_R(x,t_1) + G_7 \int_{t_1}^{t_2} \varphi(x,t) \cdot \frac{T(x,t)}{1+T(x,t)} \cdot \frac{A(t)^m}{A(t)^m+1} dt \tag{11}$$

Conditions required for scale invariance (as revealed by numerical simulations):

- **A strong T7 positive feedback**, coupled with negative feedback from lysozyme, leads to a flat T7RNAP profile across space after t_1. Also because of the negative feedback, $T(x,t) \ll 1$ and does not change significantly over time (Figure 9D). That is,

$$\frac{T(x,\ t)}{1+T(x,t)}\Big|_{t_1 \le t \le t_2} \approx T(x,t) \approx \tau \tag{12}$$

- Between t_1 and t_2, AHL remains $\gg 1$ (Figure 9E). Since the AHL concentration is not space dependent,

$$\frac{A(t)^m}{A(t)^m+1}\Big|_{t_1 \le t \le t_2, m=2} \approx 1 \tag{13}$$

- Given equations (12) and (13), the accumulation of mCherry is mainly determined by the gene expression capacity (equation (2)), a space and time

dependent function. Simulations indicate that scale invariance is favored when $n \approx 1$; that is, the **gene expression capacity profile is shallow**. After the ring initiates at t_1, colony expansion is negligible compared to the final cell radius, R_C. Therefore, $r(t)|_{t_1 \le t \le t_2} \approx R_C \approx \sigma \cdot D$.

Since $R_\varphi(t)$ is defined as the position where cell density is 95% of the carrying capacity, $R_\varphi(t)$ is a function of R_C. Based on the search results: $K_\varphi = F_W(t_1) \Rightarrow K_\varphi + R_\varphi(t)|_{t_1 \le t \le t_2} = R_C = \sigma \cdot D$ (Figure 9F). Hence:

$$\varphi(x,t)|_{t_1 \le t \le t_2} = \frac{K_\varphi}{K_\varphi + R_\varphi(t) - x} = \frac{K_\varphi}{\sigma \cdot D - x}$$

Therefore,

$$\psi_R(x,t_2) = \psi_R(x,t_1) + G_7 \tau \int_{t_1}^{t_2} \frac{K_\varphi}{\sigma \cdot D - x} dt$$

$$= \psi_R(x,t_1) + \frac{G_7 \tau \Delta T K_\varphi}{\sigma \cdot D - x}$$

However, the match between K_φ and the half-width of the colony wavefront is not an absolute constraint. The system can still generate approximate scale invariance even when these two variables are slightly different.

Calculating the mCherry ring width (Figure 3C, S3G):

The ring width refers to the distance between the valley of mCherry profile to its horizontal intersection at t_2. To compute the ring width, we examine the mCherry profile in two steps: mCherry profile at t_1 and the accumulation of mCherry from t_1 to t_2 (the maturation phase).

Based on simulations, the mCherry profile at ring initiation time, $\psi_R(x, t_1)$, scales with the domain radius D. This scaling results from the initial phase of the circuit dynamics coupled with colony growth and expansion. A strong T7RNAP positive feedback loop induces fast lysozyme synthesis. Meanwhile, a small metabolic burden decouples cell growth from the circuit dynamics. The fast dilution from the cell growth gives the cell in the relative same location of the colony same amount of time to synthesizes mCherry. Given this scaling, we use a normalized distance, $\hat{x} = \frac{x}{D}$ to continue the calculation.

$$\psi_R(\hat{x}, t_2) = \psi_R(\hat{x}, t_1) + \frac{G_7 \tau \Delta T K_\varphi}{\sigma \cdot D - \hat{x} \cdot D} \tag{14}$$

Due to the scaling of mCherry profile at t_1, $\psi_R(\hat{x}, t_1)$ is approximately the same for varying domain sizes on normalized axis (Figure 9G, left).

The time for nutrient exhaustion, t_2, is proportional to the initial nutrient concentration, which is proportional to D. The time for ring initiation, t_1, is the time when AHL reaches a maximum. This time is also proportional to D according to our simulation. Thus, $\Delta T = t_2 - t_1 = \delta \cdot D$ (δ is a positive constant).

$$\frac{G_7 \tau \Delta T K_\varphi}{\sigma \cdot D - \hat{x} \cdot D} = \frac{G_7 \tau \delta K_\varphi}{\sigma - \hat{x}}$$

Therefore, the accumulation of mCherry during the maturation process $\frac{G_7 \tau \delta K_\varphi}{\sigma - \hat{x}}$ is independent of D (Figure 9G, middle), when using the normalized x-axis.

Taken together, the mCherry profile on a normalized axis at t_2 is:

$$\psi_R(\hat{x}, t_2) = \psi_R(\hat{x}, t_1) + \frac{G_7 \tau \delta K_\varphi}{\sigma - \hat{x}}$$

Again, both $\psi_R(\hat{x}, t_1)$ and $\frac{G_7 \tau \delta K_\varphi}{\sigma - \hat{x}}$ are independent of D. If there is an inner edge $\hat{x}_{inner}$, it will be the **same value** for varying domain radius (Figure 9G, right). That is, $x_{inner} = D \cdot \hat{x}_{inner} \propto D$; the position of the inner edge always scales with D. x_{outer} is approximately equal to $R_C \approx \sigma \cdot D \propto D$. Therefore, ring width $W_r = x_{outer} - x_{inner} \propto D$.

3.5.9 Effects of adding exogenous AHL

Both simulation using the full model and experiments demonstrate that addition of exogenous AHL has two major effects (Figure 4B):

(1) Formation of smaller rings.

(2) Disruption of the proportionality between the ring width and domain radius, while maintaining their linear correlation for a smaller range of domain radii.

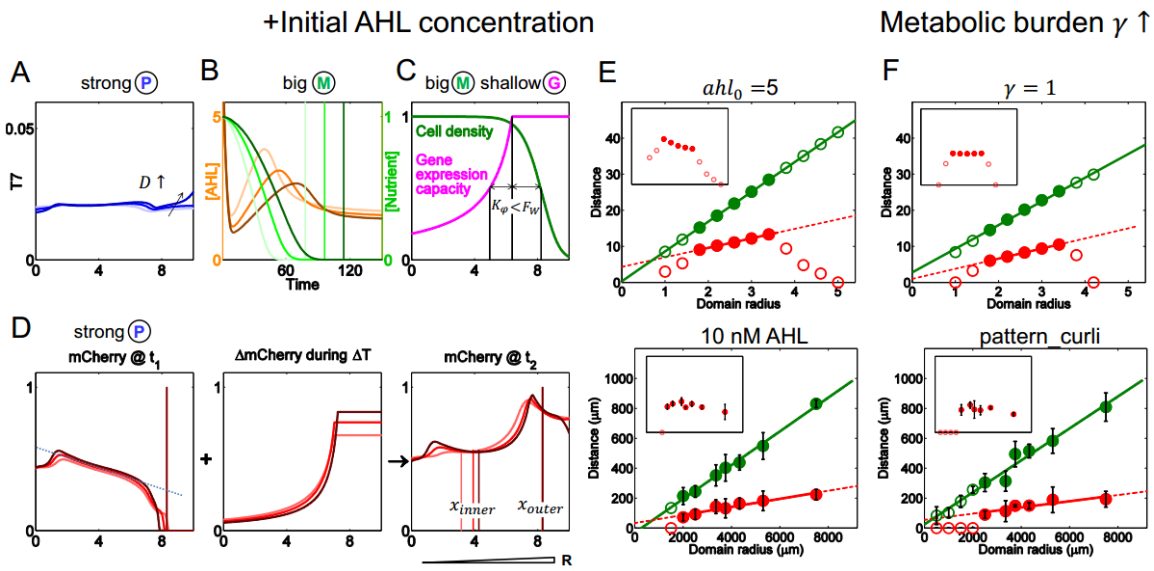

Figure 10: Scaling property of patterns in the presence of exogenous AHL or a higher metabolic burden. A. T7RNAP profiles at the ring initiation time (t_1) on a normalized axis for varying domain radii (2.2 and 3.8). The x-axis is at relative length, scaled by the domain radius. The notation on top of the panel indicates that strong positive feedback is the cause of flat T7RNAP profile. **B. AHL and nutrient concentrations over time for different domain radii.** The AHL concentration starts from the same initial value for different domain at time 0. The ring maturation time ΔT for each domain radius is not proportional to domain radius D in this case. **C. Cell density and gene expression capacity profiles along the normalized axis, for a domain radius of 3.** K_φ is smaller than F_W. **D. Maturation of the mCherry ring from t_1 to t_2. mCherry @ t_1:** The initial mCherry profiles (red curves) for different domain radii approximately overlap, with the middle part of the curve overlaps into a linear line. **ΔmCherry during ΔT:** Since ΔT is not proportional to D, and $K_\varphi < F_W$, ΔmCherry in this case is not scale invariant. **mCherry @ t_2**: After adding the accumulation profile on the mCherry profile at t_1, the minimum point of the mCherry profile at steady state (red curve) is at the same relative location. The inner edge of the mCherry ring is not scale invariant. Domain radius varies from 2.2 to 3.8. **E. Modulating the scaling property by adding exogenous AHL.** Top: Simulated scaling property when the parameter of initial exogenous AHL (ahl_0) was set to 5. The figure symbols are the same as those in Figure 4B. Bottom: Measured scaling property in the presence of 10 nM AHL. The error bars represent the standard error or range of 2-4 replicates. Each data point was obtained at 32h after start of experiment. The insets represent the ratio of the ring width to the colony radius. The x-axes for the insets are on the same scale as the corresponding figure panels; the y-axes range from 0 to 1. **F. Modulating the scaling property by having a higher metabolic**

burden. Top: Simulated scaling property with metabolic burden from effector gene $\boldsymbol{\gamma}$ equal to 1 ($\boldsymbol{\gamma}$ value base case is 0). The figure symbols are the same as those in Figure 4C. Bottom: Measured scaling property in MG1655 carrying pattern_curli. Pattern curli induced a higher metabolic burden than the pattern-formation circuit. However, it induced a less burden than the pattern_desulf circuit. The insets represent the ratio of the ring width to the colony radius. The x-axes for the insets are on the same scale as the corresponding figure panels; the y-axes range from 0 to 1.

These effects can also be intuitively interpreted based on the same mathematical framework outlined above. Compared with the base case, equations (12) and (13) still hold in the presence of exogenous AHL. However, the extra AHL induces more lysozyme expression, which induces higher metabolic burden on cell growth (Figure 10C). Compared to cell growth, diffusion will be the dominant factor to determine local cell density, which leaves the half-width of wavefront wider than in the base case.

$$K_\varphi + \varepsilon = F_W(t_1), \qquad (\varepsilon > 0)$$

$$\Rightarrow K_\varphi + R_\varphi(t)|_{t_1 \le t \le t_2} = R_C - \varepsilon = \sigma \cdot D - \varepsilon$$

Equation (11) becomes:

$$\psi_R(\hat{x}, t_2) = \psi_R(\hat{x}, t_1) + \frac{G_7 \tau \Delta T K_\varphi}{\sigma \cdot D - \varepsilon - \hat{x} \cdot D} \tag{15}$$

Based on simulation, the maturation time is still proportional to D: $\Delta T = t_2 - t_1 = \delta_{ahl} \cdot D$. However, $\delta_{ahl} > \delta$ as the ring initiates earlier (t_1 is smaller than the base case).

$$\psi_R(\hat{x}, t_2) = \psi_R(\hat{x}, t_1) + \frac{G_7 \tau \delta_{ahl} K_\varphi}{\sigma - \frac{\varepsilon}{D} - \hat{x}}$$

To understand why the relationship of ring width to domain radius has a positive intercept on y-axis, the position of the ring's inner edge needs to be calculated.

In Figure 10D (left), from unit 2 to unit 7 on x-axis, the mCherry profile is approximately linear: $y = -k\hat{x} + a_0$, (k, a_0 are positive constants).

The inner edge position, x_{inner}^{+ahl}, satisfies $\frac{\partial \psi_R(\hat{x},t_2)}{\partial \hat{x}}|_{\hat{x}=\widehat{x_{inner}^{+ahl}}} = 0$. Therefore, we have:

$$\frac{\partial \psi_R(\hat{x},t_1)}{\partial x} + \frac{G_7 \tau \delta_{ahl} K_\varphi}{\left(\sigma - \frac{\varepsilon}{D} - \hat{x}\right)^2} = 0$$

$$\widehat{x_{inner}^{+ahl}} = \sigma - \frac{\varepsilon}{D} - \sqrt{\frac{G_7 \tau \delta_{ahl} K_\varphi}{k}}$$

Eventually,

$$W_R = \left(\widehat{x_{outer}^{+ahl}} - \widehat{x_{inner}^{+ahl}}\right) D$$

$$= \sigma D - \left(\sigma - \frac{\varepsilon}{D} - \sqrt{\frac{G_7 \tau \delta_{ahl} K_\varphi}{k}}\right) D$$

$$= \varepsilon + \sqrt{\frac{G_7 \tau \delta_{ahl} K_\varphi}{k}} D$$

That is, the ring width is a linear function of the domain radius but with a positive intercept.

3.5.10 Effect of higher metabolic burden

According to our simulation using the full model and experiment, having significant additional metabolic burden (e.g. by expressing another gene) would lead to the loss of scale invariance (Figure 4C).

Conditions:

- Compared with the base case, the AHL concentration accumulates slowly to pass the half activation threshold (=1). After t_1, AHL decreases but remains $\gg 1$. As with the base case, the AHL concentration is not space-dependent due to its fast diffusion.
- With a higher metabolic burden, the colony growth slows down substantially. The T7RNAP profile is no longer flat across space after ring initiation at t_1. Instead, it will have a higher distribution around colony center.
- Different from the base case, a higher metabolic burden has a significant effect on cell growth. Cell diffusion is the dominant factor to determine local cell density, which leaves the half-width of the wavefront wider than in the base case. Under this condition, the relationship of K_φ and $R_\varphi(t)$ is similar to the case of adding exogenous AHL (Figure 10F). Hence,

$$\psi_R(x,t_2) = \psi_R(x,t_1) + G_7\tau \int_{t_1}^{t_2} \frac{T7(x,\ t)}{1+T7(x,t)} \cdot \frac{K_\varphi}{\sigma \cdot D - \varepsilon_2 - x} dt$$

Here, the inner edge cannot be expressed as a simple mathematical function. Due to a smaller synthesis rate of AHL, ΔT is shorter. **The smaller ΔT, together with the perturbed T7RNAP distribution, will lead to a ring width with a smaller width.** Because of the additional metabolic burden, colony radius does not rely solely on nutrient availability (Figure 4C).

3.5.11 Effects of reducing the positive feedback strength

According to our simulation using the full model and experiment, a significant reduction in the strength of the T7RNAP positive feedback would lead to loss of scale invariance (Figure 4D). However, a linear dependence between the two is maintained within a smaller range of domain radius, in comparison with the base case.

Conditions:

- Compared with the base case, the AHL concentration accumulates slowly to pass the half activation threshold (=1). After t_1, AHL decreases but remains $\gg 1$. As with the base case, AHL concentration is not space dependent.
- With a weak positive feedback, the T7RNAP profile is no longer flat across space after ring initiation, t_1 (Figure 11A). Instead, it is dictated by the gene expression capacity and the T7RNAP level is greater near the colony edge.
- Similar to the base case, circuit activation does not cause a significant metabolic burden; thus $K_\varphi + R_\varphi(t)|_{t_1 \le t \le t_2} = R_C = \sigma \cdot D$. (Figure 11C). Hence

$$\psi_R(x, t_2) = \psi_R(x, t_1) + G_7 \tau \int_{t_1}^{t_2} \frac{T7(x,\ t)}{1 + T7(x, t)} \cdot \frac{K_\varphi}{\sigma \cdot D - x} dt$$

Here, the mCherry profile at t_1 no longer scales with the domain radius as mCherry accumulation is affected by the T7RNAP spatial distribution. The inner edge cannot be expressed in a simple mathematical function. However, qualitative analysis of the process can give us the insights of most features.

Due to a smaller synthesis rate of AHL with a weak T7RNAP positive feedback loop, ΔT is shorter. The shorter ΔT leads to a shorter maturation time for the ring, thus a smaller **ring width**. In the base case, ΔT increases proportionally with the domain size. However, when positive feedback is too weak, ΔT decreases with the domain size (Figure 11B). When the domain size is too large, there is not enough time to initiate the ring. **The linear regime of ring width vs. domain radius shrinks and shifts to small domain sizes.**

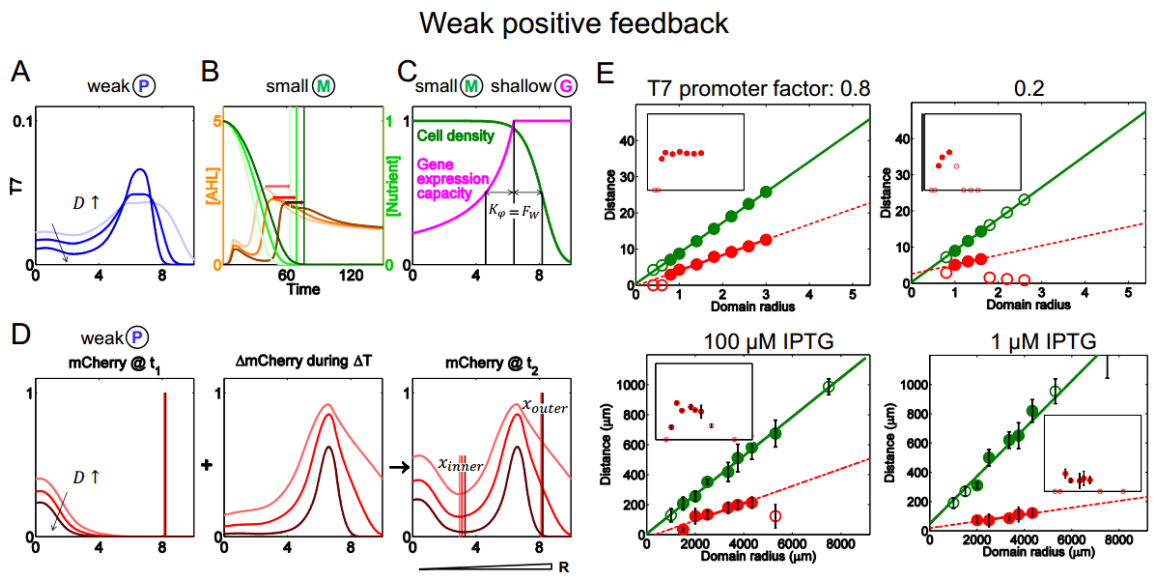

Figure 11: Scaling property of patterns for a weak positive feedback. A. T7RNAP profiles at the ring initiation time (t_1) on a normalized axis for varying domain radii (1 and 1.4). Because of the weak positive feedback, the profile of T7RNAP is not flat along x-axis, and it is not proportional over domain radius. **B. AHL and nutrient concentrations over time for different domain radii.** In this case, the ring maturation time ΔT is decreasing when domain radius D is decreasing. **C. Cell density and gene expression capacity profiles along the normalized axis, for a domain radius of 1. K_φ** equals to F_W. **D. Maturation of the mCherry ring from t_1 to t_2. mCherry @ t_1:** The initial mCherry profiles (red curves) for different domain radii do not overlap. **ΔmCherry during ΔT:** Because ΔT is not proportional to D, ΔmCherry in this case is not scale invariant. **mCherry @ t_2:** After adding the accumulation profile on the mCherry

profile at $\boldsymbol{t_1}$, the inner edge of the mCherry ring is not scale invariant. All the three figures, light red to dark red present measurements in domain radius varies from 1 to 1.4. **E. Modulating the scaling property by using weak T7RNAP positive feedback.** Top: Simulated scaling property with varying positive-feedback strength (the T7 promoter rate is 0.8 and 0.2 fold of promoter rate when circuit is fully induced). The feedback strength decreases from left to right. The figure symbols are the same as those in Figure 4D. Bottom: Experimentally measured scaling property in the presence of 100 μM (left) and 1 μM (right) IPTG. The insets represent the ratio of the ring width to the colony radius. The x-axes for the insets are on the same scale as the corresponding figure panels; the y-axes range from 0 to 1.

3.5.12 Comparison with representative mechanisms for pattern generation and scaling

Researchers have sought to define mechanisms underlying pattern formation and scaling as early as the 1950s. These mechanisms either focus on generation of patterns by self-organization or by interpreting pre-defined gradients of chemicals (morphogens).

Turing was the first to propose a reaction-diffusion (RD) model consisting of interlocking positive and negative feedback loops involving two diffusible morphogens, to explain self-organized pattern formation [102]. The original Turing model cannot generate scale invariance. However, variants of the Turing model have been proposed to account for scale invariance. These include models that assume concentration-dependent diffusion coefficients or size-dependent reactions.

If the diffusion coefficients of morphogens depend on the concentration of another diffusible molecule produced by all cells at a constant rate, the Turing model can support generation of patterns that scale with size [103-105]. This mechanism has been proposed to explain pattern formation and scaling during the embryonic

development, such as scaling during the slug stage of *Dictyostelium discoideum*. However, it requires some stringent dynamic constraints that lack direct experimental evidence. These include: 1) the morphogen diffusivities must be proportional to the square of the length scale, and 2) matching between the production rate and leakage rate of the morphogen into the surroundings.

Another extension of the Turing model is the **size-dependent reaction model** [106-109]. In addition to the two morphogens assumed in the Turing model, this model introduces another chemical whose concentration depends on the size of the reaction environment. The model further assumes that chemical is generated in a localized region of the system and it diffuses fast. As a result, its concentration is proportional to the inverse of the square of the environmental size. In this theoretic model, each morphogen has two states – active or inactive. Transition between the two states is catalyzed by this chemical. Only morphogens in the active state can participate in reactions. Satisfying these conditions, scale invariance can arise from the modified Turing model. A limitation of this model is the lack of direct experimental evidence for the key model assumptions. However, the AHL in our system can be considered as fulfilling some of the roles proposed for the additional chemical in the size-dependent reaction model. AHL concentration also approximately scales with the inverse of the square of the domain size; it also plays a critical role in modulating some reactions in our system.

In contrast to models mentioned above, the other class of models focuses on interpretation of pre-defined chemical gradients by downstream processes. A classical model is the positional information model (or the French Flag model), proposed by L. Wolpert [51]. The essence of this mechanism is a pre-defined morphogen gradient that is interpreted by downstream genes, where different genes are activated at different ranges of the morphogen concentration. In this framework, the scaling property of the final patterns is determined by the scaling property of morphogen gradients. Several models have been proposed to generate scaling morphogen.

A perfect sink model assumes that the morphogen is generated at a source and degrades at a distant edge. As a result, it forms a linear gradient from source to sink. This mechanism could support scale invariance [105, 110]. This theoretic model requires strict conditions to ensure a perfect sink to ensure scale invariance in the morphogen gradients.

Another model assumes **integration of two opposing gradients**, where two morphogens are produced at opposite ends of the developing field. There is an effective annihilation reaction between the two morphogens. Cells control the size of the pattern by the ratio of two gradients [111].

A shuttling-based mechanism requires two pre-defined morphogens: an activator and an inhibitor. Efficient shuttling requires binding of the ligand to the inhibitor to facilitate its diffusion and subsequent release of the ligand by cleavage of the

complex. The morphogen profile is reshaped by the physical translocation of the activator to the midline, mediated by its binding to the inhibitor. This mechanism is supported by data in *Drosophila* and *Xenopus* embryos [112]. This mechanism is further generalized to **an expansion-repression (ExR) model**. In the ExR model, a single morphogen is secreted from a local source and diffuses in the field of cells to form a distribution profile that has a peak at the source. The diffusion of this morphogen is facilitated by a diffusible molecule, the "expander". However, the production of the expander is repressed by the concentration of morphogen. With appropriate parameters, the ExR model can generate a scale-invariant morphogen gradient [47, 53, 69, 113].

The mechanisms above have focused on generation or interpretation of morphogen gradients by feedback control only. Recent studies have suggested an important role of tissue growth and expansion in establishing the morphogen gradients, by contributing to the transport and accumulation of the morphogen molecules [45, 49]. The resulting morphogen gradients in turn can influence the tissue growth and expansion.

Aspects of our mechanism are related to the mechanisms mentioned above:

1. Our model is analogous to the Turing model in two aspects: (1) our model also relies on self-organized pattern formation; (2) our circuit logic is identical to the Turing model. The critical difference is that the activator is transported by advection in our system but by diffusion in the Turing model.

2. AHL serves a similar role of the catalyzing chemical in the size-dependent reaction model. Its concentration is reflects the dimension of the domain, and it regulates rates of reactions involving other molecules.
3. Our circuit logic also resembles that of the expansion-repression model, where T7RNAP serves as the expander, T7 lysozyme serves as the repressor, and morphogen AHL serves as the regulator between them. However, a critical difference is that AHL in our system primarily serves as a timing cue in modulating the rates of other reactions (as in point 2).
4. In our system, colony growth and expansion play a major role in establishing the initial profile of mCherry during the first stage of pattern formation, by contributing to the transport and accumulation of intracellular proteins. This aspect is reminiscent of the computational analysis by [45, 49], which emphasizes the role of tissue growth and expansion in establishing morphogen gradients in a natural system.
5. The integration of the mCherry profile at the end of the first stage and the mCherry increment during ring maturation (Figures 3, 5) is analogous to the two opposing gradients model.

4. Programmed Assembly of Pressure Sensor using Pattern-formation Bacteria[1]

4.1 Introduction

Nature is a master in fabricating structured materials consisting of living and non-living components from bottom up. These materials often have diverse, well-defined physical properties. For example, mollusk shells are composite materials that form multilayered microstructures, consisting of primarily calcium carbonate interlaced with a small amount of organic components[114]. Because of this composite microstructure, mollusk shells are three orders of magnitude tougher than non-biogenic calcium carbonate[115, 116]. In contrast to conventional physical and chemical synthesis methods, biological fabrication is "green" and often relies on the self-organized assembly of building blocks. While inspiring, natural biological processes of material assembly are not readily programmable, which limits our ability to use them to generate materials of desirable properties that do not yet exist in nature.

Advances in synthetic biology and biomaterials engineering over the past fifteen years make it possible to fabricate living materials from the ground up[117-119]. Numerous studies have demonstrated the formation of self-assembled structures[120-

[1] Author contributions: LY and YC conceived the project. YC generated and analyzed all the experimental data. YC developed MATLAB codes for image analysis. YC and YF designed and carried out the electrochemical pressure sensing experiments. MDR and GH developed the numerical simulator for 3D pattern formation. YC conducted parameter fittings in all simulations and generated the final simulation results. KZ assisted with immunolabeling and TEM imaging. KM assisted with TEM imaging. YC, SZ, and LY wrote the manuscript, with inputs from YF, MDR, KZ, GH, and KM.

123] that consist of biomolecules as building blocks, including proteins[124-126], peptides[127-129], and DNAs[130-133]. For example, the naturally occurring protein S-layer protein can self-assembled into different shapes, like sheets, or open cylinders[134]. This self-assembled protein structure can serve as the template for assembling cadmium sulfide (CdS) nanocrystals into a super lattice structure[135]. Instead of directly using the natural biological construct, researchers have engineered bacteria to control biofilm formation to assemble inorganic materials across various length scales. The conductive biofilms generated from this inorganic-organic system combined with electrode could be externally controlled as electronic switches[89].

Fabrication of structured materials based on the programmed self-organization of living cells represents the next frontier at the interface of synthetic biology and materials engineering. It draws inspiration from biological fabrication in nature; yet it applies engineering principles to achieve predictable control of material structures and functions at two layers: programmed self-organization of cells and assembly of cellular products to interact with the environment.

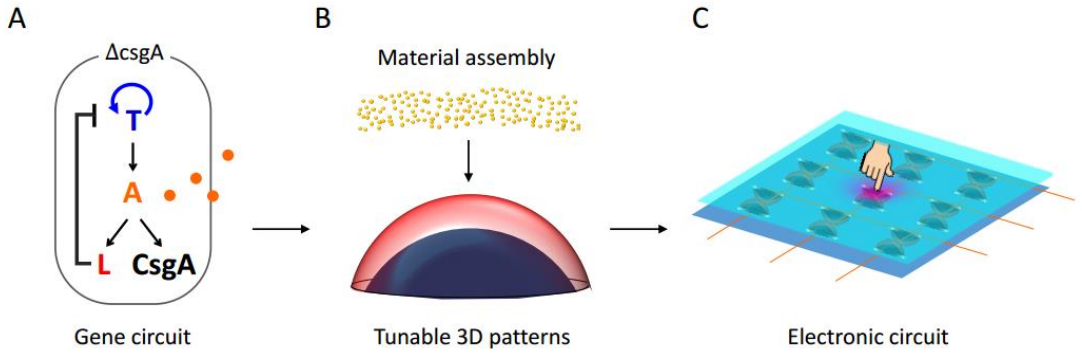

Figure 12: Programmable material fabrication using engineered pattern-forming bacteria. A. The curli-pattern circuit is built upon a pattern-formation circuit developed by Payne et al.[24]. The original circuit consists of T7RNAP that activates its own expression as well as the expression of LuxR and LuxI. LuxI mediates synthesis of AHL, which in turn, through activation of LuxR, drives expression of T7 Lysozyme and an mCherry reporter. In the revised circuit, CsgA containing a 6×-His tag is co-expressed with the lysozyme and mCherry. When expressed in a host strain producing CsgB, CsgA and CsgB will form curli that can interface with inorganic materials. **B. Material assembly by pattern-forming bacteria.** Bacteria containing the curli-pattern circuit can form self-organized curli patterns in each colony. The curli pattern can serve as the scaffold to assemble inorganic materials. The colony and the corresponding curli pattern are both programmable by gene circuit parameters and the growth environment. **C. The bacterially assembled materials are used as modules for building functional devices.** The schematic illustrates a "touch pad", that could sense and transduce local pressure variations. The dome shape represents the micro-structured material made from the colony; the orange lines represent conductive wires; and the two blue planes represent supporting surfaces.

Here, we extended the design strategy by using pattern-forming bacteria, programmed by synthetic gene circuits, as the structural scaffold. These bacteria are engineered to produce and assemble extracellular fibrils with functional tags into three-dimensional (3D) patterns. These patterned fibrils in turn enable assembly of inorganic materials. This two-layer control enables assembly of structured materials that have well-defined physical and chemical properties (Figure 12).

4.2 Results

4.2.1 Pattern-curli formation

We recently developed a synthetic gene circuit (Figure 12) to program bacterial pattern formation in two-dimension (2D)[24]. The circuit consists of a mutant T7 RNA polymerase (T7RNAP)[57] that activates its own expression and that of LuxR and LuxI. LuxI synthesizes an acyl-homoserine lactone (AHL), a membrane-diffusible chemical that upon binding and activating LuxR, can induce expression of T7 lysozyme, which inhibits T7RNAP[58]. CFP and mCherry fluorescent proteins are co-expressed with T7RNAP and lysozyme, respectively, to report the circuit dynamics. The circuit enables generation of robust spatial patterns in the expression of mCherry[24, 28].

We extended the circuit by incorporating an engineered curli developed by Chen et al.[89]. Part of the extracellular matrix produced by many bacteria, curli consists of two components, CsgA and CsgB[136]. Chen et al. engineered CsgA to encode six histidine tags (6×-His tag) to interface with inorganic materials. I modified our circuit to co-express the engineered CsgA with the lysozyme, generating the curli-pattern circuit. I then used *E. coli* MG1655 *PRO ΔcgA ompR234* (hereafter referred to as MG1655 *ΔcsgA*) as a host strain, in which *csgA* is deleted but *csgB* is constitutively expressed.

MG1655 *ΔcsgA* cells generated no detectable fibrils (Figure 17A). In contrast, induction of the curli-pattern circuit in these cells by addition of exogenous Isopropyl-

D-1-thiogalactopyranoside (IPTG) and AHL led to extensive fibril formation (Figure 17B, C) in a dose-dependent manner (Figure 17D).

4.2.2 Inorganic material assembly to bacterial colony

These fibrils enabled assembly of gold nanoparticles conjugated with a Ni-NTA group, through the formation of a Ni (II)-NTA bound between the 6×-His tag and the gold nanoparticle (Figure 17E). To assemble other inorganic particles, I used a mouse anti-6x His tag antibody conjugated biotin (1st antibody), which can bind to anti-mouse antibody (2nd antibody) conjugated with nanoparticles. As a demonstration, I used goat anti-mouse IgG conjugated with 10 nm gold. Assembly of the gold particles occurred when both antibodies were present (Figure 17F), but not when either was absent (Figure 17G). By changing the conjugation module on the 2nd antibody, we can use the curli to assemble different inorganic nanoparticles, including CdSe quantum dots (Figure 17H).

4.2.3 Bacterial growth and pattern formation on permeable membrane

I used inkjet printing[28] to initiate single colonies on permeable membranes placed on top of agar containing growth media. The membranes serve as a structural support for colony growth and greatly facilitate subsequent assembly of nanoparticles. Briefly, I printed a 150 pL (containing ~20 cells) droplet of the bacterial culture onto each membrane. When confined in 2D, bacteria carrying our pattern formation circuit generated 2D patterns[28]. Here I did not confine the bacterial growth. After 32 hrs

incubation under 30˚C, each colony grew into a raised, convex shape, with a 3D dome pattern of mCherry expression within (Figure 13A and Figure 18A). The colony size, elevation, and the corresponding pattern were controllable by the physical properties of the membranes: hydrophobicity and pore size. For a fixed pore size, the colonies became flatter with decreasing membrane hydrophobicity. If a membrane was too hydrophobic (e.g. a PTFE membrane), it prevented the colony growth, likely by suppressing wicking of nutrient from the agar and making it unavailable to the bacteria[137]. For membranes of the same material (thus with similar hydrophobicity), the colonies became larger but not taller with increasing pore sizes (Figure 13B and Figure 18B).

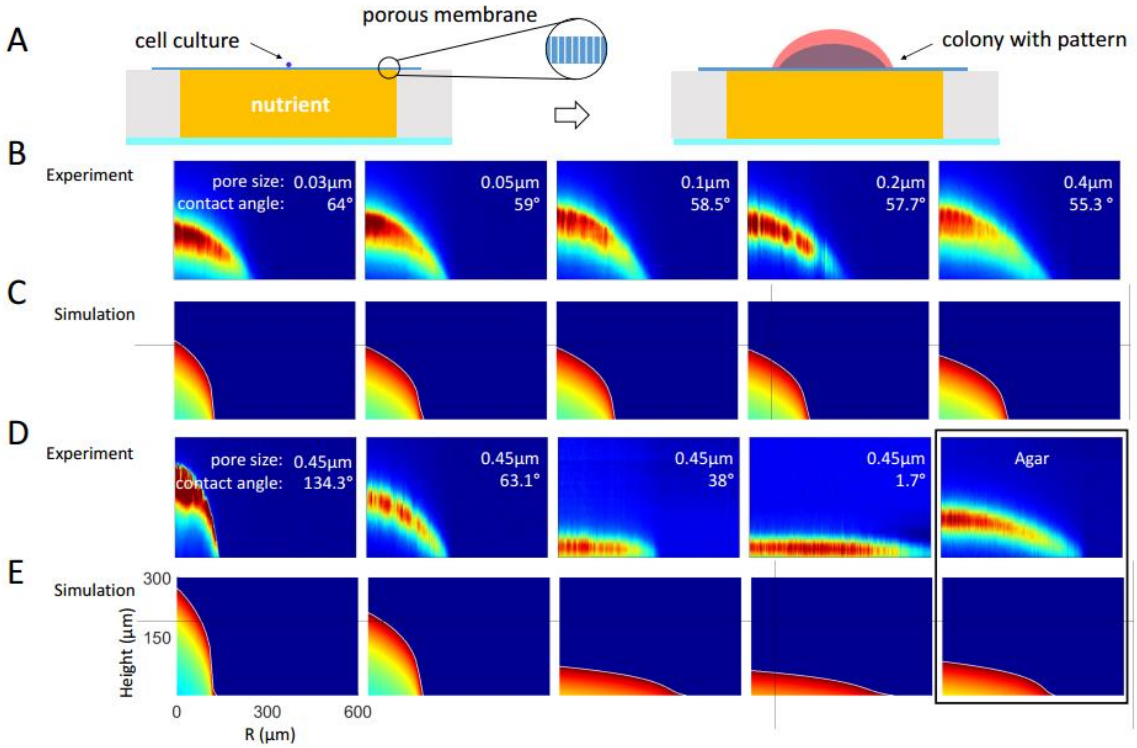

Figure 13: Bacterial growth and pattern formation on permeable membranes. A. Growing colonies on a permeable membrane. I loaded 0.3% molten agar in 2×YT with IPTG and appropriate antibiotics in a Culture Well™ multiwell chambered coverslip (Grace Bio-Labs) as the culturing device. After the agar solidified, I placed a permeable membrane on top of the culture well and printed bacteria onto the membrane surface. The diagram is not to scale. **B. Tunable dome structures on membranes with different pore sizes.** Each column represents the heat map of mCherry fluorescence patterns measured by a confocal microscope after 32 hrs incubation in both vertical (y-axis) and radial (x-axis) directions. The pore size varied from 0.03 to 0.4 µm, as indicated. The contact angles of these membranes varied slightly (from left to right: 64.0º, 59.0º, 58.5º, 57.7º, 55.3º). **C. Simulated dome structures on membranes with varying pore sizes.** In our model, I assume that the pore size affects the radius expansion rate $\boldsymbol{v}$ and the nutrient influx rate $\boldsymbol{\alpha_1}$ (Eqs. (2) and (3)), respectively. Each column represents the heat map of simulated mCherry fluorescence patterns for the varying pore sizes. **D. Experimentally tunable dome pattern on membranes with different contact angle.** Each column represents the heat map of mCherry fluorescence patterns measured by a confocal microscope after 32 hrs incubation in both vertical (y-axis) and radial (x-axis) directions. From left to right, the membrane is PVDF, PC, MCE, NC. The pore size of each membrane is 0.45 µm. Contact angle of each membrane is 134.3º, 63.1º, 38.0º, 1.7º. The most left image is colony

directly grow on 0.3% 2×YT (PH=6.5) agar. **E. Simulation results of dome pattern on membranes with different contact angle**. In our model, I assume varying contact angle affects the radius expansion rate $\boldsymbol{v}$ follows Eq (2). Each column represents the heat map of mCherry fluorescence patterns after simulation with different $\boldsymbol{v}$.

Mechanistically, the observed dependence of the colony shape on the physical properties of the membrane can be attributed to modulation of cellular motility on, and nutrient transport across the membrane. Indeed, a kinetic model incorporating these effects captured the characteristics of the dome structure, as well as its dependence on membrane properties (Figure 13C and Figure 18C). Similarly, consistent with experimental observations (Figure 13D and Figure 18D), our model shows that decreasing hydrophobicity leads to colonies with larger radii and smaller heights (Figure 13E and Figure 18E).

I next assembled gold nanoparticles using the bacteria carrying the curli-pattern circuit. Briefly, I fixed each colony by floating the supporting membrane on high concentration fixation solution and then immunolabelled gold nanoparticles onto the structure (Figure 19A and Chapter 3.4). As curli and mCherry are co-expressed, I expect their spatial patterns to overlap. Therefore, the structure of gold nanoparticles assembled by the curli should also overlap with that of mCherry. Indeed, confocal microscopy shows that the spatial distribution of the nanoparticles is similar to that of mCherry (Figure 19B), both forming a dome.

4.2.4 Fabrication of bacterial pressure sensor

The dome is a composite material consisting of inorganic gold nanoparticles distributed in an organic matrix. As the organic matrix is visco-elastic, and the gold nanoparticles are conductive, I conjectured that the assembled microstructure could serve as a pressure sensor. Consider two bacterially fabricated domes facing each other with a small distance in between, and a constant voltage applied to the edge of each dome (Figure 20A). When sufficiently pressed, the two domes make contact, which leads to the flow of an electrical current. Since the inter-particle distances decrease and the number of particle-particle contacts increase, the strength of the current should reflect the strength of the externally applied pressure.

To test this notion, I used nitrocellulose to mount a nuclepore track-etched polycarbonate (PC) membrane with a colony onto a thin glass coverslip. I then positioned two such glass coverslips (each carrying a colony) to face each other with a 0.5 mm thick silicone gasket as spacer in between (Figure 20B). Next I used copper wire to connect the edges of the colonies to an electrochemistry workstation. The workstation provided a constant voltage to the device, and recorded the changes in the electronic current flowing through the device. To actuate this pressure sensitive device, I placed a thin cylinder (~1.5 mm in diameter) right on top of the upper glass coverslip. The center axis of the cylinder was aligned with the center of the two colonies. The

device was then actuated by a programmable syringe pump, pressing on the cylinder (Figure 20C).

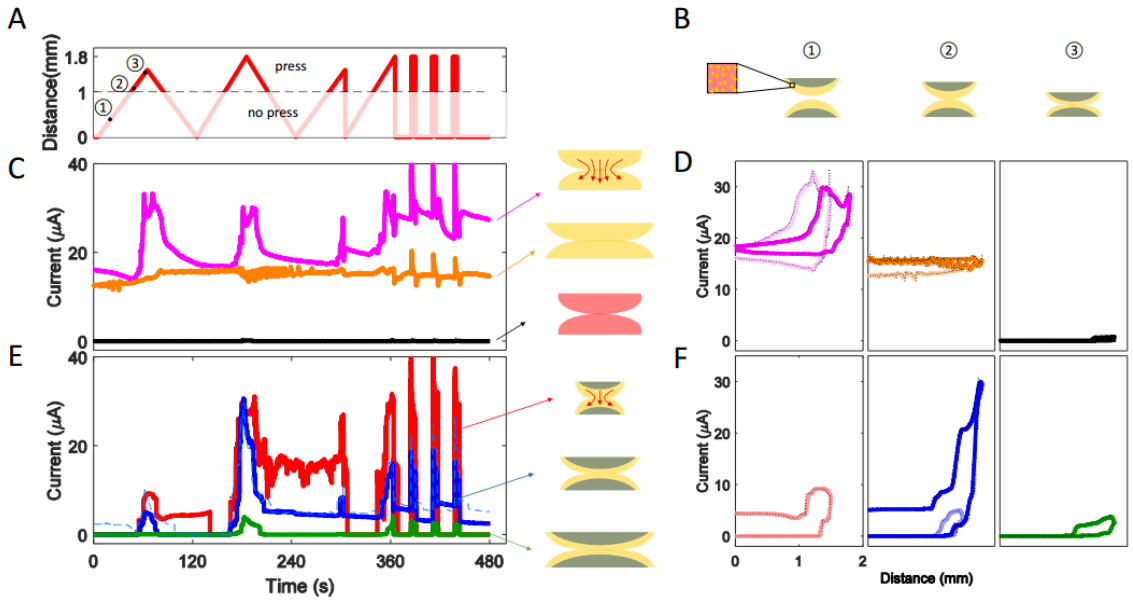

Figure 14: Patterned gold nanoparticles as a resettable pressure sensor A. Controlled compression of two opposing colonies. The distance indicates the displacement of the presser from its starting position. The presser starts to make contact with the device when the displacement is >1 mm. **B. Status of two colonies at different time point**. Different time points are labeled in Figure 14A. The yellow-blue dome shape represents the colony; yellow dome represents the cells within the colony with gold assembly. The inset image is a higher magnification of the yellow section at nanoscale: gold nanoparticles bind on curli. At time point 3, upon making contact, the two colonies would experience increasing pressure with an increasing displacement distance. **C. Colonies with uniform gold nanoparticles exhibited no differential response to pressure.** With uniform expression of induced curli in a colony, gold nanoparticles were uniformly assembled throughout the colony, as illustrated as the yellow solid spherical cap on the right-hand side. Magenta and orange lines indicate currents from colonies grown on membranes with a pore sizes of 0.03 μm and 0.1 μm, respectively. The black line indicates response of colonies of pattern-forming bacteria grown on membrane with a pore size of 0.03 μm, without assembling gold nanoparticles (illustrated as the red hemispheroids on the right-hand side). The red arrows indicate the electric current pathway. **D. Intensity of electric current as a function of the pressing distance for colonies not containing dome structured gold nanoparticles.** The left panel shows responses from a pair of colonies grown on a

membrane with a pore size of 0.03 μm. The light magenta line indicates a varying pressing distance from 0 to 1.5 mm; the magenta line indicates a varying pressing distance from 0 to 1.8 mm. The middle panel shows responses from a pair of colonies grown on a membrane with a pore size of 0.1 μm. The light orange line indicates a varying pressing distance from 0 to 1.5 mm; the orange line indicates a varying pressing distance from 0 to 1.8 mm. The right panel shows responses of a pair colonies of pattern-forming bacteria grown on a membrane with a pore size of 0.1 μm, without assembling the gold nanoparticles. The gray line indicates a varying pressing distance from 0 to 1.5 mm; the black line indicates a varying pressing distance from 0 to 1.8 mm. **E. Colonies with the dome structure exhibited differential pressure responses.** The red, blue and green solid lines indicate responses from colonies grown on membranes with pore sizes of 0.05 μm, 0.2 μm, and 0.4 μm respectively. The dashed blue line indicates replicate experiment of the solid blue line by using different electrochemical machine of the same model on a different day. The right-hand side illustrates colonies containing dome-structured gold nanoparticles. The red arrows indicate the electrons travel pathway. **F. Intensity of electric current as a function of the pressing distance for colonies containing dome structured gold nanoparticles.** The left panel shows responses from a pair of colonies grown on a membrane with a pore size of 0.05 μm. The light red line indicates a varying pressing distance from 0 to 1.5 mm; the red line indicates a varying pressing distance from 0 to 1.8 mm. The middle panel shows responses from a pair of colonies grown on a membrane with a pore size of 0.2 μm. The light blue line indicates a varying pressing distance from 0 to 1.5 mm; the blue line indicates a varying pressing distance from 0 to 1.8 mm. The right panel shows responses of a pair colonies of pattern-forming bacteria grown on a membrane with a pore size of 0.4 μm. The light green line indicates a varying pressing distance from 0 to 1.5 mm; the green line indicates a varying pressing distance from 0 to 1.8 mm.

The displacement of the actuator had different profiles, depending how fast and how strong two colonies were pressed together or separated (Figure 14A, B). First we tested the pressure response of colonies not containing the programmed structures. To this end, we used MG1655 *ΔcsgA* cells expressing the histidine-tagged CsgA under the induction of AHL[89]. When curli expression was fully induced, the assembled gold nanoparticles were distributed approximately uniformly in the colonies, forming a solid spherical cap (Figure 19B, the third column). We controlled the radii and heights

of different colonies by using membranes with different pore sizes: i.e., a larger pore size would lead to a colony with a larger radius and a larger height. Because each colony's height was >250 μm, the two opposing colonies were already in contact even without applied pressure (Figure 14C, orange line), leading to a high base-level current. Although the current increased when the two colonies were pressed together, it did not significantly vary with different displacement profiles (Figure 14C, magenta line). The lack of a strong differential response is more evident by plotting the current response against the displacement distance. Increasing displacement, i.e., increasing pressure on the device, did not cause a significant difference between the overall current levels (Figure 14D, left and middle panels). A control experiment showed that the gold nanoparticles assembled in the curli were critical for making the colonies conductive, as pressing together two colonies containing no gold nanoparticles generated no detectable current (Figure 14C, black lines; Figure 14D, right panel).

In contrast, the domes containing gold nanoparticles exhibited differential pressure responses. To control the dome shape, I grew the bacteria carrying the curli-pattern circuit on PC membranes with different pore sizes, before incubating with gold nanoparticles. The resulting colonies had different radii but approximately the same height (Figure 18B). The height was sufficiently small such that two colonies placed opposite each other in our device, were not in contact without being pressed. Thus, in the off-state (i.e., without externally applied pressure), the electrical current through the

device was approximately zero. When the two colonies were pressed into contact, the resulting current increased with increasing applied pressure (Figure 14E). we speculate that with an increasing pressure, the deformation of the dome structure would cause a tighter packing of nanoparticles near the contact point. This in turn would increases the number of conducting pathways through the device, and as a consequence, an increased electrical current at a higher pressure (Figure 14E, red arrows).

We also found that a device with smaller domes (i.e., those with smaller radii of curvature) exhibited a stronger pressure response than one containing larger domes (Figure 14E). This differential response is likely due to two reasons. First, the densities of gold particles would be similar among all domes and different domes would have similar electrical resistivity. Thus a smaller dome would have a smaller resistance than a larger dome. Second, given the same pressing distance, the pressure is higher in a smaller dome compared with that in a larger dome. Therefore, there will be more particle-particle contact in smaller domes, which in turn would increase the conductivity. Because these domes were elastic, the device could be pressed multiple times with resettable and robust readout (Figure 14E, dash line). When the pressing distance increased, there was a dramatic increase in current flowing through a device with two small domes (Figure 14F, left panel). The differential pressure response was smaller for a device with two larger domes (Figure 14F, middle and right panel).

In contrast to solid spherical cap structures, only the dome-shape structures had strong differential responses to pressure (Figure 14C, E). In a solid spherical cap structure with gold nanoparticles uniformly distributed, there are more conducting pathways for electrons (Figure 14C, red arrows) than in a dome structure (Figure 14E, red arrows). Thus, a change in the pressing distance between two colonies would have little effect on the colony resistance. Given the same change in the pressing distance, the number of conductive pathways will increase more dramatically with an increasing contact area in a dome structure.

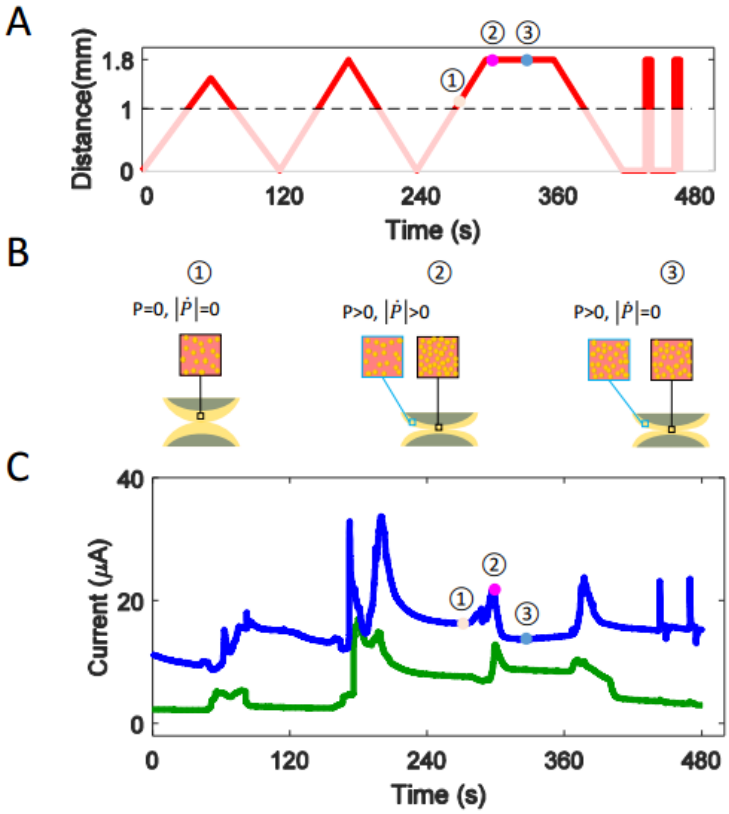

Figure 15: Patterned gold nanoparticles respond to pressure derivatives. A. The pressing distance as a function of time, with the same device configuration as in

Figure 14. B. **Distributions of gold nanoparticles corresponding to different pressure inputs.** 1) the pressure is zero; 2) the pressure and its derivative are both positive; 3) the pressure is positive, but its derivative is zero. The three time points are labeled in Figure 15A. C. **The pressure sensor responded strongly to changing pressure**. The blue and green solid lines indicate current responses from colonies grown on membranes with pore sizes of 0.2 μm and 0.4 μm, respectively.

Due to the visco-elastic behavior of the bacterial colonies, the distribution of gold nanoparticles embedded in the domes would likely respond with different conduction dynamics to different pressing profiles (Figure 15A). Without pressure, the distribution of gold nanoparticles in each dome is similar (time point 1). When two domes are pressed together (time point 2), the contact region of the two opposing domes increases and the exerted pressure leads to a densification of the local distribution of gold nanoparticles. If the displacement of the actuator is maintained, i.e., the strain on the device is held constant (the flat region between points 2 and 3, Figure 15A), then the density of the gold nanoparticles in the contact region should decrease as the stress in the visco-elastic matrix relaxes (Figure 15B), and should lead to a concomitant decrease in conductivity. In other words, at constant strain we expect to see the current flow through the device to drop. Our experimental observations confirmed this prediction. Note in Figure 15C, the reduced response corresponding to the plateau between time points 2 and 3 in the input.

4.2.5 Applications of bacterial pressure sensor

The bacterially assembled domes are robust pressure sensors – even without the precision of control by using a syringe pump. As an illustration, we used a pressure

sensor consisting of two facing colonies to control an LED light (Figure 16A). This device exhibited robust responses to manual pressure using a finger. When pressed with increasing strength, the conductivity of the pressure sensor increased and led, after amplification, to an increasing LED brightness. The brightness gradually decreased when once the pressure was removed. The pressure sensor responded similarly when it was pressed repeatedly.

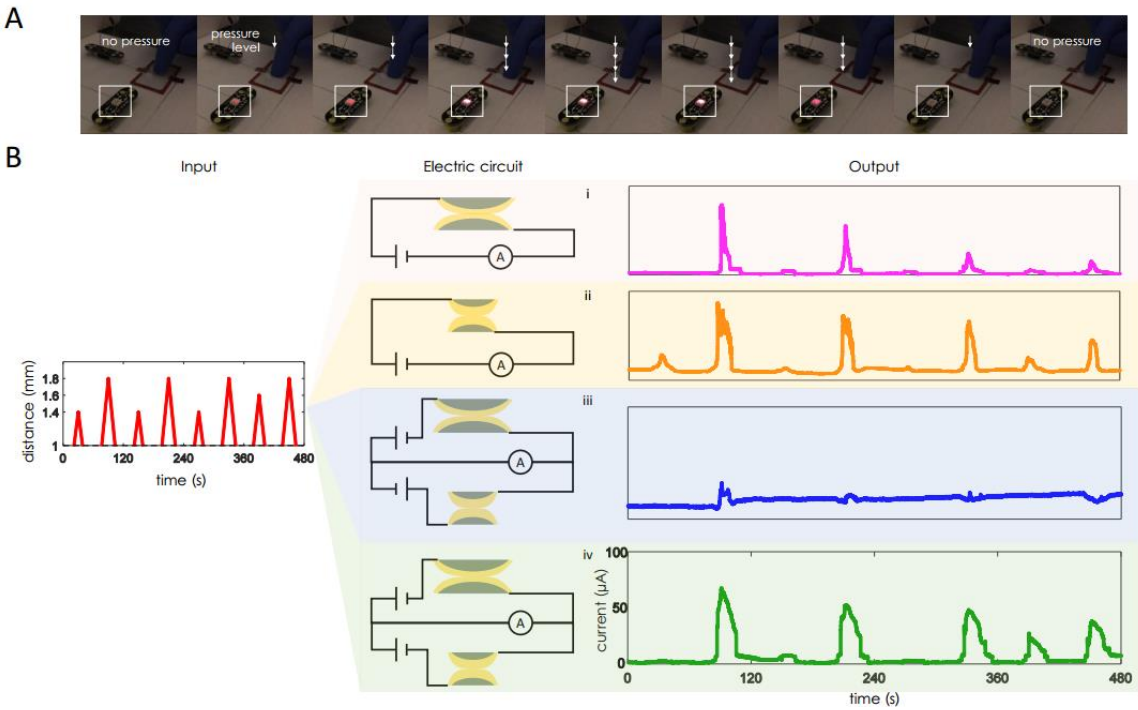

Figure 16: Robust signal processing by the bacterial pressure sensors. A. Control of an LED light using a bacterial pressure sensor in response to manual operation. The images indicate LED light intensities when the sensor was pressed to varying degrees or released. Also see Supplementary Video 1. All electronic components were from Electroninks Inc. B. **Construction of a noise filter and a signal amplifier using bacterially assembled gold domes.** As in Fig. 3E, the input is the pressing distance as a function of time. Two sets of colonies were grown on the membranes with pore size of 0.2 μm and 0.05 μm, respectively. Panel i use the sets of small domes; panel ii use the sets of large domes; panels iii and iv are used the

combination of the small and large sets of domes, but with different circuit design. Right of panel i and ii: the electric current readouts of these two sets of colonies being pressed separately. However, after combining the same sets of colonies with more complicated designs of the electronic circuits (panels iii and iv), substantial changes in the current signal were observed. Right panel iii: because the applied voltage polarities were opposite, the current signals from two sets of colonies cancelled out. Only the current with higher amplitude was selected, therefore, the electronic circuit combined with the colonies functioned as a noise filter. Right panel iv: because the applied voltage polarities were the same, current signals from two sets of colonies summed up. Hence, the output was amplified in the form of the original input signal, and the electronic circuit functioned as a signal amplifier. The x and y axis are of the same scale among i-iv panels.

The ability of the sensors to transduce differential pressure inputs makes it possible to construct more complex signal processing devices. Given the same sequence of input pressure signals with alternating strengths (Figure 16B, left panel), domes of different size would yield different responses that could be integrated by a downstream signal processor. As a demonstration, we used domes of different radii but similar heights (as controlled by membrane pore size). Each would generate its characteristic response to an alternating sequence of strong and weak pressure signals (Figure 16B, i and ii). we then used a current-cancelling circuit to subtract one response from the other. The net response exhibited distinct peaks corresponding only to strong input signals, but not to small ones. That is, the integration of these two responses led to a filtering of small variations in the pressure input (Figure 16B, iii and iv). Conversely, we used a current-adding circuit to integrate the two intermediate responses. The overall response exhibited distinctly amplified peaks corresponding to original inputs (Figure 16B, i and ii).

Finally, by placing multiple domes in appropriate spatial configurations in electronic circuits, we were able to implement location sensors (Figure 21). Each location sensor is activated when a dome is pressed. The overall resistance of the sensor is determined by the location of the pressed dome. The amplitude of the output (electric current) thus reflects the location of the pressed dome. To illustrate this design concept, We implemented multiple location sensors consisting of two, three, or four pairs of bacterially assembled gold-nanoparticle domes. Each location sensor functioned as designed (Figure 21).

4.3 Discussions

The past 15 years has witnessed tremendous progress in synthetic biology. To date, however, the progress in programming the spatial-temporal dynamics of cell populations has been limited to a handful of examples[28, 29, 95, 138-140] -- much less in comparison with other developments, such as programming of logic functions[118, 141-145], temporal dynamics of single cells[146, 147], or cell populations[148-150]. The scarcity of successful pattern-forming circuits is due to the intrinsic challenges associated with both modeling and experiments[151]. In particular, modeling spatiotemporal dynamics is typically more time-consuming and less intuitive than modeling only temporal dynamics. Similarly, experimental demonstration of patterning dynamics is typically much more difficult than that of temporal dynamics alone. Our results demonstrate the first example in programming 3D patterns in a

growing colony, by coupling gene circuit dynamics with modulation of environmental conditions. The ability to generate such 3D patterns opens the door to using engineered systems to examine the design principles of natural patterning processes in 3D, such as skeletal patterns in limb[152], tooth[153, 154], and biofilms[155, 156].

As demonstrated by our results, this capability enables fabrication of 3D materials by using the engineered pattern as the structural scaffold. Extensive work has been carried out at the interface between materials engineering and cellular engineering. By and large, however, this integration is one sided – materials are often fabricated to serve as the scaffold for controlling or characterizing cells. Much less has been done in the opposite, which is to make materials using living cells. In contrast to previous efforts to assemble materials using engineered bacteria[89, 157], our work is based on the principle of programmed self-organization. In essence, each bacterium containing the circuit contains all the information to grow into the final structure, without pre-patterning. That is, our work is an example of 3D "printing" of functional materials using self-organizing cells. Our results underscore the importance of the programmed structure in defining the physical properties of the resulting material – pressure sensing. That is, this pressure sensing capability is an emergent property enabled by the pattern-forming bacteria. In addition to pressure sensors, such biologically-fabricated structured materials could have other applications, such as plasmonics. For instance, if the domes containing gold could be used as a back contact

with solar cells while coated with a dielectric material, the system could be used to couple or trap sunlight for improved photon absorption in photovoltaics[158, 159].

By design, our fabrication process is modular. For instance, the engineered curli can be used to assemble other inorganic materials to expand the functionality of the dome structure. For example, if one replaces the gold nanoparticles with catalytic metal nanoparticles, i.e. CoP. The dome structure with catalytic sites coated on the surface could be potentially applied in water splitting[160]. The pattern-formation circuit can be replaced with circuits capable of generating other patterns[29, 95, 139] by one or multiple engineered populations. The curli can be replaced with other effector molecules to enable the growth and assembly of soft materials, such as self-organized hydrogel formation [161]. The engineering at multiple time and length scales can enable the predictable 3D assembly of materials for diverse applications in medicine[162, 163], biotechnology[164, 165] and environmental cleanup[166, 167].

4.4 Supplementary materials and methods

4.4.1 Plasmids, cell strains, and growth media

The curli-pattern circuit consists of two plasmids: pET15bLCFPT7 and pTuLysCsgA$_{His}$2CMR2, as described in the supplementary material. As a control, we used pZA-CmR-rr12y-pLuxR-*csgA*$_{His}$[89] for induced expression of curli protein. Unless noted otherwise, MG1655 *PRO* Δ*csgA ompR234* cells carrying the curli-pattern circuit or the control plasmid was used for the printing experiments. For initial overnight culture,

LB medium was used; for liquid culture experiments, M63 minimum medium supplemented with 0.2% w/v glucose and 1mM $MgSO_4$ was used; for growth on membrane experiments, 2×YT medium was used[91]. All media were adjusted with 1.0M KOH (Sigma) solution to PH=6.5 by VWR Symphony SB70P PH meter.

4.4.2 Methods

4.4.2.1 Measurement of cell density in liquid culture

Cell densities of liquid cultures were quantified using optical density (OD) measured at 600 nm absorbance using a Perkin-Elmer VICTOR3 plate reader.

4.4.2.2 Transmission electron microcopy (TEM)

10 μl fixed sample was deposited onto a 200-mesh formvar/carbon coated nickel TEM grid (Electron Microscopy Sciences) for 2 mins, then stained with 2% uranyl acetate (Electron Microscopy Sciences) for 30s. TEM images were obtained on FEI Tecnai G^2 Twin transmission electron microscope at 80 kV accelerating voltage. All these parameters were kept the same between experiments.

4.4.2.3 Scanning electron microscopy (SEM)

1 cm × 1 cm silicon wafer was immersed in 1 ml sample solution overnight. After fixation and dehydration process, wafer with samples were imaged under FEI XL30 SEM-FEG scanning electron microscope with 10kV accelerating voltage. Images were obtained at ultra-high resolution, using the secondary electron imaging mode. All these parameters were kept the same between experiments.

4.4.2.4 NiNTA-AuNP labelling

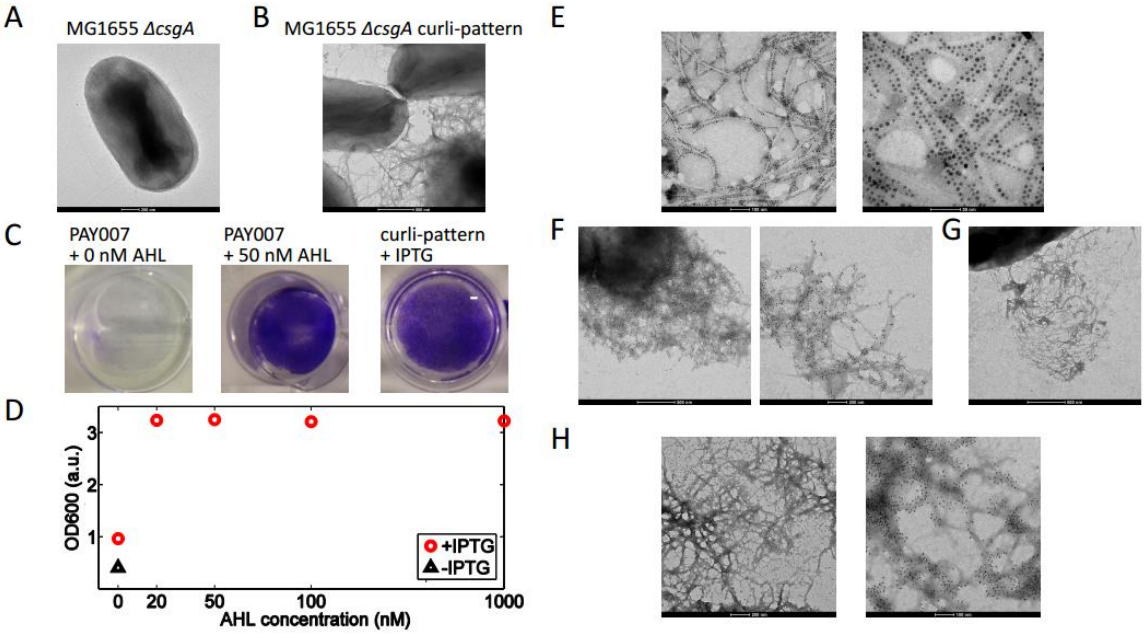

Figure 17: Construction of pattern-curli circuit. A. TEM image of MG1655 Δ*csgA* cells after 24 hrs incubation at 30 ˚C. The scale bar is 200nm. **B. *TEM* image of MG1655 Δ*csgA* cells carrying the curli-pattern circuit incubated after 24 hrs incubation at 30 ˚C**. The scale bar is 500nm. C. **Crystal violet (CV) staining assay of MG1655 Δ*csgA* cells carrying the curli-pattern circuit and MG1655 Δ*csgA* cells carrying inducible curli circuit.** CV staining assay is a standard method to stain amyloid[168]. In this case, the presence of CV stain (blue) indicates the production of curli fibril. Both samples were washed in 1× PBS for three times, then immersed in 500 μL 0.1% CV solution (Sigma) for 15 mins at room temperature. After that, the samples were washed with 1× PBS four times. Left: there was no detectable CV stain in the absence of AHL-mediated CsgA induction. Middle: CV stain was detected when CsgA was induced by 50 nM AHL. Right: CV stain was detected when bacteria carrying the curli-pattern circuit were induced by 1000 μM IPTG. D. **OD600 of CV stain dissolved in acetic acid.** The samples in Figure 17C were immersed in 500 μL of 30% acetic acid for 15 mins at room temperature. The ODs of dissolved solutions were measured at 600 nm absorbance using a Perkin-Elmer VICTOR3 plate reader. MG1655 Δ*csgA* curli-pattern circuit was used in this measurement. Circuit was induced by different amount of IPTG and AHL. E. **TEM images of curli secreted from MG1655 Δ*csgA* carrying the curli-pattern circuit assembling with 5 nm NiNTA-AuNP.** Before assembly, cells were incubated at 30 ˚C after 24 hrs. Then 5 nm NiNTA-AuNP were assembled to curli using the protocol described as NiNTA-AuNP labelling. The scale bar is 100nm. Right: TEM

image at larger magnification with scale bar of 50 nm. F. **TEM images of curli secreted from MG1655 Δ*csgA* carrying the curli-pattern circuit binding with gold nanogold using immunolabeling.** The 6×-His tag first binds with 1st antibody (mouse anti-6× His tag antibody conjugated with biotin); then 1st antibody binds to 2nd antibody (goat anti-mouse IgG conjugated with 10 nm gold). By this means, 10 nm gold nanogold particles were assembled to the curli. The scale bar is 500nm. Right: TEM image at larger magnification with scale bar of 200nm. G. **TEM images of curli immunolabeling with 2nd antibody without 1st antibody.** Antibody agents and constructs were maintained the same with Figure 17F. The scale bar is 500nm. H. **TEM images of curli secreted from MG1655 Δ*csgA* carrying the curli-pattern circuit binding with quantum dots (Qdots) using immunolabeling.** The 6×-His tag first binds with 1st antibody (mouse anti-6× His tag antibody conjugated with biotin); then 1st antibody binds to 2nd antibody (Streptavidin-655Qdots). The scale bar is 200nm. Right: TEM image at larger magnification with scale bar of 100nm.

The protocol is adapted from[89]:

20 μL of bacterial culture was placed on parafilm with TEM grid floating on top. The coated side of the TEM grid was in contact with the culture for 2 mins. The TEM was washed by 20 μL of 1× phosphate-buffered saline (PBS) 5 times (1 min for each time). The TEM grid was placed on top of 20 μL of selective binding buffer (1× PBS with 0.487 M NaCl, 80 mM imidazole, and 0.2% Tween20) for 3 times (1 min for each time). The TEM grid was placed on top of 50 μL of selective binding buffer with 10 nM 5 nm NiNA-AuNP particles (Nanoprobes) for 90 mins. The TEM grid was washed 5 times (1 min for each time) with 20 μL of selective binding buffer, and 3 times (1 min for each time) with 20 μL of 1× PBS. Before imaging under TEM, the grid was stained with filtered 2% uranyl acetate for 30 s.

4.4.2.5 Inkjet printing

I used the Epson Stylus Photo R280 Ultra Hi-Definition Photo Printer (C11C691201) for printing experiments[59]. To facilitate manipulation and sterilization, the outer dome of the printer was disassembled and removed. I then used PrintPayLess Empty Refillable Ink Cartridges. Print heads were cleaned thoroughly before and after each experiment. First, the printer head box was repositioned to the middle of the printer trail and absorbent paper towels were placed under the printer head to collect the liquid flushing through the printer heads. Second, the printer heads were flushed with 75% ethanol once, followed with washing with deionized water three times gently using a syringe. The absorbent paper towels were removed and the printer head box was then placed back in its original spot.

0.3% 2×YT agar was prepared in microwave. I then cooled the agar below 50℃ at room temperature, and supplemented it with 75 μg/mL carbenicillin, 50 μg/mL chloramphenicol, 50 μg/mL spectinomycin, 50 μg/mL kanamycin, 1000 μM IPTG (optional), and 100nM acyl-homoserine lactone (AHL). I next pipetted 170 μL of the agar into each culture well (Grace Bio-Labs; Bend, OR, USA; Item #103310), and let it solidify at room temperature.

An overnight culture of MG1655 Δ*csgA* cells carrying the full circuit was diluted to absorbance of 0.2 (measured by Victor 3 plate reader) and diluted another 50 fold into fresh 2×YT broth. The diluted culture was transferred into an empty ink cartridge

using a sterile syringe. The other five cartridges were filled with deionized water sterilized with a 0.2 μm filter (VWR® Syringe Filters, # 28145-477).

Printing templates were designed by GIMP software using 1-pixle diameter spots. Each template was exported to an Epson CD printer program to direct printing of bacteria to a membrane or the agar surface. When printing to a membrane, a porous membrane was placed on the top of each culture well. The porous membrane material varies from nitrocellulose (NC), GN-6 Hydrophilic mixed cellulose esters (MCE), nuclepore track-etched polycarbonate (PC), polyvinylidene difluoride (PVDF), and TE36 type polytetrafluoroethylene (PTFE). The thickness of all membranes was around 15 μm; the pore size varied from 0.05 μm to 0.45 μm. All inkjet-printed samples were incubated at 30˚C for 32 hrs. After incubation, the samples were imaged under a Leica DM16000B fluorescence microscope with a mercury excitation lamp at 5× objective, or under a Zeiss 780 confocal upright fixed stage confocal microscope with 5× objective.

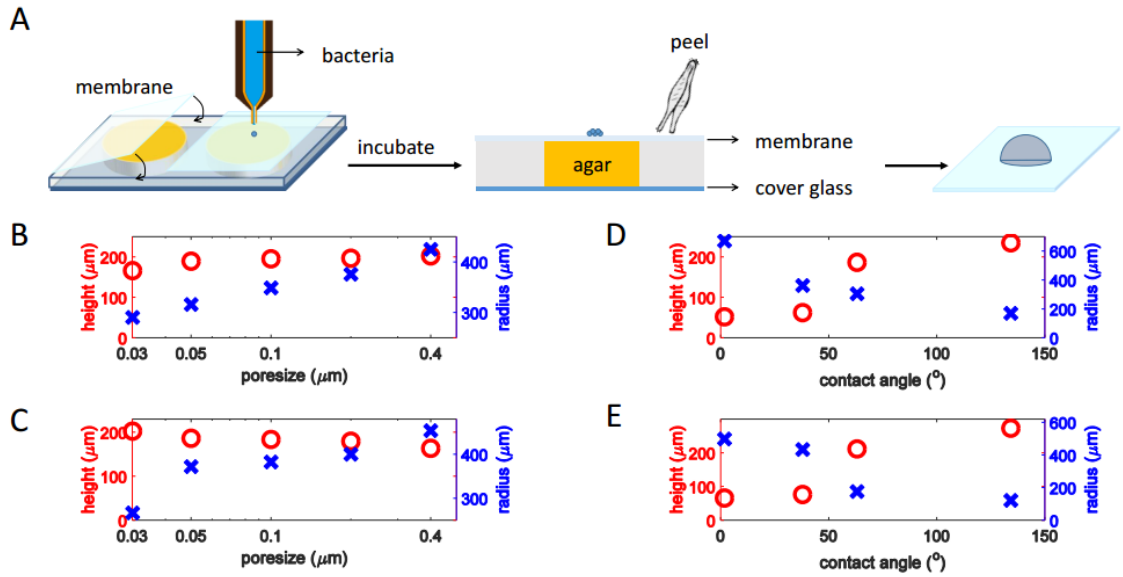

Figure 18: Bacterial growth and pattern formation on permeable membranes. A. Printing bacteria on a membrane. An initial overnight LB culture of MG1655 Δ*csgA* carrying the full gene circuit was grown for 16 hrs at 37 ˚C. 0.3% molten agar in 2×YT (PH = 6.5) medium was prepared. While allowing it to cool, I diluted the overnight culture to an OD of 0.2, and then diluted the resulting culture another 50 fold into 10 mL fresh LB culture before loading it into the inkjet printer cartridge. After the agar cooled down to 50 ˚C, IPTG and appropriate antibiotics were added. 170 μL of the agar was added to each culture-well. After the agar solidified, a permeable membrane was placed on top of the agar. I then used the inject printer to print the bacteria solution onto the membrane surface. After incubating the whole device under 30 ºC for 32 hrs, the permeable membrane carrying the colony was carefully removed by using a tweezer. **B. Heights and radii of colonies growing on PC membranes with different pore sizes after 32 hrs incubation at 30 ˚C.** The heights and radii were extracted by a custom MATLAB image analysis code from the confocal microscopy[28]. The contact angles of these membranes were 64.0º, 59.0º, 58.5º, 57.7º, and 55.3º (corresponding to increasing pore sizes). **C. Simulated heights and radii of colonies when the radius expansion rate v and the nutrient influx rate α_1 were varied according to Eqs (2) and (3), respectively. D. Heights and radii of colonies growing on membranes with different contact angles after 32 hrs incubation at 30 ºC.** The heights and radii were extracted the same way described in Figure 18B. The pore size for all the membranes was 0.45 μm. Contact angles were 1.7º, 38.0º, 63.1º, and 134.3º. **E. Simulated heights and radii of colonies when the radius expansion rate v was varied according to Eq (2).**

4.4.2.6 Immunolabeling nanoparticles to the colonies

After pealing the membrane from the agar, a membrane was washed twice by floating on top of 1× PBS twice, each wash lasted for 5 mins. The membrane was placed to float on top of 8% formal aldehyde for 24 hrs to fix the colony. After the fixation, membrane was taken out and air-dried for 5 mins. The membrane was washed with PBS twice by floating on top of 1× PBS, each wash lasted for 5 mins. After wash, membrane was placed on top of blocking buffer (6% BSA (RIA grade, Sigma Cat. no. A-7888) in 1× PBS) for 1 hr at room temperature. The membrane was incubated in the primary antibody (mouse anti-6× His tag antibody conjugated with biotin, Thermo Fisher Scientific, # MA1-21315-BTIN) diluted 1000 fold in blocking buffer overnight at 4 ºC. Followed with three times 1× PBS wash (5 mins for each wash), the membrane was incubated in the secondary antibody (goat anti-Mouse IgG conjugated with 10nm gold particles, Life Science Technologies, LLC, # G7652) diluted 10 fold in blocking buffer for 2 hrs under room temperature (note: secondary antibody in Figure 17H is Streptavidin-655Qdots, Life Science Technologies, LLC, # Q10121MP).

The membrane was washed in 1× PBS three times (5 mins for each wash)

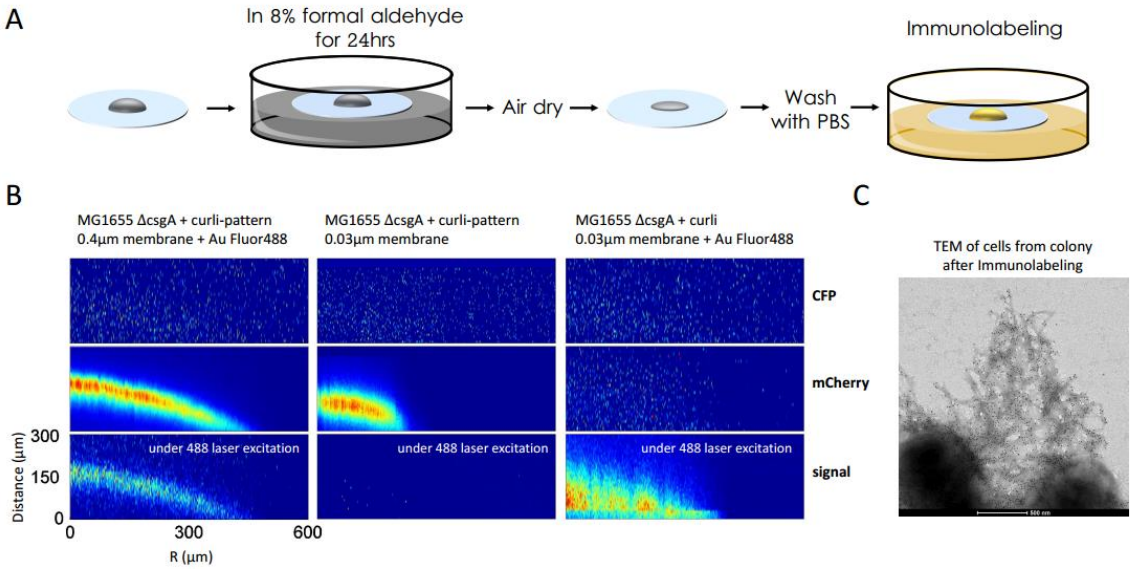

Figure 19: Generation of structured materials using bacteria carrying the curli-pattern circuit. A. Assembly of nanoparticles to a colony of bacteria carrying curli-pattern circuit. I first fixed the colony, and then used the immunolabeling to bind nanoparticles to the colony. **B. Gold particles distribute similarly as mCherry in colonies.** To examine if curli was co-expressed with T7 Lysozyme sufficiently, I compared the mCherry signal with the emission signal from the patterned nanoparticles. Left column: cells carrying curli-pattern circuit were grown on a PC membrane with a 0.4 µm pore size. Gold nanoparticles conjugated with an Alexa Fluor 488 fluorescent dye (a bright, green-fluorescent dye with excitation ideally suited to the 488 nm laser line, Thermo Fisher Scientific) were assembled onto the colony through immunolabeling. The colony was excited at 435 nm (CFP channel), 555 nm (mCherry channel), or 488 nm (green channel) during confocal microscopy. The mCherry signal matched with the emission signal from Fluor 488 dye very well: both form dome structures, indicating that gold particles distribute similarly as mCherry within the colony. Middle column: cells carrying curli-pattern circuit were grown on PC membrane with 0.03 µm pore size. No gold nanoparticles were assembled onto the colony. When the colony was excited at 488 nm, no emission signal was detected. This proved the signal observed in the left column bottom panel was emitted from the Fluor 488 dye, not from the colony itself. Right column: bacteria carrying the inducible curli circuit were grown on a PC membrane with a 0.03 µm pore size. Gold nanoparticles conjugated with the Alexa Fluor 488 fluorescent dye were assembled on colony through immunolabeling. These bacteria did not express CFP or mCherry reporter. When excited at 488 nm, the emission signal from the Fluor 488 dye formed a solid spherical cap, instead of a dome (Fig. 3D). **C. TEM of bacteria scooped from the outer-layer of**

the colony (shell part) carrying curli-pattern circuit after immunolabeling. The colony was grown on top of a PC membrane with a 0.4 μm pore size. The TEM image shows 10nm gold nanoparticles bound to curli fibrils. This result shows that the bacteria from the curli dome have efficiently assembled the nanoparticles.

4.4.2.7 Electrochemical measurement

Currents though the device were measured with a Bio Logic SP-200 electrochemistry workstation, at 1 V applied voltage (Figure 20).

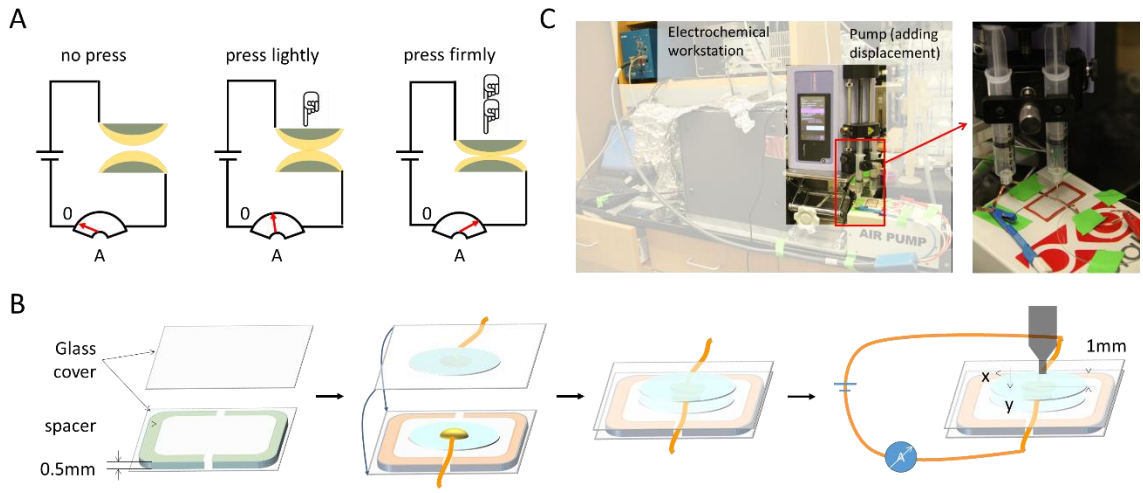

Figure 20: Assembly of the pressure sensor. A. Design concept. Black lines represent conductive wires. In the absence of pressing, the two colonies are separate and there is no electric current passing through. When pressed together lightly, a small current can go through the two colonies via their contact. The current increases with increasing pressure that enhances the contact. **B. Implementation of the sensor.** Two PC membranes carrying colonies were mounted to the surfaces of two glass covers with nitrocellulose (Electron Microscopy Science, 72180). Copper wires were used to link the edge of the colony. The two glass covers (each carrying a colony) were placed to face each other with a 0.5 mm spacer (Grace Bio-Labs Press-To-Seal silicone isolator) in between. The other ends of both copper wires were linked to the positive and negative terminals of an electrochemistry workstation. A syringe needle controlled by a programmable syringe pump was used as a "presser" (18ga × 1.5", Blunt Tip) to press the colony sensor. The diameter of the syringe needle was 1.5 mm. It was placed 1 mm right above the top of the glass cover. The top projection of the cylinder aligned with the location of the colony. **C. Configuration of the overall testing device for the**

pressure sensor. The electrochemical workstation provides a constant voltage, and measures and records the electric currents resulting from the bacterial pressure sensors.

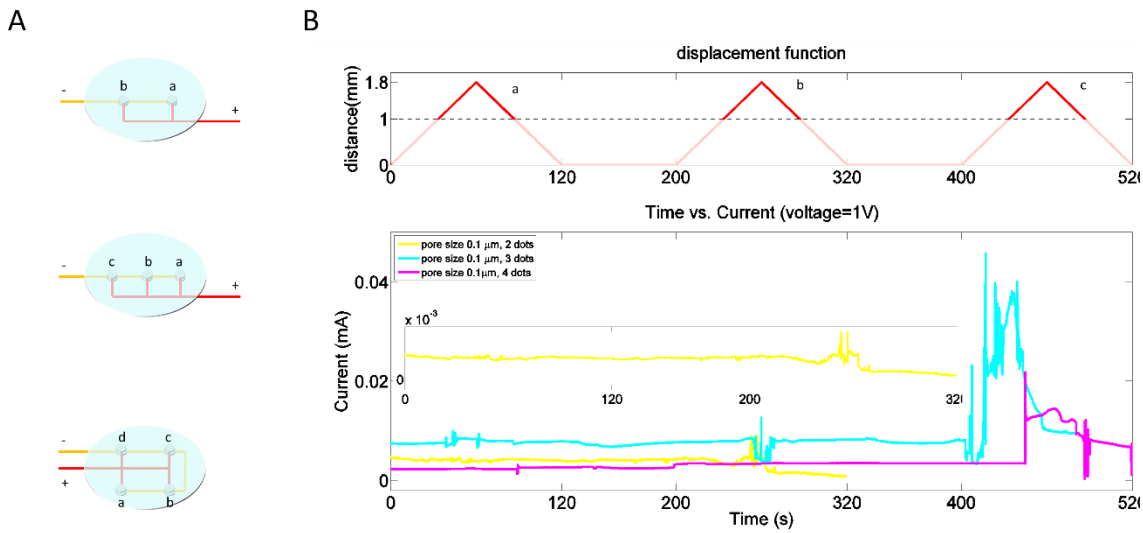

Figure 21: Multi-colony location sensors. A. Design of two-colony, three-colony, and four-colony location sensors. Similar to Figure 20, in each device, colonies and conductive wires were mounted onto two membranes. Mounted to the bottom membrane, the yellow wires connected colonies to the negative terminal of the voltage. Mounted to the top membrane, the red wires connected colonies with to positive terminal of the voltage. To differentiate which colony was pressed, I labelled them a, b, c, and d based on the locations. Note: red and yellow wires are the same type of conductive copper wires. **B. Current responses to pressing at different locations.** The top panel indicates the pressure input – the pressing distance as a function of time at different locations. When applicable, the first pulse was applied to location 'a', the second pulse to 'b', the third pulse to 'c', and the forth pulse to 'd'. The bottom panel indicates the current responses from pressing at different locations. In the same device and at the same strength of pressing, the amplitude of the output current is determined by the location of the pressing. For example, in 2-colony device, the peak current from location 'b' is higher than location 'a'. The pore size of all the membranes used in this set of experiments were 0.1 μm.

4.4.3 Model development

4.4.3.1 Colony growth dynamics

We first model colony growth in the absence of the gene circuit using a phenomenological and computationally efficient differential equation model. Because of its radial symmetry when growing on top of a flat membrane (Figure 13A), characterize the colony by two variables:

1) The radial extension $R(t)$ on the membrane at time t
2) The height function $h(r,t)$, which determines the height of the column of cells situated at a distance r from the center of the colony.

Colony growth is regulated by the amount of nutrient in the colony, $N_c(t)$, which in turn depends on the amount of nutrient in the agar, $N_a(t)$.

Our model consists of the following differential equations:

$$\begin{cases} \dot{R} = v\dfrac{n_c}{n_c + K_p} \\ \dot{h}(r,t) = \gamma\dfrac{n_c}{n_c + K_p}h(r,t)\dfrac{Q^m}{Q^m + h(r,t)^m}, \qquad 0 \le r \le R \\ \dot{n}_a = -\alpha_1 R^2(n_a - n_c) \\ \dot{N}_c = \alpha_2 R^2(n_a - n_c) - \beta_m\dfrac{n_c}{n_c + K_m}V_c - \beta_p\dfrac{n_c}{n_c + K_p}V_p \end{cases} \tag{1}$$

where,

- $n_a(t) = \frac{N_a(t)}{V_a}$ is the nutrient concentration in the agar at time t and V_a is the volume of the agar;

- $V_c(t) = \int_{r<R(t)} h(r)dr$ is the volume of the colony at time t;
- $n_c(t) = \frac{N_c(t)}{V_c(t)}$ is the nutrient concentration in the colony at time t;
- $V_p = \int_{r<R} h(r) \frac{Q^m}{Q^m + h(r)^m} dr$ is the total volume of cells that undergo proliferation;
- other constants in Eq (1) are explained in Table 3.

Table 3: Definition and the value of parameters used in the ODE model

Parameter	Description	Value	Base Unit
v	maximum expansion rate of colony radius	0.5	mm·hr^{-1}
γ	maximum expansion rate of colony height	5	hr^{-1}
K_p	half-saturation for proliferative stimulation	2	molecule·μL^{-1}
K_m	half-saturation for metabolic stimulation	60	molecule·μL^{-1}
Q	half activation distance for growth	5.67	μm
m	Hill coefficient of colony-height-mediated growth inhibition	3	
α_1	influx rate for agar nutrient concentration	0.5	molecule·hr^{-1}·μL^{-1}
V_a	agar volume	170	μL
α_2	influx rate for colony nutrient	1.7	molecule·hr^{-1}
β_m	nutrient depletion rate constant due to basal metabolic activity	1	molecule·hr^{-1}·μL^{-1}
β_p	nutrient depletion rate constant due to cell growth	10	molecule·hr^{-1}·μL^{-1}
ρ	membrane pore size	0.03 - 0.4	μm
θ	membrane contact angle	1.3 - 134.3	º
M	Hill coefficient of AHL mediated gene expression	2	

n	Hill coefficient for distance-dependent gene expression capacity	1	
K	Half activation distance for gene expression	100	μm

In deriving the above equations, we made the following assumptions:

1. The colony expands radially at a speed that depends on the nutrient concentration (n_c), analogous to Monod kinetics (see [28] for details). With saturating nutrients, the colony exhibits traveling wave solutions with an asymptotic speed v. Because cells consume nutrients, depletion of nutrient leads to decrease in the wave speed as modeled by means of the $\frac{n_c}{n_c+K_p}$.
2. At each position r where the colony touches the membrane ($0 \leq r \leq R$), the colony has a vertical growth rate $\dot{h}(r,t)$ that increases with the availability of nutrient ($\frac{n_c}{n_c+K_p}$) and decreases with the height ($\frac{Q^m}{Q^m+h(r,t)^m}$).
3. We assume fast diffusion of nutrient in both agar and colony, leading to a homogeneous distribution in each compartment. Nutrient transfer from agar to colony takes place across the membrane. The rate of exchange is proportional to the area of contact between colony and membrane and the concentration gradient between the two compartments. The nutrient exchange accounts for the third equation and the first term in the fourth equation in (1).
4. In the colony, nutrient is depleted by the cells. We assume all cells to have a baseline metabolic resorption rate, captured by the second term in the fourth

equation in (1). The last term in the equation accounts for depletion by cells undergoing proliferation.

In the experiments, the membrane pore size ρ and hydrophobicity (as measured by the contact angle θ) were varied as control parameters. To account for the impact of these parameters on the model, we assume that the radius expansion rate (v) is a function of the pore size (ρ) and the membrane contact angle (θ), and that the influx rate for agar nutrient concentration (α_1) is a function of ρ. More precisely, we use the following empirical equations:

$$v = \left(\frac{20}{\left(1 + \frac{\theta}{40}\right)^{10}} + 0.1 \right) (0.25\rho^2 + 0.95) \tag{2}$$

$$\alpha_1 = 0.01\rho^2 \tag{3}$$

Before simulating the colony growth, we rescale the variables as

$$\widehat{n_c} = \frac{n_c}{K_p}, \qquad \widehat{n_a} = \frac{n_a}{K_p}, \qquad \hat{h} = \frac{h}{Q}, \qquad \hat{t} = t\gamma$$

Omitting the hats for notational simplicity, the model equations can be rewritten using the parameter groups G_i (see Table 4),

$$\begin{cases} \dot{R} = G_1 \dfrac{n_c}{n_c + 1} \\ \dot{h}(r,t) = \dfrac{n_c}{n_c + 1} h(r,t) \dfrac{1}{1 + h(r,t)^m} \\ \dot{n}_a = -G_2 R^2 (n_a - n_c) \\ \dot{N}_c = G_3 R^2 (n_a - n_c) - G_4 \dfrac{n_c}{n_c + G_5} V_m - G_6 \dfrac{n_c}{n_c + 1} V_p \end{cases} \tag{4}$$

Because systems (1) and (4) are infinite dimensional (the equation for h is defined for each $r < R$), we discretize the radial dimension of the colony into 100 equally spaced elements of size 50. We then solve the resulting system of ODE using a stiff differential equation solver (ode23s) in MATLAB. The initial conditions are specified as: $R(0) = 0.1$; $h(r, 0) = 0.1\big(0 \leq r \leq R(0)\big)$; $n_a(0) = 50$; $N_c(0) = 0$. The computational domain only provides the computational range for running the simulation. Consequently, we choose a computational domain large enough to avoid pattern interference with the boundary and to enforce no-flux boundary conditions.

4.4.3.2 Expression profiles

Based on the model of the colony growth dynamics developed in the previous section, we can now quantify the final gene expression profiles. To this end, we use the above model to compute the colony shape in the quasi-stationary state where nutrient has been depleted. We then compute the corresponding steady-state profiles of T7RNAP (denoted as T) and T7 lysozyme (denoted as L), the T7-lysozyme complex (denoted as P), and AHL (denoted as A). The equilibrium equations for gene expression are given by the following nonlinear system, see [28] for details and Table 4,

$$\begin{cases} \dot{A} = 0 = -G_7 \int_{\Omega} \frac{T}{1+T} \frac{1}{1+P} \varphi(r,K) dV - G_8 A & (5) \\ \dot{L} = 0 = -G_9 L + G_{10} \theta(C) \frac{T}{1+T} \frac{A^M}{1+A^M} \varphi(r,K) & (6) \\ \dot{T} = 0 = -G_{11} T + G_{12} \theta(C) \frac{T}{1+T} \frac{1}{1+P} \varphi(r,K) & (7) \\ P = \frac{G_{13}}{G_{14} G_{15}} TL & (8) \end{cases}$$

where the function φ represents the gene expression capacity,

$$\varphi(r,C) = \begin{cases} \frac{K^n}{K^n + (R-r)^n}, & r \leq R \\ 1, & r > R \end{cases} \quad (9)$$

With R the colony radius, see (1) and (4). In (6) and (7), θ is the Heaviside function ($\theta(x) = 1$ if $x > 0$ and $\theta(x) = 0$ otherwise). C is the cell density, when cell density reach the carrying capacity, $C = 1$.

Ignoring A for a moment, the equations (6) - (8) form a cubic polynomial system in T and L. One can determine the solution of this system analytically and find that there is one zero root. The remaining roots are either complex, or one is positive definite and the other negative definite. We assume that the steady state will obtain the positive root if it exists, and the zero root otherwise. At this point, given a value for A, we can compute the steady state profile for T and L, however Eq (5) will not be satisfied. To find a simultaneous solution we performed the following iterative procedure:

(1) Make an initial guess for $A = A(0)$.

(2) Predict $L(0)$ and $T\ (0)$ based on $A(0)$ by solving equations (6) - (8).

(3) Update the prediction for $A(0)$ by solving equation (5), to determine $A(1)$.

(4) Repeat steps (2) and (3) until the solution has converged.

In practice, we found convergence after as few as three steps of the iterative procedure with the parameters listed in Table 4.

Table 4: Expression and value of coefficient in nondimensional model

Nondimensional parameter	Expression	Value
G_1	$\frac{v}{\gamma}$	0.1
G_2	$\frac{\alpha_1}{\gamma}$	0.1
G_3	$\frac{\alpha_1 V_a}{Q\gamma}$	3
G_4	$\frac{\beta_m}{K_p\gamma}$	0.1
G_5	$\frac{K_m}{K_p}$	30
G_6	$\frac{\beta_p}{K_p\gamma}$	1
G_7	$\frac{\alpha_a \bar{c}}{\alpha_c K_a}$	0.955
G_8	$\frac{d_a}{\alpha_c}$	0.3
G_9	$\frac{d_L}{\alpha_c}$	0.0144
G_{10}	$\frac{d_L}{\alpha_c}$	0.0144
G_{11}	$\frac{d_T}{\alpha_c}$	0.3
G_{12}	$\frac{\alpha_T}{\alpha_c K_T}$	5
G_{13}	$\frac{K_T d_L}{\alpha_L}$	0.0038
G_{14}	$\frac{d_L}{\alpha_L k_D}$	0.0000864
G_{15}	$\frac{K_P d_L}{\alpha_L}$	0.0013

5. Concluding Remarks and Future Directions

5.1 Concluding remarks

The central theme of our thesis is to identify the major elements driving pattern formation, understand the mechanism underlying scale-invariant patterns, and apply bacterial patterns to the fabrication of functional structured materials.

In chapter 1, I first reviewed five basic elements underlying the generation of periodic patterns. These include negative feedback, time delay, positive feedback, nonlinearity in regulation, and random fluctuations ("noise") in cellular processes. The specific roles of these five elements in promoting or attenuating periodic patterns were discussed. I discussed commonly seen spatial oscillations, and the role of each design element in such examples. In summary, by reviewing literatures of modeling and experimental works on the generation of periodic patterns, I have summarized the role of design principles underlying oscillatory behavior. The in-depth discussion of each element and the biological insights will benefit the studies in developmental biology, biophysics, systems biology, synthetic biology, and applied mathematics.

In chapter 2, we examined the scaling dynamics of pattern formation in *E. coli* programmed by a synthetic gene circuit [24]. The morphogen in our system is highly diffusible; it serves as a timing cue to coordinate the patterning process. Importantly, the temporal dynamics of the morphogen are coupled with the size of the growth

environment; this coupling enables a colony to sense the size of the environment and time the pattern formation accordingly.

By integrating both modeling and experiment, we demonstrated that our system can generate robust core-ring patterns of mCherry, which reports the transcription of the T7 lysozyme. Most surprisingly, **the width of the ring pattern exhibits scale invariance with respect to the colony size.** Our modeling analysis reveals a novel mechanism, a collective space-sensing mechanism, that underlies the scale invariance. Briefly, the mechanism entails sequential actions of an integral feedback loop and an incoherent feedforward loop. The integral feedback is implemented by the accumulation of a diffusive chemical produced by a colony in the growth environment. This accumulation, combined with nutrient consumption by the colony, sets the timing for forming the core and initiating the ring. The incoherent feedforward loop is implemented by the opposing effects of domain size on the rate and duration of ring maturation. This mechanism underscores the timing control in achieving robust scaling in self-organized patterns.

Our work differs from but complements with conventional developmental-biology research on pattern formation. Due to the complexity of natural systems, many confounding factors complicate quantitative experiments and data interpretation, often making it difficult to draw definitive conclusions. In comparison, our synthetic system

provides a well-defined context to probe principles underlying the scaling property of self-organized pattern formation.

The fundamental premise of this approach is that the principles defined in such engineered systems can be generally applicable to natural examples. Indeed, the lessons learned from the Chapter 1 emphasize a new perspective in examining scaling property of self-organized patterns. Instead of always assuming a static view of the spatial morphogen gradients, **our mechanism underscores the importance of temporal control in generating scale-invariant patterns.** Evidence from the literature suggests that this notion may be generally applicable. For example, geometrically, the patterning process in our system resemble that during the embryonic development in birds and reptiles that occurs in a hard-shell egg. Dynamically, it provides novel interpretations for pattern formation in the vertebrate neural tube. The morphogen used to control the pattern of neuronal subtype formation is much higher than needed to trigger the pattern [84, 169]. It has been shown that the duration of morphogen is as critical as its spatial gradient in controlling the patterning dynamics [86]. These observations, along with mine, suggest that the conventional emphasis on a spatial morphogen gradient could underestimate the contribution of the temporal morphogen dynamics.

In Chapter 3, I illustrate a design strategy to use pattern-forming bacteria programmed by synthetic gene circuits as the structural scaffold to assemble inorganic materials. This two-layer control enables assembly of three-dimension (3D) structured

materials that have well-defined physical and chemical properties. In particular, we showed that these bacterially fabricated structured materials function as pressure sensors, which in turn can be used as modules for building more complex signal-processing systems.

This work makes several conceptual and technological advances. It is the first demonstration of **programming 3D patterns in a growing colony**. In the past 16 years, tremendous technical progress has been made in programming single cells or cell populations by using gene circuits. Hundreds of gene circuits with different functions have been created during this time span. The majority of these focus on the generation of logic gates or switching behaviors. Fewer examples demonstrate the generation of oscillations. In sharp contrast, many fewer gene circuits have been engineered to program self-organized pattern formation in growing cells based on coordinated dynamics in a population. The scarcity of successful pattern-forming circuits is due to the intrinsic challenges associated with both modeling and experiments [151].

In this work, the patterning process employs a unique combination of circuit engineering and precise control of growth conditions. This capability enables fabrication of functional materials by using engineered patterns as the structural scaffold. Assembly of materials using engineered bacteria has been demonstrated in recent studies [89, 157]. However, these studies entirely rely on **pre-patterning** of cells to control the assembly of final materials in two dimensions. In contrast to these studies, our work is based on the

principle of **programmed self-organization**. With this strategy, each bacterium containing the circuit contains all the information to grow into the final structure, without depending on pre-patterning. The critical insight is the role of spatial structures (mediated by self-organized pattern formation) in conferring the physical property (pressure sensing) of the assembled gold nanoparticles. *That is, this pressure sensing capability is an emergent property enabled by the pattern-forming bacteria*. In addition, the use of porous membrane represents a major technical innovation in controlling bacterial growth, which in turn enables a layer of control over the patterning process. The ability to generate such 3D patterns open the door to use engineered system to examine the design principles of natural patterning processes in 3D.

The fabrication process presented in Chapter 3 is **modular and scalable** by design. In our results, we demonstrated the application of pressure sensing. In general, however, the same pattern-forming bacteria can be used to assemble different types of building blocks to generate other functional, structured materials. Furthermore, while we have focused on programming of 3D domes, other structures can be programmed by operating the circuits under different conditions or by using other engineered gene circuits.

5.2 Future directions

5.2.1 Generation of complex patterns

To date, my work has focused on generation of 2D or 3D patterns in individual colonies. In the future work, my colleagues and I will scale up the diversity and length scale of these programmed patterns by exploiting inter-colony interactions, enabled by inkjet printing coupled with self-organized pattern formation. Moreover, in Chapter 3, my work demonstrated that the use of membranes is an effective strategy to control the pattern-formation process that is complementary to controlling circuit parameters and seeding pattern of cells. Permeable membranes also provide decided advantages for extracellular material precipitation.

The future work can examine the combination of different factors to achieve precise control for pattern formation, materials generation or assembly, and materials analysis. These include:

- **Membrane properties**, including surface chemistry (specifically wettability), pore size, and transparency.
- **Agar density and media composition**. The agar density will affect diffusivity of nutrients through the membrane, and affect the degree of hydration on the membrane surface. Nutrient richness will affect the bacterial growth rate, which in turn affects patterning process.

- **Initial seeding condition**: initial seeding template, seeding distance, and droplet volume. In preliminary work, experiments and 2D simulations both show that the initial seeding configuration allows for the generation of more complex patterns (Figure 22).

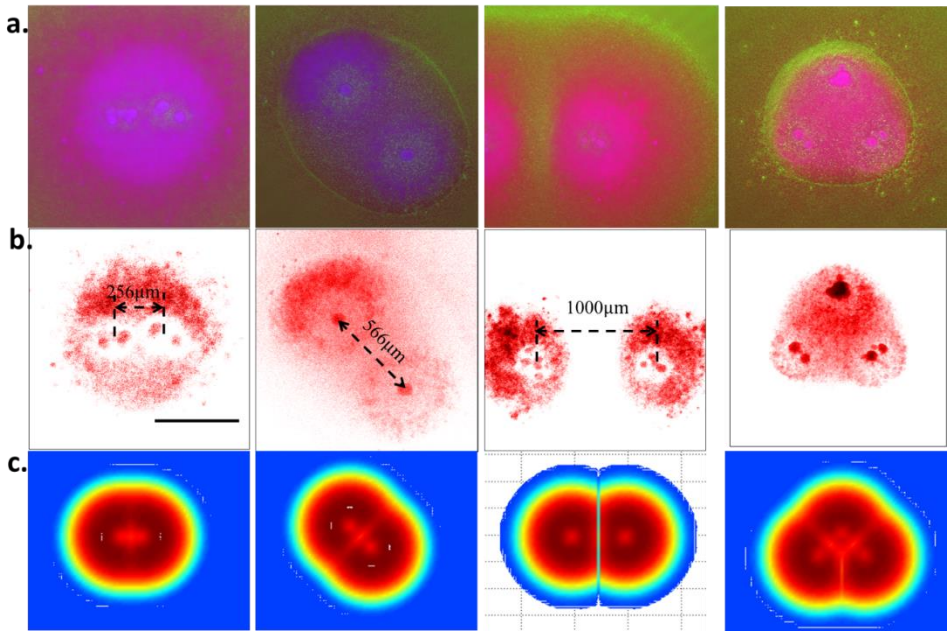

Figure 22: Pattern formation in multiple colonies. A. Composite fluorescent images of colonies and patterns from multiple initial seeding positions. All images were taken after 32 hrs incubated at 30˚C. **B.** mCherry fluorescent channels of (a). **C.** Simulated mCherry patterns using our PDE model using comparable seeding configurations.

- **Using mixed cell cultures**: our inkjet printing technique will also enable us to initiate self-organized pattern formation from mixed cultures containing different bacterial strains (same parental strain carrying different circuits or different strains carrying the same circuit) of the same species, or different species.

Here, we have demonstrated the capability of printing single colonies, multiple colonies with any designed configuration of one strain, or colonies containing cells from multiple strains. The endeavors to generate complex spatial patterns have both biological and applicational significance.

First, the synthetic system serves as a model framework to testify the principles of forming sophisticated patterns. Majority of the natural patterns are sophisticated. As we mentioned in Chapter 2, synthetic system could serve as a well-defined system to elucidate the principles of biological networks. The principles of forming various sophisticated patterns in a synthetic system could be generally applicable to naturally occurred complex patterns as well.

Second, sophisticated patterns generated in the synthetic system could be implemented into different applications. Figure 12C has demonstrated an application of an electronic circuit with multiple identity bacterial patterns. Compared to the applications demonstrated in Chapter 3, if precisely controllable and predictable sophisticated patterns can be generated, one can envision the possibility of generating more complicated structured materials (e.g. concentric domes, continuously connected domes et al.) with more well-defined physical properties.

References

1. Oates, A.C., L.G. Morelli, and S. Ares, *Patterning embryos with oscillations: structure, function and dynamics of the vertebrate segmentation clock.* Development, 2012. **139**(4): p. 625-39.

2. Kondo, S. and R. Asal, *A reaction-diffusion wave on the skin of the marine angelfish Pomacanthus.* Nature, 1995. **376**(6543): p. 765-8.

3. Lenz, P. and L. Sogaard-Andersen, *Temporal and spatial oscillations in bacteria.* Nat Rev Microbiol, 2011. **9**(8): p. 565-77.

4. Kruse, K. and F. Julicher, *Oscillations in cell biology.* Curr Opin Cell Biol, 2005. **17**(1): p. 20-6.

5. Ferrell Jr, James E., Tony Y.-C. Tsai, and Q. Yang, *Modeling the Cell Cycle: Why Do Certain Circuits Oscillate?* Cell, 2011. **144**(6): p. 874-885.

6. Rowlett, V.W. and W. Margolin, *The bacterial Min system.* Curr Biol, 2013. **23**(13): p. R553-6.

7. Hoyle, R.B., *Pattern formation : an introduction to methods*. 2006, Cambridge, UK ; New York: Cambridge University Press. x, 422 p.

8. Velenich, A. and J. Gore, *Synthetic approaches to understanding biological constraints.* Current Opinion in Chemical Biology, 2012. **16**(3-4): p. 323-328.

9. Riccione, K.A., et al., *A synthetic biology approach to understanding cellular information processing.* ACS Synth Biol, 2012. **1**(9): p. 389-402.

10. Aulehla, A. and O. Pourquie, *Oscillating signaling pathways during embryonic development.* Curr Opin Cell Biol, 2008. **20**(6): p. 632-7.

11. Palmeirim, I., et al., *Avian hairy gene expression identifies a molecular clock linked to vertebrate segmentation and somitogenesis.* Cell, 1997. **91**(5): p. 639-48.

12. Cooke, J. and E.C. Zeeman, *A clock and wavefront model for control of the number of repeated structures during animal morphogenesis.* J Theor Biol, 1976. **58**(2): p. 455-76.

13. Jiang, Y.J., et al., *Notch signalling and the synchronization of the somite segmentation clock.* Nature, 2000. **408**(6811): p. 475-9.

14. Oates, A.C. and R.K. Ho, *Hairy/E(spl)-related (Her) genes are central components of the segmentation oscillator and display redundancy with the Delta/Notch signaling pathway in the formation of anterior segmental boundaries in the zebrafish.* Development, 2002. **129**(12): p. 2929-46.

15. Hirata, H., et al., *Oscillatory expression of the bHLH factor Hes1 regulated by a negative feedback loop.* Science, 2002. **298**(5594): p. 840-3.

16. Gomez, C. and O. Pourquie, *Developmental control of segment numbers in vertebrates.* J Exp Zool B Mol Dev Evol, 2009. **312**(6): p. 533-44.

17. Schroter, C., et al., *Topology and dynamics of the zebrafish segmentation clock core circuit.* PLoS Biol, 2012. **10**(7): p. e1001364.

18. Dubrulle, J., M.J. McGrew, and O. Pourquie, *FGF signaling controls somite boundary position and regulates segmentation clock control of spatiotemporal Hox gene activation.* Cell, 2001. **106**(2): p. 219-32.

19. Pourquie, O., *The segmentation clock: Converting embryonic time into spatial pattern.* Science, 2003. **301**(5631): p. 328-330.

20. Finkelshtein, A., et al., *Bacterial swarms recruit cargo bacteria to pave the way in toxic environments.* MBio, 2015. **6**(3): p. e00074-15.

21. Liu, J., et al., *Metabolic co-dependence gives rise to collective oscillations within biofilms.* Nature, 2015. **523**(7562): p. 550-4.

22. Huang, K.C., Y. Meir, and N.S. Wingreen, *Dynamic structures in Escherichia coli: spontaneous formation of MinE rings and MinD polar zones.* Proc Natl Acad Sci U S A, 2003. **100**(22): p. 12724-8.

23. Loose, M., et al., *Spatial regulators for bacterial cell division self-organize into surface waves in vitro.* Science, 2008. **320**(5877): p. 789-92.

24. Payne, S., et al., *Temporal control of self-organized pattern formation without morphogen gradients in bacteria.* Mol Syst Biol, 2013. **9**: p. 697.

25. de Boer, P.A., R.E. Crossley, and L.I. Rothfield, *A division inhibitor and a topological specificity factor coded for by the minicell locus determine proper placement of the division septum in E. coli.* Cell, 1989. **56**(4): p. 641-9.

26. Bi, E.F. and J. Lutkenhaus, *FtsZ ring structure associated with division in Escherichia coli.* Nature, 1991. **354**(6349): p. 161-4.

27. Hu, Z., et al., *The MinC component of the division site selection system in Escherichia coli interacts with FtsZ to prevent polymerization.* Proc Natl Acad Sci U S A, 1999. **96**(26): p. 14819-24.

28. Cao, Y., et al., *Collective Space-Sensing Coordinates Pattern Scaling in Engineered Bacteria.* Cell, 2016. **165**(3): p. 620-30.

29. Liu, C., et al., *Sequential establishment of stripe patterns in an expanding cell population.* Science, 2011. **334**(6053): p. 238-41.

30. Kondo, S. and T. Miura, *Reaction-diffusion model as a framework for understanding biological pattern formation.* Science, 2010.

31. Sick, S., et al., *WNT and DKK determine hair follicle spacing through a reaction-diffusion mechanism.* Science, 2006. **314**(5804): p. 1447-1450.

32. Nakamasu, A., et al., *Interactions between zebrafish pigment cells responsible for the generation of Turing patterns.* Proceedings of the National Academy of Sciences of the United States of America, 2009. **106**(21): p. 8429-8434.

33. Lindner, B., et al., *Effects of noise in excitable systems*, in *Physics Reports*. 2004. p. 321-424.

34. Hempel, H., L. Schimansky-Geier, and J. & Garcia-Ojalvo, *Noise-sustained pulsating patterns and global oscillations in subexcitable media.* Physical Review Letters, 1999. **82(18), 3713**.

35. Maini, P.K., et al., *Turing's model for biological pattern formation and the robustness problem.* Interface Focus, 2012. **2**(4): p. 487-96.

36. Weart, R.B., et al., *A metabolic sensor governing cell size in bacteria.* Cell, 2007. **130**(2): p. 335-47.

37. Monahan, L.G., et al., *Coordinating bacterial cell division with nutrient availability: a role for glycolysis.* MBio, 2014. **5**(3): p. e00935-14.

38. Weymouth, F.W., J. Field, and M. Kleiber, *Relationship between body size and metabolism.* Proceedings of the Society for Experimental Biology and Medicine, 1942. **49**(3): p. 367-370.

39. Lesne, A. and M. Lagues, *Scale Invariance in Biology.* Scale Invariance: From Phase Transition to Turbulence, 2012: p. 361-384.

40. Bollenbach, T., et al., *Precision of the Dpp gradient.* Development, 2008. **135**(6): p. 1137-1146.

41. Balaskas, N., et al., *Gene Regulatory Logic for Reading the Sonic Hedgehog Signaling Gradient in the Vertebrate Neural Tube.* Cell, 2012. **148**(1-2): p. 273-284.

42. Dessaud, E., A.P. McMahon, and J. Briscoe, *Pattern formation in the vertebrate neural tube: a sonic hedgehog morphogen-regulated transcriptional network.* Development, 2008. **135**(15): p. 2489-2503.

43. Barkai, N. and D. Ben-Zvi, *'Big frog, small frog'--maintaining proportions in embryonic development: delivered on 2 July 2008 at the 33rd FEBS Congress in Athens, Greece.* FEBS J, 2009. **276**(5): p. 1196-207.

44. Gisiger, T., *Scale invariance in biology: coincidence or footprint of a universal mechanism?* Biol Rev Camb Philos Soc, 2001. **76**(2): p. 161-209.

45. Fried, P. and D. Iber, *Dynamic scaling of morphogen gradients on growing domains.* Nat Commun, 2014. **5**: p. 5077.

46. Lander, A.D., *Pattern, Growth, and Control.* Cell, 2011. **144**(6): p. 955-969.

47. Ben-Zvi, D., B. Shilo, and N. Barkai, *Scaling of morphogen gradients.* Current Opinion in Genetics & Development, 2011.

48. Gurdon, J.B. and P.Y. Bourillot, *Morphogen gradient interpretation.* Nature, 2001. **413**(6858): p. 797-803.

49. Averbukh, I., et al., *Scaling morphogen gradients during tissue growth by a cell division rule.* Development, 2014. **141**(10): p. 2150-6.

50. Skataric, M., E.V. Nikolaev, and E.D. Sontag, *Fundamental limitation of the instantaneous approximation in fold-change detection models.* IET Syst Biol, 2015. **9**(1): p. 1-15.

51. Wolpert, L., *Positional information and the spatial pattern of cellular differentiation.* Journal of Theoretical Biology, 1969. **25**(1): p. 1-47.

52. McHale, P., W. Rappel, and H. Levine, *Embryonic pattern scaling achieved by oppositely directed morphogen gradients.* Physical biology, 2006.

53. Ben-Zvi, D. and N. Barkai, *Scaling of morphogen gradients by an expansion-repression integral feedback control.* Proceedings of the National Academy of Sciences, 2010. **107**(15): p. 6924-6929.

54. Ben-Zvi, D., et al., *Scaling of the BMP activation gradient in Xenopus embryos.* Nature, 2008.

55. Chen, H., et al., *A System of Repressor Gradients Spatially Organizes the Boundaries of Bicoid-Dependent Target Genes.* Cell, 2012. **149**(3): p. 618-629.

56. Roth, S. and J. Lynch, *Does the Bicoid Gradient Matter?* Cell, 2012. **149**(3): p. 511-512.

57. Tan, C., P. Marguet, and L.C. You, *Emergent bistability by a growth-modulating positive feedback circuit.* Nature Chemical Biology, 2009. **5**(11): p. 842-848.

58. Stano, N.M. and S.S. Patel, *T7 lysozyme represses T7 RNA polymerase transcription by destabilizing the open complex during initiation.* Journal of Biological Chemistry, 2004. **279**(16): p. 16136-16143.

59. Cohen, D.J., R.C. Morfino, and M.M. Maharbiz, *A Modified Consumer Inkjet for Spatiotemporal Control of Gene Expression.* Plos One, 2009. **4**(9).

60. Edelstein-Keshet, L., *Mathematical models in biology*. Vol. 46. 1988. xvii, 586 p.

61. Jozefczuk, S., et al., *Metabolomic and transcriptomic stress response of Escherichia coli.* Molecular Systems Biology, 2010. **6**.

62. Morse, R.P., et al., *Structural basis of toxicity and immunity in contact-dependent growth inhibition (CDI) systems.* Proceedings of the National Academy of Sciences of the United States of America, 2012. **109**(52): p. 21480-21485.

63. Salmon, K., et al., *Global gene expression profiling in Escherichia coli K12 - The effects of oxygen availability and FNR.* Journal of Biological Chemistry, 2003. **278**(32): p. 29837-29855.

64. Prindle, A., et al., *Ion channels enable electrical communication in bacterial communities.* Nature, 2015. **527**(7576): p. 59-63.

65. Rogers, K.W. and A.F. Schier, *Morphogen gradients: from generation to interpretation.* Annu Rev Cell Dev Biol, 2011. **27**: p. 377-407.

66. Tomlin, C.J. and J.D. Axelrod, *Biology by numbers: mathematical modelling in developmental biology.* Nat Rev Genet, 2007. **8**(5): p. 331-40.

67. Von Dassow, G., et al., *The segment polarity network is a robust developmental module.* Nature, 2000. **406**(6792): p. 188-192.

68. Stathopoulos, A. and D. Iber, *Studies of morphogens: keep calm and carry on.* Development, 2013. **140**(20): p. 4119-4124.

69. Ben-Zvi, D., et al., *Expansion-Repression Mechanism for Scaling the Dpp Activation Gradient in Drosophila Wing Imaginal Discs.* Current Biology, 2011. **21**(16): p. 1391-1396.

70. Houchmandzadeh, B., E. Wieschaus, and S. Leibler, *Precise domain specification in the developing Drosophila embryo.* Physical Review E, 2005.

71. Howard, M. and P. Wolde, *Finding the center reliably: robust patterns of developmental gene expression.* Physical review letters, 2005.

72. Slusarczyk, A.L., A. Lin, and R. Weiss, *Foundations for the design and implementation of synthetic genetic circuits.* Nature Reviews Genetics, 2012. **13**(6): p. 406-420.

73. Tanouchi, Y., R.P. Smith, and L. You, *Engineering microbial systems to explore ecological and evolutionary dynamics.* Curr Opin Biotechnol, 2012. **23**(5): p. 791-7.

74. Brophy, J.A. and C.A. Voigt, *Principles of genetic circuit design.* Nat Methods, 2014. **11**(5): p. 508-20.

75. Jessup, C.M., et al., *Big questions, small worlds: microbial model systems in ecology.* Trends Ecol Evol, 2004. **19**(4): p. 189-97.

76. Elowitz, M. and W.A. Lim, *Build life to understand it.* Nature, 2010. **468**(7326): p. 889-90.

77. Basu, S., et al., *A synthetic multicellular system for programmed pattern formation.* Nature, 2005.

78. Schaerli, Y., et al., *A unified design space of synthetic stripe-forming networks.* Nature Communications, 2014. **5**.

79. Tabor, J.J., et al., *A Synthetic Genetic Edge Detection Program.* Cell, 2009. **137**(7): p. 1272-1281.

80. Sinervo, B., *Egg Incubation - Its Effects on Embryonic-Development in Birds and Reptiles - Deeming,Dc, Ferguson,Mwj.* Science, 1992. **256**(5063): p. 1574-1574.

81. Brawand, D., W. Wahli, and H. Kaessmann, *Loss of egg yolk genes in mammals and the origin of lactation and placentation.* Plos Biology, 2008. **6**(3): p. 507-517.

82. Dzialowski, E.M. and P.R. Sotherland, *Maternal effects of egg size on emu Dromaius novaehollandiae egg composition and hatchling phenotype.* Journal of Experimental Biology, 2004. **207**(4): p. 597-606.

83. Briscoe, J. and J. Ericson, *Specification of neuronal fates in the ventral neural tube.* Current Opinion in Neurobiology, 2001. **11**(1): p. 43-49.

84. Ahn, S. and A.L. Joyner, *Dynamic changes in the response of cells to positive hedgehog signaling during mouse limb patterning.* Cell, 2004. **118**(4): p. 505-516.

85. Pages, F. and S. Kerridge, *Morphogen gradients - a question of time or concentration?* Trends in Genetics, 2000. **16**(1): p. 40-44.

86. Dessaud, E., et al., *Interpretation of the sonic hedgehog morphogen gradient by a temporal adaptation mechanism.* Nature, 2007. **450**(7170): p. 717-U7.

87. Bullough, W.S., *The control of mitotic activity in adult mammalian tissues.* Biol Rev Camb Philos Soc, 1962. **37**: p. 307-42.

88. Gamer, L.W., J. Nove, and V. Rosen, *Return of the chalones.* Dev Cell, 2003. **4**(2): p. 143-4.

89. Chen, A.Y., et al., *Synthesis and patterning of tunable multiscale materials with engineered cells.* Nat Mater, 2014. **13**(5): p. 515-23.

90. Wang, C.L., D.S. Clark, and J.D. Keasling, *Analysis of an engineered sulfate reduction pathway and cadmium precipitation on the cell surface.* Biotechnol Bioeng, 2001. **75**(3): p. 285-91.

91. Sambrook, J. and D.W. Russell, *Molecular cloning : a laboratory manual*. 3rd ed. 2001, Cold Spring Harbor, N.Y.: Cold Spring Harbor Laboratory Press.

92. Kenkre, V.M., *Results from variants of the Fisher equation in the study of epidemics and bacteria.* Physica a-Statistical Mechanics and Its Applications, 2004. **342**(1-2): p. 242-248.

93. Murray, J.D., et al., *Spatial pattern formation in biology: I. Dermal wound healing. II. Bacterial patterns.* Journal of the Franklin Institute-Engineering and Applied Mathematics, 1998. **335B**(2): p. 303-332.

94. Maini, P.K., *Using mathematical models to help understand biological pattern formation.* C R Biol, 2004. **327**(3): p. 225-34.

95. Song, H., et al., *Spatiotemporal modulation of biodiversity in a synthetic chemical-mediated ecosystem.* Nat Chem Biol, 2009. **5**(12): p. 929-35.

96. Collins, C.H., J.R. Leadbetter, and F.H. Arnold, *Dual selection enhances the signaling specificity of a variant of the quorum-sensing transcriptional activator LuxR.* Nat Biotechnol, 2006. **24**(6): p. 708-12.

97. You, L., et al., *Programmed population control by cell-cell communication and regulated killing.* Nature, 2004. **428**(6985): p. 868-71.

98. Kumar, A. and S.S. Patel, *Inhibition of T7 RNA polymerase: Transcription initiation and transition from initiation to elongation are inhibited by T7 lysozyme via a ternary complex with RNA polymerase and promoter DNA.* Biochemistry, 1997. **36**(45): p. 13954-13962.

99. Aronson, D. and H. Weinberger, *Multidimensional nonlinear diffusion arising in population genetics.* Advances in Mathematics, 1978. **30.1**: p. 33-76.

100. Tyson, R., L.G. Stern, and R.J. LeVeque, *Fractional step methods applied to a chemotaxis model.* Journal of Mathematical Biology, 2000. **41**(5): p. 455-475.

101. Ryser, M.D., Y.D. Qu, and S.V. Komarova, *Osteoprotegerin in Bone Metastases: Mathematical Solution to the Puzzle.* Plos Computational Biology, 2012. **8**(10).

102. Turing, A., *The chemical basis of morphogenesis.* Transactions of the Royal Society of, 1952.

103. Pate, E. and H.G. Othmer, *Applications of a model for scale-invariant pattern formation in developing systems.* Differentiation, 1984. **28**(1): p. 1-8.

104. Hunding, A. and P. Sørensen, *Size adaptation of Turing prepatterns.* Journal of mathematical biology, 1988.

105. Aegerter-Wilmsen, T., C.M. Aegerter, and T. Bisseling, *Model for the robust establishment of precise proportions in the early Drosophila embryo.* J Theor Biol, 2005. **234**(1): p. 13-9.

106. Ricard, J., *Systems biology and the origins of life? part II. Are biochemical networks possible ancestors of living systems? networks of catalysed chemical reactions: non-equilibrium, self-organization and evolution.* C R Biol, 2010. **333**(11-12): p. 769-78.

107. Ishihara, S. and K. Kaneko, *Turing pattern with proportion preservation.* Journal of Theoretical Biology, 2006. **238**(3): p. 683-693.

108. Boissonade, J., *Self-organization phenomena in non-equilibrium chemical systems.* Origins of Life: Self-Organization and/or Biological Evolution?, 2009: p. 23-36.

109. Rosen, R., *Self-Organization in Non-Equilibrium Systems - Nicolis,G, Prigogine,I.* International Journal of General Systems, 1978. **4**(4): p. 266-269.

110. Crick, F., *Diffusion in embryogenesis.* Nature, 1970. **225**(5231): p. 420-2.

111. McHale, P., W.J. Rappel, and H. Levine, *Embryonic pattern scaling achieved by oppositely directed morphogen gradients.* Physical Biology, 2006. **3**(2): p. 107-120.

112. Ben-Zvi, D., et al., *Scaling of the BMP activation gradient in Xenopus embryos.* Nature, 2008. **453**(7199): p. 1205-11.

113. Barkai, N. and B. Shilo, *Developmental biology: Segmentation within scale.* Nature, 2013.

114. Currey, J.D., *Mechanical-Properties of Mother of Pearl in Tension.* Proceedings of the Royal Society Series B-Biological Sciences, 1977. **196**(1125): p. 443-+.

115. Luz, G.M. and J.F. Mano, *Mineralized structures in nature: Examples and inspirations for the design of new composite materials and biomaterials.* Composites Science and Technology, 2010. **70**(13): p. 1777-1788.

116. Jackson, A.P., J.F.V. Vincent, and R.M. Turner, *The Mechanical Design of Nacre.* Proceedings of the Royal Society Series B-Biological Sciences, 1988. **234**(1277): p. 415-+.

117. Chen, A.Y., C. Zhong, and T.K. Lu, *Engineering living functional materials.* ACS Synth Biol, 2015. **4**(1): p. 8-11.

118. Purnick, P.E. and R. Weiss, *The second wave of synthetic biology: from modules to systems.* Nat Rev Mol Cell Biol, 2009. **10**(6): p. 410-22.

119. Khalil, A.S. and J.J. Collins, *Synthetic biology: applications come of age.* Nat Rev Genet, 2010. **11**(5): p. 367-79.

120. Petka, W.A., et al., *Reversible hydrogels from self-assembling artificial proteins.* Science, 1998. **281**(5375): p. 389-92.

121. Whitesides, G.M. and B. Grzybowski, *Self-assembly at all scales.* Science, 2002. **295**(5564): p. 2418-2421.

122. Rajagopal, K. and J.P. Schneider, *Self-assembling peptides and proteins for nanotechnological applications.* Curr Opin Struct Biol, 2004. **14**(4): p. 480-6.

123. Zhang, S., *Fabrication of novel biomaterials through molecular self-assembly.* Nat Biotechnol, 2003. **21**(10): p. 1171-8.

124. Ringler, P. and G.E. Schulz, *Self-assembly of proteins into designed networks.* Science, 2003. **302**(5642): p. 106-109.

125. Zhong, C., et al., *Strong underwater adhesives made by self-assembling multi-protein nanofibres.* Nature nanotechnology, 2012. **9**(10): p. 858-866.

126. Ryadnov, M.G. and D.N. Woolfson, *Engineering the morphology of a self-assembling protein fibre.* Nat Mater, 2003. **2**(5): p. 329-32.

127. Lee, Y.J., et al., *Fabricating genetically engineered high-power lithium-ion batteries using multiple virus genes.* Science, 2009. **324**(5930): p. 1051-5.

128. Aggeli, A., et al., *pH as a trigger of peptide beta-sheet self-assembly and reversible switching between nematic and isotropic phases.* Journal of the American Chemical Society, 2003. **125**(32): p. 9619-9628.

129. Fichman, G. and E. Gazit, *Self-assembly of short peptides to form hydrogels: design of building blocks, physical properties and technological applications.* Acta Biomater, 2014. **10**(4): p. 1671-82.

130. Yan, H., et al., *DNA-templated self-assembly of protein arrays and highly conductive nanowires.* Science, 2003. **301**(5641): p. 1882-4.

131. Seeman, N.C. and A.M. Belcher, *Emulating biology: Building nanostructures from the bottom up.* Proceedings of the National Academy of Sciences of the United States of America, 2002. **99**: p. 6451-6455.

132. Seeman, N.C., *Nanomaterials based on DNA.* Annu Rev Biochem, 2010. **79**: p. 65-87.

133. Elbaz, J., P. Yin, and C.A. Voigt, *Genetic encoding of DNA nanostructures and their self-assembly in living bacteria.* Nat Commun, 2016. **7**: p. 11179.

134. Sleytr, U.B. and T.J. Beveridge, *Bacterial S-layers.* Trends Microbiol, 1999. **7**(6): p. 253-60.

135. Shenton, W., et al., *Synthesis of cadmium sulphide superlattices using self-assembled bacterial S-layers.* Nature, 1997. **389**(6651): p. 585-587.

136. Barnhart, M.M. and M.R. Chapman, *Curli biogenesis and function.* Annu Rev Microbiol, 2006. **60**: p. 131-47.

137. Zhang, R.L., et al., *Enhanced Permeation of a Hydrophobic Fluid through Particles with Hydrophobic and Hydrophilic Patterned Surfaces.* Scientific Reports, 2014. **4**.

138. Basu, S., et al., *A synthetic multicellular system for programmed pattern formation.* Nature, 2005. **434**(7037): p. 1130-4.

139. Tabor, J.J., et al., *A synthetic genetic edge detection program.* Cell, 2009. **137**(7): p. 1272-81.

140. Schaerli, Y., et al., *A unified design space of synthetic stripe-forming networks.* Nat Commun, 2014. **5**: p. 4905.

141. Moon, T.S., et al., *Genetic programs constructed from layered logic gates in single cells.* Nature, 2012. **491**(7423): p. 249-53.

142. Fernandez-Rodriguez, J., et al., *Memory and Combinatorial Logic Based on DNA Inversions: Dynamics and Evolutionary Stability.* ACS Synth Biol, 2015. **4**(12): p. 1361-72.

143. Andrianantoandro, E., et al., *Synthetic biology: new engineering rules for an emerging discipline.* Mol Syst Biol, 2006. **2**: p. 2006 0028.

144. Siuti, P., J. Yazbek, and T.K. Lu, *Synthetic circuits integrating logic and memory in living cells.* Nat Biotechnol, 2013. **31**(5): p. 448-52.

145. Tamsir, A., J.J. Tabor, and C.A. Voigt, *Robust multicellular computing using genetically encoded NOR gates and chemical 'wires'.* Nature, 2011. **469**(7329): p. 212-5.

146. Rosenfeld, N., et al., *Gene regulation at the single-cell level.* Science, 2005. **307**(5717): p. 1962-1965.

147. Bennett, M.R. and J. Hasty, *Microfluidic devices for measuring gene network dynamics in single cells.* Nat Rev Genet, 2009. **10**(9): p. 628-38.

148. Din, M.O., et al., *Synchronized cycles of bacterial lysis for in vivo delivery.* Nature, 2016. **536**(7614): p. 81-5.

149. Balagadde, F.K., et al., *A synthetic Escherichia coli predator-prey ecosystem.* Mol Syst Biol, 2008. **4**: p. 187.

150. Chen, Y., et al., *SYNTHETIC BIOLOGY. Emergent genetic oscillations in a synthetic microbial consortium.* Science, 2015. **349**(6251): p. 986-9.

151. Lander, A.D., *Pattern, growth, and control.* Cell, 2011. **144**(6): p. 955-69.

152. Newman, S.A. and H.L. Frisch, *Dynamics of skeletal pattern formation in developing chick limb.* Science, 1979. **205**(4407): p. 662-8.

153. Jernvall, J. and I. Thesleff, *Reiterative signaling and patterning during mammalian tooth morphogenesis.* Mech Dev, 2000. **92**(1): p. 19-29.

154. Kavanagh, K.D., A.R. Evans, and J. Jernvall, *Predicting evolutionary patterns of mammalian teeth from development.* Nature, 2007. **449**(7161): p. 427-32.

155. Davies, D.G., et al., *The involvement of cell-to-cell signals in the development of a bacterial biofilm.* Science, 1998. **280**(5361): p. 295-8.

156. Asally, M., et al., *Localized cell death focuses mechanical forces during 3D patterning in a biofilm.* Proc Natl Acad Sci U S A, 2012. **109**(46): p. 18891-6.

157. Nguyen, P.Q., et al., *Programmable biofilm-based materials from engineered curli nanofibres.* Nat Commun, 2014. **5**: p. 4945.

158. Li, Y., et al., *Surface plasmon coupling enhanced dielectric environment sensitivity in a quasi-three-dimensional metallic nanohole array.* Opt Express, 2010. **18**(4): p. 3546-55.

159. Grandidier, J., et al., *Light Absorption Enhancement in Thin-Film Solar Cells Using Whispering Gallery Modes in Dielectric Nanospheres.* Advanced Materials, 2011. **23**(10): p. 1272-+.

160. Han, G.Q., et al., *Controllable synthesis of three dimensional electrodeposited Co-P nanosphere arrays as efficient electrocatalysts for overall water splitting.* Rsc Advances, 2016. **6**(58): p. 52761-52771.

161. Sun, F., et al., *Synthesis of bioactive protein hydrogels by genetically encoded SpyTag-SpyCatcher chemistry.* Proc Natl Acad Sci U S A, 2014. **111**(31): p. 11269-74.

162. Vallet-Regi, M., M. Colilla, and B. Gonzalez, *Medical applications of organic-inorganic hybrid materials within the field of silica-based bioceramics.* Chemical Society Reviews, 2011. **40**(2): p. 596-607.

163. Hirst, A.R., et al., *High-tech applications of self-assembling supramolecular nanostructured gel-phase materials: from regenerative medicine to electronic devices.* Angew Chem Int Ed Engl, 2008. **47**(42): p. 8002-18.

164. Goldberg, M., R. Langer, and X. Jia, *Nanostructured materials for applications in drug delivery and tissue engineering.* J Biomater Sci Polym Ed, 2007. **18**(3): p. 241-68.

165. Langer, R. and D.A. Tirrell, *Designing materials for biology and medicine.* Nature, 2004. **428**(6982): p. 487-92.

166. Niu, Z., et al., *Porous graphene materials for water remediation.* Small, 2014. **10**(17): p. 3434-41.

167. Li, H., L.F. Liu, and F.L. Yang, *Covalent assembly of 3D graphene/polypyrrole foams for oil spill cleanup.* Journal of Materials Chemistry A, 2013. **1**(10): p. 3446-3453.

168. Elghetany, M.T. and A. Saleem, *Methods for staining amyloid in tissues: a review.* Stain Technol, 1988. **63**(4): p. 201-12.

169. Harfe, B.D., et al., *Evidence for an expansion-based temporal Shh gradient in specifying vertebrate digit identities.* Cell, 2004. **118**(4): p. 517-528.

Biography

Yangxiaolu Cao was born in Altay, Xinjiang Province, China on June 8th 1990. She went to Tsinghua University in Aug of 2008 and received a bachelor degree in Mechanical Engineering in June of 2012. After undergraduate, she joined Dr. Lingchong You's lab in the department of Biomedical Engineering at Duke University in Aug of 2012. For a complete list of publications and honors, see below:

Publications:

1. Cao Y, Ryser MD, Payne S, Li B, Rao CV, You L. Collective space-sensing coordinates pattern scaling in engineered bacteria. **Cell**. 2016 Apr 21;165(3):620-30.

2. Cao Y*, Lopatkin A*, You L. Elements of biological oscillations in time and space. **Nature Structural & Molecular Biology**. 2016 Dec 1;23(12):1030-4.

3. Cao Y, Feng Y, Ryser MD, Zhu K, Herschlag G, Marusak K, Zauscher S, You L. Programmed assembly of pressure sensors using pattern-forming bacteria. **Nature Biotechnology** (under review).

4. Payne S*, Li B*, Cao Y, Schaeffer D, Ryser MD, You L. Temporal control of self-organized pattern formation without morphogen gradients in bacteria. **Molecular systems biology**. 2013 Jan; 9(1):697.

5. Marusak KE, Feng Y, Eben CF, Payne ST, Cao Y, You L, Zauscher S. Cadmium sulphide quantum dots with tunable electronic properties by bacterial precipitation. **RSC Advances**. 2016;6(80):76158-66.

6. Feng Y, Ngaboyamahina E, Marusak KE, Cao Y, You L, Glass JT, Zauscher S. Hybrid (Organic/Inorganic) Electrodes from Bacterially Precipitated CdS for PEC/Storage Applications. **The Journal of Physical Chemistry C**. 2017 Jan 20.

Honors:

1. 2016 Kewaunee Student Achievement Award

2. GPNANO fellowship (5 out of 180 applicants), 2014-2015